ALAN ANTÔNIO DAS GRAÇAS SANTOS

DESIGN OF HEUSLER ALLOYS USING Co-*VB*-Sn (*VB* = V, Nb, Ta) ATOMS WITHIN AB INITIO CALCULATIONS FOR THERMOELECTRIC APPLICATIONS

Dissertation submitted to the Programa de Pós-Graduação Multicêntrico em Química de Minas Gerais of the Universidade Federal de Viçosa-campus Rio Paranaíba, in partial fulfillment of the requirements for the degree of *Magister Scientiae*.

Adviser: Pablo Damasceno Borges

RIO PARANAÍBA - MINAS GERAIS
2023

Ficha catalográfica elaborada pela Biblioteca da Universidade Federal de Viçosa - Campus Rio Paranaíba

T
S237d 2023

Santos, Alan Antônio das Graças, 1998-
Design of Heusler alloys using Co-*VB*-Sn (*VB* = V, Nb, Ta) atoms within ab initio calculations for thermoelectric applications / Alan Antônio das Graças Santos. – Rio Paranaíba, MG, 2023.
99 f.: il. (algumas color.).

Inclui apêndice.
Orientador: Pablo Damasceno Borges.
Dissertação (mestrado) - Universidade Federal de Viçosa, Instituto de Ciências Exatas e Tecnológicas, 2023.
Referências bibliográficas: f.85-98.
DOI: https://doi.org/10.47328/ufvcrp.2023.011

1. Heusler alloys. 2. Thermoelectric materials. 3. DFT. I. Borges, Pablo Damasceno, 1975-. II. Universidade Federal de Viçosa. Instituto de Ciências Exatas e Tecnológicas. Mestrado Multicêntrico em Química de Minas Gerais. III. Título.

547

Bibliotecário(a) responsável: Crislene Silva de Sousa CRB-6/2539

ALAN ANTÔNIO DAS GRAÇAS SANTOS

DESIGN OF HEUSLER ALLOYS USING Co-*VB*-Sn (*VB* = V, Nb, Ta) ATOMS WITHIN AB INITIO CALCULATIONS FOR THERMOELECTRIC APPLICATIONS

Dissertation submitted to the Programa de Pós-Graduação Multicêntrico em Química de Minas gerais of the Universidade Federal de Viçosa-campus Rio Paranaíba, in partial fulfillment of the requirements for the degree of *Magister Scientiae*.

APPROVED: November 07, 2023.

Assent:

Documento assinado digitalmente
gov.br
ALAN ANTONIO DAS GRACAS SANTOS
Data: 22/11/2023 19:19:55-0300
Verifique em https://validar.iti.gov.br

Alan Antônio das Graças Santos
Author

Documento assinado digitalmente
gov.br
PABLO DAMASCENO BORGES
Data: 23/11/2023 07:35:00-0300
Verifique em https://validar.iti.gov.br

Pablo Damasceno Borges
Adviser

To those who fight for the
preservation of our common home.

ACKNOWLEDGEMENTS

To my family, for their love and affection, which have always been my pillar even from a distance.

To my friends, who bring happiness to my university life.

To Prof. Dr. Pablo, for his guidance, friendship, support, and prompt assistance throughout the entire process.

To the research group, especially to Nathan, for his assistance throughout the research.

To all the professionals at the Federal University of Viçosa, Rio Paranaíba *campus*, especially Anderson Oliveira, for their prompt assistance with administrative matters.

To the Federal University of Viçosa and the Multicentric Master's Program in Chemistry of Minas Gerais, for the opportunity to pursue postgraduate studies.

To the Coordenação de Aperfeiçoamento de Pessoal de Nível Superior (CAPES), to granting the scholarship.

"Now, forasmuch as, following the senses,
Thou seest that the reason has short wings."

Canto II – Paradiso – Divine Comedy

DANTE ALIGHIERI

ABSTRACT

SANTOS, A. A. G., M.Sc., Universidade Federal de Viçosa, November 2023. **Design of Heusler Alloys Using Co-*VB*-Sn (*VB* = V, Nb, Ta) Atoms Within *Ab Initio* Calculations for Thermoelectric Applications**. Advisor: Pablo Damasceno Borges.

Environmentally friendly energetic matrices are essential for sustainable human development. In this perspective, Heusler alloys have shown to be promising materials for thermoelectric applications. This work presents a theoretical study of Co-*VB*-Sn (*VB* = V, Nb, Ta) Heusler alloys within the GGA-PBE and hybrid (HSE06) approaches. The cubic (C1b) CoVSn, CoNbSn and CoTaSn Half-Heusler compounds exhibit semiconductor characteristics and a bandgap of 1.33eV, 1.50eV and 1.18 eV, respectively, when Co occupies the Wyckoff 4c site. The cubic (L21) Co_2VSn, Co_2NbSn and Co_2TaSn Full-Heusler are half-metallic compounds with a bandgap of 1.26eV, 0.86eV and1.36 eV. All the systems present a total magnetic moment in agreement with the Slater-Pauling rule. The chemical bonds analyses indicate covalent-polar bonds in the studied alloys. High effective mass was found to semiconductors structures, an excellent result in relation to application as thermoelectric. Using Wannier functions, and based in experimental data present in the literature it was studied the thermoelectric parameters for the CoTaSn alloy.

Keywords: Heusler alloys. Co-*VB*-Sn. Thermoelectric materials. DFT. Effective mass.

RESUMO

SANTOS, A. A. G., M.Sc., Universidade Federal de Viçosa, novembro de 2023. **Design of Heusler Alloys Using Co-*VB*-Sn (*VB* = V, Nb, Ta) Atoms Within *Ab Initio* Calculations for Thermoelectric Applications**. Orientador: Pablo Damasceno Borges.

Matrizes energéticas ambientalmente amigáveis são essenciais para o desenvolvimento humano sustentável. Nessa perspectiva, as ligas de Heusler têm se mostrado materiais promissores para aplicações termoelétricas. Este trabalho apresenta um estudo teórico das ligas de Heusler Co-VB-Sn (*VB* = V, Nb, Ta) dentro das abordagens GGA-PBE e híbrido (HSE06). As ligas Half-Heusler cúbica (C_{1b}) CoVSn, CoNbSn e CoTaSn exibe características semicondutoras e um bandgap de 1,33eV, 1,50eV e 1,18 eV, respectivamente, quando o Co ocupa o sítio Wyckoff 4c. As ligas Full-Heusler cúbico (L_{21}) Co_2VSn, Co_2NbSn e Co_2TaSn é um *half-metal* com um bandgap de 1,26eV, 0,86eV e 1,36 eV. Todos os sistemas apresentam um momento magnético total em concordância com a regra de Slater-Pauling. As análises das ligações químicas indicam ligações covalentes-polares nas ligas estudadas. Grande massas efetivas foram encontradas para as estruturas semicondutoras, um excelente resultado em relação à aplicação como termoelétrico. Usando funções de Wannier, e baseado em dados experimentais presentes na literatura, foram estudados os parâmetros termoelétricos para a liga CoTaSn.

Palavras-chave: Ligas Heusler. Co-*VB*-Sn. Materiais termoelétricos. DFT. Massas efetivas.

LIST OF ILLUSTRATIONS

Figure 1.1 - Global primary energy consumption by source from 2000 to 2022 (a) absolute numbers (b) relative numbers [1]…….....19

Figure 1.2 - Representation of the circuits that describe the (a) Seebeck and (b) Peltier effects……20

Figure 2.1 - Kohn-Sham self-consistent scheme……30

Figure 2.2 - Comparison of a wavefunction in the Coulomb potential (real) of the nucleus to the one in the pseudopotential (approximation) [75]…….....35

Figure 2.3 - Brillouin zone and high symmetry points to crystalline structures of the space groups a) F-43m and b) Fm-3m [80]……..36

Figure 2.4 - Relation between Bloch functions and Wannier functions (WFs). Source: [87]…….....37

Figure 2.5 - 2D plot ELF to a) molecule ethene b) NaCl salt c) along the plane containing the chemical bond between C and a Cu–Cu metallic bond. Source: [96]……..…41

Figure 2.6 - Representation of a) VBT parabolic approximation, b) VBB parabolic approximation. Source: [87,100]……42

Figure 2.7 - Classification of the bands according to the effective mass presented at points of high symmetry…….....43

Figure 3.1 - Equilibrium structures of several (a) HH and (b) FH alloys from GGA-PBE calculations……45

Figure 4.1 - Crystal structures: (a) Half-Heusler, (b) Full-Heusler, (c) NaCl-type and (d) ZnSn-type. In figures (e-f) are represented three possible chemical bonds of atom in 4c. The structures Full-Heusler (h-j) may have the same type of bonds as the Half-Heusler……47

Figure 4.2 - Total energy versus lattice parameter of several (a) HH and (b) FH vanadium structures for obtained from GGA-PBE calculations. The cohesive energy was calculated from Equation 2.69 within GGA-PBE (HSE06) approximation…….48

Figure 4.3 - Total energy versus lattice parameter of several (a) HH and (b) FH niobium structures for obtained from GGA-PBE calculations. The cohesive energy was calculated from Equation 2.69 within GGA-PBE (HSE06) approximation…….50

Figure 4.4 - Total energy versus lattice parameter of several (a) HH and (b) FH tantalum structures for obtained from GGA-PBE calculations. The cohesive energy was calculated from Equation 2.69 within GGA-PBE (HSE06) approximation…….51

Figure 4.5 - TDOS and PDOS for (a-b) HH-A, (c-d) HH-B and (e-f) HH-C vanadium structures, obtained from PBE calculations; (g-h) HH-A, (i-j) HH-B and (k-l) HH-C vanadium structures, obtained from HSE06 calculations……54

Figure 4.6 - TDOS and PDOS for (a-b) FH-A, (c-d) FH-B and (e-f) FH-C vanadium structures, obtained from PBE calculations; (g-h) FH-A, (i-j) FH-B and (k-l) FH-C vanadium structures, obtained from HSE06 calculations……55

Figure 4.7 - TDOS and PDOS for (a-b) HH-A, (c-d) HH-B and (e-f) HH-C niobium structures, obtained from PBE calculations; (g-h) HH-A, (i-j) HH-B and (k-l) HH-C niobium structures, obtained from HSE06 calculations……...59

Figure 4.8 - TDOS and PDOS for (a-b) FH-A, (c-d) FH-B and (e-f) FH-C niobium structures, obtained from PBE calculations; (g-h) FH-A, (i-j) FH-B and (k-l) FH-C niobium structures, obtained from HSE06 calculations……...60

Figure 4.9 - TDOS and PDOS for (a-b) HH-A, (c-d) HH-B and (e-f) HH-C tantalum structures, obtained from PBE calculations; (g-h) HH-A, (i-j) HH-B and (k-l) HH-C tantalum structures, obtained from HSE06 calculations……..63

Figure 4.10 - TDOS and PDOS for (a-b) FH-A, (c-d) FH-B and (e-f) FH-C structures tantalum, obtained from GGA-PBE calculations; (g-h) FH-A, (i-j) FH-B and (k-l) FH-C tantalum structures, obtained from HSE06 calculations……..…64

Figure 4.11 - Bandstructure of vanadium HH-A alloy (a) GGA-PBE spin up and down (b) GGA-PBE+SOC (c) CBB Γ - X - W (d) VTB W – L (e) VTB W - L - Γ (f) VTB X - W – Γ……65

Figure 4.12 - TDOS of HH-A vanadium structure obtained from (a) PBE (b) PBE-SOC. Curve adjusted by Equation 2.68, within free electron approximation (FEA), using the respective effective mass……67

Figure 4.13 - Bandstructure of niobium HH-A (a) GGA-PBE spin up and down (b) GGA-PBE+SOC (c) CBB Γ - X - W (d) VTB W – L (e) VTB W - L - Γ (f) VTB X - W – Γ……68

Figure 4.14 - TDOS of HH-A niobium structure obtained from (a) PBE (b) PBE-SOC. Curve adjusted by Equation 2.68, within free electron approximation (FEA), using the respective effective mass……69

Figure 4.15 - Bandstructure for tantalum HH-A (a) GGA-PBE spin up and down (b) GGA-PBE+SOC (c) CBB Γ - X - W (d) VTB W – L (e) VTB W - L - Γ (f) VTB X - W – Γ……70

Figure 4.16 - TDOS of CoNbSn HH-A structure obtained from (a) PBE (b) PBE-SOC calculation and adjusted by Equation 2.68, within free electron approximation (FEA)……71

Figure 4.17 - Representation of crystallography plans (121) and (101) in the a) HH-A and b) FH-A structures……..72

Figure 4.18 - Charge density of a) HH-A vanadium with isosurface: 0.055 eÅ^{-3}, b) FH-A vanadium with isosurface: 0.044 eÅ^{-3}; and Electron localization function of c) HH-A vanadium with isosurface: 0.22, and d) FH-A vanadium with isosurface: 0.16……..74

Figure 4.19 - Electron localization function obtained from HSE06 calculations in the planes $(1\bar{2}1)$ and (101) for a) HH-A and b) FH-A vanadium structures……...75

Figure 4.20 - Charge density of a) HH-A niobium with isosurface: 0.057 eÅ^{-3}, b) FH-A niobium with isosurface: 0.044 eÅ^{-3}; and Electron localization function of c) HH-A niobium with isosurface: 0.22, and d) FH-A niobium with isosurface: 0.16……77

Figure 4.21 - Electron localization function obtained from HSE06 calculations in the planes $(1\bar{2}1)$ and (101) for a) HH-A and b) FH-A niobium structures……..78

Figure 4.22 - Charge density of a) HH-A tantalum with isosurface: 0.052 eÅ^{-3}, b) FH-A tantalum with isosurface: 0.045 eÅ^{-3}; and Electron localization function of c) HH-A tantalum with isosurface: 0.23, and d) FH-A tantalum with isosurface: 0.28……..80

Figure 4.23 - Electron localization function obtained from HSE06 calculations in the planes $(1\bar{2}1)$ and (101) for a) HH-A and b) FH-A tantalum structures……...81

Figure 4.24 - Calculated bandstructures obtained from Wannier functions (dashed lines) and GGA-PBE calculations (solid lines) Tantalum HH-A structure…….82

Figure 4.25 - Theoretical and experimental results for (a) Seebeck coefficient, (b) electrical conductivity (c) electronic component of thermal conductivity and (d) ZT versus temperature in the range of temperature 200 –1050K for HH-A tantalum structure. Experimental data extracted from Ref. Shan Li, et al [62]…….83

Figure 4.26 - Calculated (a) Seebeck coefficient, (b) electrical conductivity and (c) power factor for in HH-A structure, as a function of the chemical potentials for different temperatures……..84

LIST OF TABLES

Table 4.1 - Wyckoff positions for the atoms Co, Sn and Ta for each HH and FH structure. The 8c position is occupied only in FH case……48

Table 4.2 - Lattice parameter of Group VB alloys…….....49

Table 4.3 - Atomic and Pauling electronegativity [129]……..50

Table 4.4 - Local (m) and total (M) magnetic moments of the structures HH and FH for (Co-V-Sn) alloys from HSE06 (GGA-PBE) calculation. Δm represents the contribution of interstitial region of the crystal. Values of M in bold are in accordance with the Slater-Pauling rule……53

Table 4.5 - Band gap of VB Group alloys……56

Table 4.6 - Local (m) and total (M) magnetic moments of the structures HH and FH for (Co-Nb-Sn) alloys from HSE06 (GGA-PBE) calculation. Magnetic moments calculated with GGA-PBE for comparation. Δm represents the contribution of interstitial region of the crystal. Values of M in bold are in accordance with the Slater-Pauling rule……57

Table 4.7 - Local (m) and total (M) magnetic moments of the structures HH and FH for (Co-Ta-Sn) alloys from HSE06 (GGA-PBE) calculation. Magnetic moments calculated with GGA-PBE for comparation. Δm represents the contribution of interstitial region of the crystal. Values of M in bold are in accordance with the Slater-Pauling rule……61

Table 4.8 - Effective masses of CoVSn HH-A…….....66

Table 4.9 - Effective masses of CoNbSn HH-A……...69

Table 4.10 - Effective masses of CoTaSn HH-A…….....71

Table 4.11 - Bader Charge q (|e|) obtained from HSE06 calculations for vanadium alloys. Values in bold represent the atoms in the 4c/8c sites……...73

Table 4.12 - Bader Charge q (|e|) obtained from HSE06 calculations for niobium alloys. Values in bold represent the atoms in the 4c/8c sites……...76

Table 4.13 - Bader Charge q (|e|) obtained from HSE06 calculations for tantalum alloys. Values in bold represent the atoms in the 4c/8c sites……...79

LIST OF ACRONYMS AND ABBREVIATIONS

2D	Two Dimensions
BZ	Brillouin Zone
CCB	Conduction Band Bottom
COP21	21st Conference of the Parties
DOS	Density of States
DFT	Density Functional Theory
ELF	Electron Localization Function
FH	Full-Heusler
FEA	Free Electron Approximation
GGA	Generalized-Gradient Approximation
HF	Half-Metallic
HH	Half-Heusler
HSE06	Hybrid functional HSE06
KS	Kohn-Sham
LDA	Local Density Approximation
LSDA	Local Spin Density Approximation
MSMAs	Magnetic Shape Memory Alloys
mBJ	Modified Becke Johnson (mBJ)
PAW	Projector Augmented-wave
PBE	Perdew, Burke and Ernzerhof
PEDOT	Poly(3,4-ethylenedioxythiophene)
PCR	Polymerase Chain Reaction
PGEC	Phonon-Glass – Electron Crystal
PLEC	Phonon-Liquid Electron-Crystal
RTGs	Radioisotope Thermoelectric Generators
SOC	Spin-Orbit Coupling
TDOS	Density of States Total
VASP	Vienna ab-initio simulation package
VB	Elements of VB group: V, Nb and Ta
WF	Wannier function
MLWFs	Maximally Localized Wannier Functions
VBT	Valence Band Top

LIST OF SYMBOLS

S	Seebeck Coefficient
Π	Peltier Coefficient
I	Electric Current
ZT	Figure Merit
κ	Total Thermal Conductivity
κ_{lat}	Lattice (Phonon) Component of Thermal Conductivity
κ_{el}	Electronic Component of Thermal Conductivity
σ	Electronic Conductivity
T	Temperature Absolute
ΔT	Temperature Absolute Difference
L	Lorenz Number
η	Power Generation Efficiency
Ψ	Wave-function
$\vec{r}$	Electron Position Vector
N	Electron Number
e	Elementary charge
$\vec{R}$	Nucleus Position Vector
M	Atomic Nucleus Mass
m_0^*	Rest Electron Mass
$\hbar$	Planck constant divided by 2π
e	Elemental Charge
Z	Atomic Number
∇	Gradient Operator
∇^2	Laplacian Operator
$\sum \ldots$	Sum Symbol
$\int dr$	Integral Symbol
$\langle \Psi \vert L \vert \Psi \rangle$	Expectation value of L
$\langle L \rangle$	Expectation value of L
$\frac{d}{dx}$	Differential Operator
$\mathbf{T}$	Kinetic Energy Operator
$\mathbf{V_{ext}}$	External Potential

$\mathbf{V_{ee}}$	Electron-Electron Repulsion Potential
$\mathbf{V_{int}}$	Electron-Electron Interactions Potential
E_{II}	Nuclei-Nuclei Interaction
ρ	Density of charge
$\delta(r - r_i)$	Function Delta-Dirac
$F[f]$	Functional of function f
$\frac{\delta}{\delta f}$	Differential Operator to Functional
$F_{HK}[\rho(\vec{r})]$	Electronic Energies (Except External Potential)
$T_s[\rho(\vec{r})]$	Kinetic Energy of Electrons in the Non-Interacting System
$E_{Hartree}[\rho(\vec{r})]$	Hartree Energy
$E_{xc}[\rho(\vec{r})]$	Exchange-Correlation Energy
E_{II}	Nucleus-Nucleus Coulomb Interaction
θ_i^{KS}	i-th Kohn-Sham orbitals
$v_{xc}(\vec{r})$	Exchange-Correlation Potential
ϵ_{xc}	Exchange-Correlation Density
v_S	Effective Potential
H_{KS}	Kohn-Sham's Hamiltonian Operator
ϵ_i	i-th Kohn-Sham Orbitals Energy
ϵ_{xc}^{hom}	Exchange-Correlation Density to Homogeneous Gas
E_{xc}^{LDA}	Exchange-Correlation Energy to LDA approximation
E_{xc}^{GGA}	Exchange-Correlation Energy to GGA approximation
E_{xc}^{PBE}	Exchange-Correlation Energy to GGA-PBE approximation
ϵ_c^{hom}	Correlation Density to Homogeneous Gas
ϵ_x^{hom}	Exchange Density to Homogeneous Gas
u_{nk}	Bloch Periodic Function
w_0	Wannier function
$U_{mn}^{dis(k)}$	Matrix $N^{(k)} \times N$ states
$E_{n,k}$	Energy of the Band n at k
v_i	Band Velocity at (n, k)
μ	Potential Chemical
τ	Relaxation Time
Z_{VEC}	Number of Valence Electrons

q	Charge Bader
m^*	Effective mass
m^*_{DOS}	Density of States Effective Mass
N_d	Degeneracy Factor
E_c	Cohesive Energy
E_T	Total Energy
eV	eletron-Volt
Å	Angstrom
a	Lattice Parameter
a_{opt}	Optimized Lattice Parameter
P(n,k)	Permutation
E_f	Fermi Level
e_g, t_{2g}	Molecular Orbitals in Crystal Field Theory
m	Total magnetization
Δ_m	Contribution of the Interstitial Region of the Crystal to the Total Magnetic Moment
μ_B	Bohr magneton

SUMMARY

1– INTRODUCTION ..... **Error! Bookmark not defined.**
1.1 - Thermoelectric materials and figure of merit 19
1.2 - Heusler alloys 23
2 – THEORETICAL AND COMPUTATIONAL FOUNDATIONS 24
2.1- Quantum many bodies system 24
2.2- Density Functional Theory and Hohenberg–Kohn theorems 26
2.3- Density Functional Theory and self-consistent process 27
2.4- Exc approximations 30
2.4.1- LDA approximation 31
2.4.2- GGA approximation 31
2.4.3- GGA-PBE approximation 32
2.4.4 – Meta-GGA functional (mBJ) 33
2.4.4 – Hybrid functional (HSE06) 34
2.5- Pseudopotential 34
2.6- Brillouin Zone 36
2.7- VASP Package 36
2.8- Wannier special functions 37
2.9- Boltzwann computational package 38
2.9- Analysis tools for Chemical Bonds 39
2.9.1 Density of Charges 39
2.9.2 Electron Localization Function (ELF) 39
2.10 Effective Mass 42
2.11 Spin–orbit coupling (SOC) 44
2.12 Cohesive Energy (E_c) 44
3 – METHODOLOGY 45
4 – RESULT AND DISCUSSION 46
4.1 Structures 46
4.1.1 Vanadium alloys 48
4.1.2 Niobium alloys 50
4.1.3 Tantalum alloys 51
4.2 Electronic and Magnetic properties 52
4.2.1 Vanadium alloys 52
4.2.2 Niobium alloys 57

4.2.3 Tantalum alloys 61
4.3 Effective Mass and SOC 65
4.3.1 Vanadium alloys 65
4.3.2 Niobium alloys 67
4.3.3 Tantalum alloys 70
4.4 Chemical Bonds 72
4.4.1 Vanadium alloys 72
4.4.2 Niobium alloys 75
4.4.3 Tantalum alloys 78
4.5 Thermoelectric Properties 81
5 – CONCLUSION 85
6 – REFERENCES 85
SCIENTIFIC ACTIVITIES 99

1 – INTRODUCTION

The use of electrical, thermal, mechanical or any other type of energy has been a key factor for the survival and development of the human race [2]. Its use is crucial for the progress and improvement of social welfare, in fact, countries that have access to modern electricity energy matrices are associated with poverty reduction and improvements in the Human Development Index [3,4]. In addition, to the democratization of access to energy sources, another current concern is the search for renewable and clean energy matrices, that do not emit polluting substances. At the 21st Conference of the Parties (COP21), the Paris Agreement was signed, which established goals for countries to reduce greenhouse gas emissions and outline prospects for the impact of new technologies on the decarbonization of energy matrices [5]. Beyond the predominance of non-clean and non-renewable sources for power generation, energy conversion efficiency is another problem. Currently, less than 40% of the energy used is effectively converted into electricity [6,7].

As shown in Figure 1.1 (a), the global consumption of energy increases year by year, being the fossil fuel (oil, natural gas and coal) the main source. These energy matrices are the main responsible for climate change, in reason of release of SO_x, NO_x and CO_2 emissions to atmosphere, and also have a high impact in the world economy [8–11]. On the other hand, the use of renewable energy sources also increased, mainly after 2010, as shown in Figure 1.1(b). Besides of hydropower generation, new technologies known as “green energies” [12] have contributed to global energy consumption and are a new frontier to economic development [13–15].

As well known, during the process of converting primary energy into electrical energy, a large loss occurs. From this perspective, thermoelectric materials are promising, as they can be used to build devices capable of converting thermal energy into electrical energy (and vice versa), without emitting pollutants and offering longer usage time.

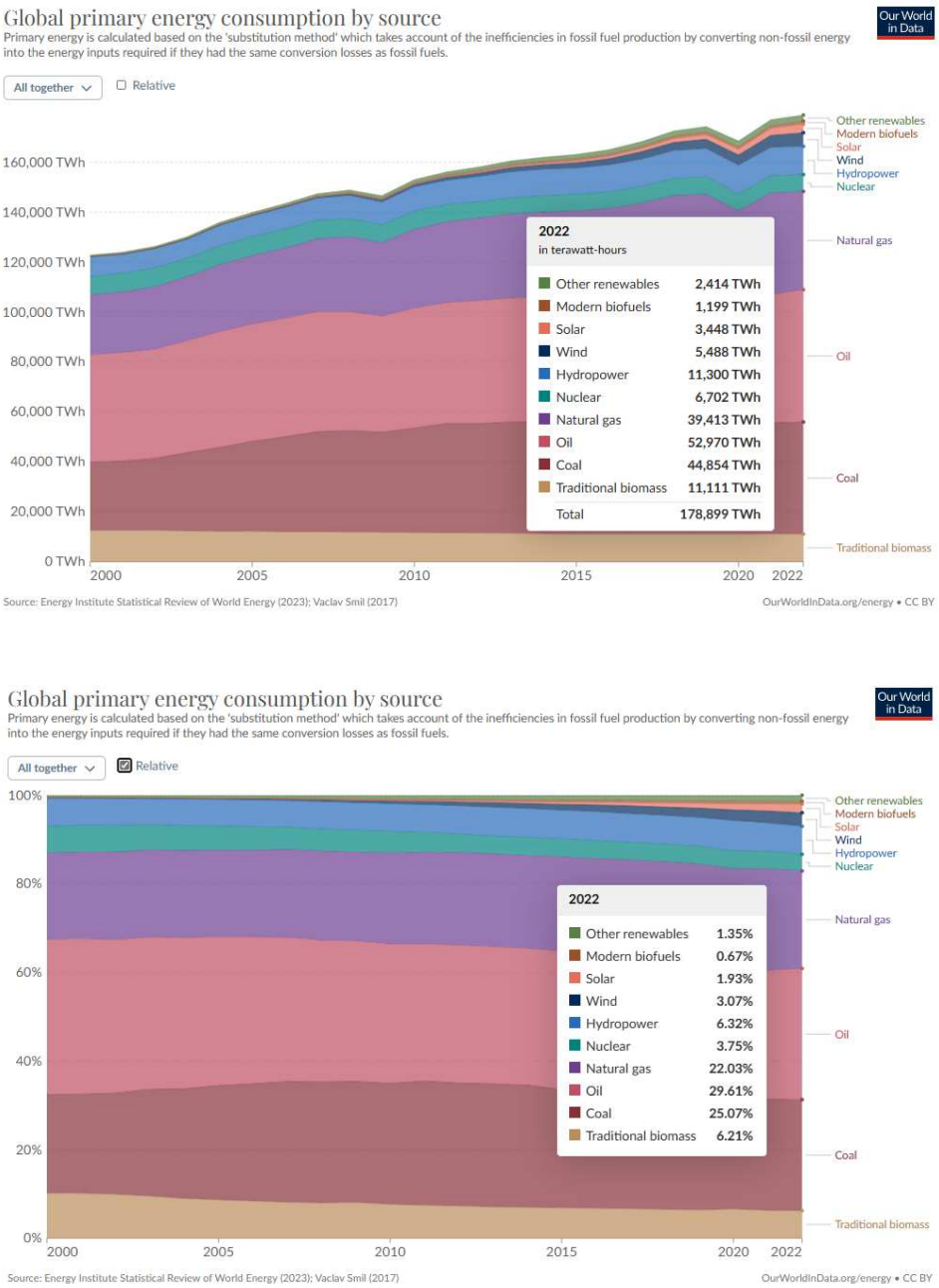

Figure 1.1: Global primary energy consumption by source from 2000 to 2022 (a) absolute numbers (b) relative numbers [1].

1.1 - Thermoelectric materials and figure of merit

The thermoelectric phenomenon was first reported by T. J. Sebbeck in 1822 [16,17], when he experimentally observed the needle movement of a compass, when it was brought together by two different conductors placed together and exposed to a temperature difference at the junctions. The needle movement occurred in reason of electromagnetic field created from electrical current generated by temperature difference. In 1834, J. C. Peltier [18] observed an

inverse phenomenon, where an electrified junction of two different semiconductors caused a temperature difference at the junctions. However, it was only in 1851 that these two observations were correlated and better explained by W. Thomson (Lord Kevin) [19], who predicted a third phenomenon. Therefore, the conversion of thermal energy to electrical energy is known as the Seebeck Effect; the conversion of electrical energy into thermal energy as the Peltier Effect; and the concomitant Seebeck and Peltier effects as Thomson Effect.

Modern thermoelectric devices, known as thermocouple, are formed by a pair of n- and p-type semiconductors [20]. Figure 1.2 (a) depicts the Effect Seebeck in a thermocouple, where the temperature difference creates an electric field in opposite directions for each semiconductor. This create a potential difference between them and generates an electric current when the circuit is closed. It was considered a current of positive carries. Also, the potential difference, in terms of absolute temperature T, can be given by:

$$\frac{\mathrm{d\,V}}{\mathrm{dT}} = \mathrm{S_a} - \mathrm{S_b} = \mathrm{S_{ab}} \qquad 1.1$$

which $\mathrm{S_a}$and $\mathrm{S_b}$ are absolute *Seebeck coefficient* of materials *a* and *b*, respectively, while S_{ab} is the relative Seebeck coefficient of the thermocouple. For p-type semiconductor the absolute Seebeck coefficient is positive ($\mathrm{S} > 0$) otherwise, negative ($\mathrm{S} < 0$) for n-type.

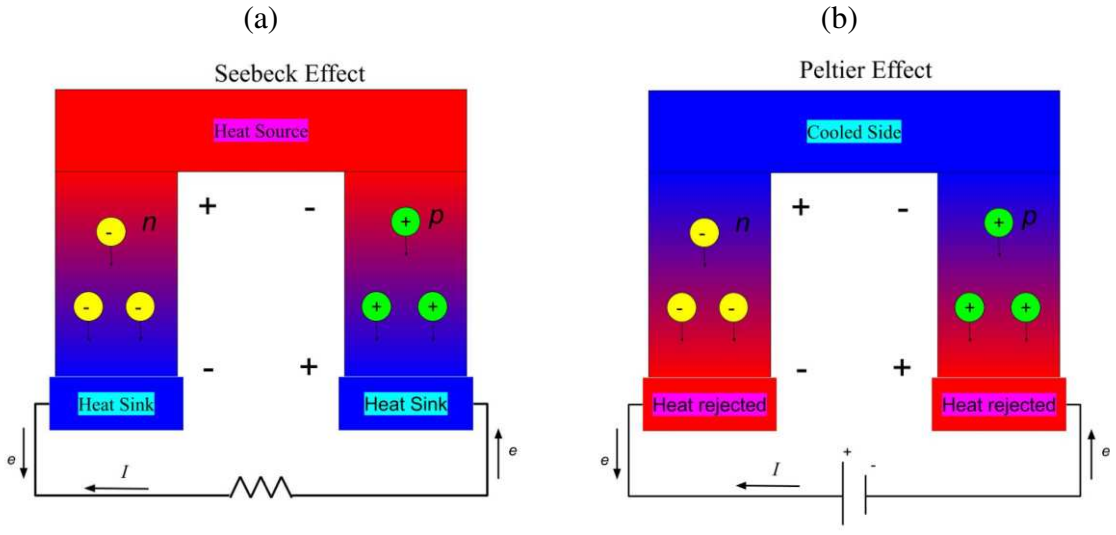

Figure 1.2: Representation of the circuits that describe the (a) Seebeck and (b) Peltier effects.

On the other hand, the Peltier effect is observed when a current I is present in a circuit, producing a cooling of one junction and the heating of the other, as shown in Figure 1.2 (b). This rate of heat is given by [21]:

$$\frac{d\,Q}{dt} = (\Pi_a - \Pi_b)I = \Pi_{ab}I \qquad 1.2$$

which $\Pi_a$and Π_b are the absolute *Peltier coefficient* of materials *a* and *b*, while Π_{ab} is the relative Peltier coefficient of thermocouple.

The Thomson effect occurs when electric current and a temperature gradient co-exist in homogeneous conductor. This causes a reversible cooling or heating. However, this effect has little impact when the gradient of temperature is not large and generally is negligible [21]. Furthermore, the relationship between the Peltier and Seebeck coefficients is given by:

$$\Pi_{ab} = S_{ab}T \qquad 1.3$$

The efficiency of a thermoelectric generator or a cooler is related to the parameter known as **Figure of Merit** [20]:

$$Z = \frac{\sigma S^2}{\kappa} \qquad 1.4$$

where S is the Seebeck coefficient, σ the electrical conductivity, and κ the thermal conductivity. The Power Factor is defined as $PF = \sigma S^2$. The thermal conductivity is usually written as the sum of its electrical (κ_{el}) and lattice (κ_{lat}) components. The electronic component of thermal conductivity arises of energy transported by electrons as heat and can be estimated from the Wiedemann Franz relation [22]:

$$\kappa_{ele} = L\sigma T \qquad 1.3$$

where $L = 2.44 \times 10{-}8\ V^2K^{-2}$ is the Lorenz Number and T is absolute temperature. While the lattice component (κ_{lat}) can be explained from phonon theory. Commonly, the figure of merit is multiplied by the temperature of operation, i.e., ZT, being dimensionless. Additionally, the figure of merit of the thermocouple is given by an average ZT of the materials.

The power generation (η_{pg}) and cooler (η_{cooler}) efficiency can be defined as [23]:

$$\eta_{pg} = \frac{T_h - T_c}{T_h}\left[\frac{\sqrt{1 + ZT_{ave}} - 1}{\sqrt{1 + ZT_{ave}} - \frac{T_c}{T_h}}\right] \qquad 1.6$$

$$\eta_{cooler} = \frac{T_h}{T_h - T_c}\left[\frac{\sqrt{1 + ZT_{ave}} - \frac{T_h}{T_c}}{\sqrt{1 + ZT_{ave}} + 1}\right] \qquad 1.7$$

$$ZT_{ave} = \frac{1}{T_h - T_c}\int_{T_c}^{T_h} ZT\ dT \qquad 1.8$$

where T_h and T_c are the temperature of the hot, cold ends; while T_{ave} is the average temperature. For $ZT_{ave} \rightarrow \infty$ the term in brackets is equal to 1, that is, the thermoelectric device has a maximum efficiency. For the power generation, the maxim efficiency is given by Carnot efficiency: $\frac{T_h - T_c}{T_h}$.

The great challenge for the development of high-efficiency thermoelectric devices is to find materials that have low thermal conductivity, high Seebeck coefficient and electrical conductivity. Comparatively, for ZT_{ave} = 3.0 and ΔT= 400K, $\eta_{pg} \approx 25\%$; and for ZT_{ave} = 3.0 and ΔT = 20 K, $\eta_{cooler} \approx 6\%$ [23].

Commercially, bismuth telluride (Bi_2Te_3) is the most used thermoelectric for refrigeration around room temperature, with ZT ≈ 1.1. This value can be improved through doping process [24,25]. Materials as lead telluride PbTe; tellurium, antimony, germanium and silver alloys; and silicon–germanium solid solution $Si_{1-x}Ge_x$ are used in thermoelectric devices as well as in studies for development of radioisotope thermoelectric generators (RTGs) for spatial applications [26]. Due to the decrease in the cost of semiconductor production, the integration of thermoelectric devices in other areas has increased considerably, such as: thermoelectric devices keep laser diodes at constant temperature to stabilize operating wavelengths; biological assaying for development of polymerase chain reaction (PCR), and the use of thermoelectric devices in PCR for control thermally the quantities of enzymatic reactions in temperature cycles [27].

Currently, several materials/concepts are being studied for the development of high-performance thermoelectric materials, such as: i) phonon-glass – electron crystal (PGEC) in which heavy atoms would be allocated in vibrating "cages", spreading the phonons, but allowing good conductivity [28]; phonon-liquid electron-crystal (PLEC) as a new strategy of decreasing the thermal conductivity of the lattice through a liquid type behavior of superconductors [29]. ii) *2D materials* based on Na_xCoO_2, In_4Se_3, SnSe, Bi-SnSe and Na-SnSe that can reach ZT ≈ 2 [30]. iii) *superlattices* that are formed by periodic arrangement of successive adjacent layers, which can scatter phonons and ultimately decreases thermal conductivity, and increases S coefficient by increasing the density of states at the Fermi level [31]. Bi_2Te_3/Sb_2Te_3, Bi_2Te_3/Bi_2Se_3 as well as PbSeTe/PbTe are among the structures studied [32]. iv) O*rganic compounds* that has the advantage of being non-toxic, enabling recycling, easy modeling, carbon is abundant; however, they have the disadvantage of degrading at high temperatures [33]. Some examples are poly(3,4-ethylenedioxythiophene) (PEDOT), polythiophenes, polyacetylenes and polyanilines [34]; v) materials with low thermal

conductivity are promising thermoelectric application, such as the chalcogenides [35]; and vi) Heusler alloys that present promising characteristics with high power factor, thermal and mechanical stability and are composed of elements abundant in nature [36,37].

1.2 - Heusler alloys

Heusler alloys were discovered in 1903 by F. Heusler [28], when he was studying the compound Cu_2MnAl, which is currently classified as a Full-Heusler alloy (FH). Details of the crystal structure of Heusler alloys will be presented in details in Section 4.1. Ternary Heusler alloys can be formed from several elements of periodic table [38], and are studied for application in several areas, such as, spintronic [39] magnetoelastic [40], topological insulators [41], magnetic shape memory alloys (MSMAs) [42] and thermoelectric.

In the thermoelectric context, materials that have narrow bandgaps and density of states around the Fermi level generally have a higher power factor for high temperatures, thus being promising compounds for this type of application. [43]. In this scenario, the alloys called Half-Heusler (HH) were studied: (Zr/Hf/Ti)NiSn with ZT > 1.2 (for T > 700K) [44,45], Ti-doped FeNbSb with ZT > 1 (T ≈ 1000 K) [46]. $FeNb_{1-x}Ti_xSb$ presented ZT of 1.1 at 1100K with x = 0.02 [46]. Other Heusler structures with various combinations of elements can lead to both p-type and n-type thermoelectric materials. [47–49]

In the literature [50] , the synthesis of CoVSn revealed a low ZT ≈ 0.007 in reason of formation of intermetallic phases. On the other hand, CoNbSn alloys [51–60] doped with different elements such as Hf, Sb, Pt, Ti, Sb can reach ZT ≈ 0.6. Kimura and Tamura [52] reported an interesting increase in ZT in $Co_{1+x}NbSn$ compound, when the concentration of Co was increased. The HH alloy CoTaSn was successfully synthesized [61] and had its thermoelectric properties studied by S. Li et al. [62], presenting ZT ≈ 0.01. For the complex compound, $Ta_{0.6}Nb_{0.4}CoSn_{1-x}Sb_x$, ZT = 0.75 for 973K and x = 0.06.

Theoretical study of physicochemical properties of Heusler alloys is very useful for understanding and developing of high-performance thermoelectric devices. From first principle calculations, using the accurate HSE06 hybrid functional, within Density Functional Theory (DFT), this work presents the results for several properties of Co-*VB*-Sn (*VB* = V, Nb, Ta) Heusler alloys. The results are presented for: lattice parameter; cohesion energy; density of states; band structures; band gap; magnetic moments; effective masses; Bader Charges, ELF functions; Charge Densities; chemical bonds; and thermoelectric parameters. The results were compared to the available experimental data.

2 – THEORETICAL AND COMPUTATIONAL FOUNDATIONS

2.1- Quantum many bodies system

A quantum system that involves the interaction of many particles can have its chemical physical properties analyzed based on the knowledge of its quantum states. For a given quantum system, the time-independent Schrödinger equation takes the following form:

$$\mathbf{H}\Psi(\overrightarrow{r_1},\dots,\overrightarrow{r_N}) = \mathrm{E}\Psi(\overrightarrow{r_1},\dots,\overrightarrow{r_N}) \qquad 2.1$$

where **H** is the Hamiltonian operator of the system, E are the energy eigenvalues and $\Psi(\overrightarrow{r_1},\dots,\overrightarrow{r_N})$ are the wave functions. The Hamiltonian operator for a quantum system of one or more atoms can be given by [63]:

$$\boldsymbol{H} = -\frac{\hbar^2}{2m_0^*}\sum_i \nabla_i^2 - \sum_{i,I}\frac{Z_I e^2}{|\overrightarrow{r_i}-\overrightarrow{R_I}|} + \frac{1}{2}\sum_{i\neq j}\frac{e^2}{|\overrightarrow{r_i}-\overrightarrow{r_j}|} - \\ -\sum_I \frac{\hbar^2}{2M_I}\nabla_i^2 + \frac{1}{2}\sum_{i\neq j}\frac{Z_I Z_J e^2}{|\overrightarrow{R_I}-\overrightarrow{R_J}|}. \qquad 2.2$$

where r_i and R_I are the positions of the i-th electron and I-th nucleus, respectively; M_I is the I-th atomic nucleus mass; m_0^*, $\hbar$ and e are the rest mass of electron ($9.109x10^{-31}$ Kg), the Planck constant divided by 2π ($1.054x10^{-34}$J.s) and the elemental charge ($1.602x10^{-19}$C), respectively. The first term of equation 2.2 refers to the electronic kinetic energy, the second to the nucleus-electron attraction, the third to the electron-electron repulsion, the fourth to the kinetic energy of the nucleus and the last energy to the nucleus-nucleus repulsion.

The complexity of the Hamiltonian operator makes Equation 2.1 very difficult to solve, that is, only numerical solutions are possible. Generally, the first simplification is to consider atomic nuclei as being infinitely more massive than electrons, so that the approximation $1/M_I \longrightarrow 0$ can be adopted, which makes the fourth term of Equation 2.2 negligible. This simplification is known as the Born-Oppenheimer (adiabatic) approximation, where atomic nuclei can be considered as static, and R_I are parameters rather than variables. Thus, the Hamiltonian described by equation 2.2 can be simplified to:

$$\mathbf{H} = \mathbf{T} + \mathbf{V_{ext}} + \mathbf{V_{int}} + \mathbf{E_{II}}\,. \qquad 2.4$$

In which, using the Hartree atomic units $m_0^* = \hbar = e = \frac{4\pi}{\varepsilon_0} = 1$, are written as:

$$\mathbf{T} = -\frac{1}{2}\sum_{i} \nabla_i^2 ,$$

$$\mathbf{V_{ext}} = -\sum_{i,I} \frac{1}{\left|\overrightarrow{r_i} - \overrightarrow{R_I}\right|},$$

$$\mathbf{V_{int}} = \frac{1}{2}\sum_{i\neq j} \frac{1}{\left|\overrightarrow{r_i} - \overrightarrow{r_j}\right|},$$

$$\mathbf{E_{II}} = \frac{1}{2}\sum_{i\neq j} \frac{1}{\left|\overrightarrow{R_I} - \overrightarrow{R_J}\right|} = \text{constant} \qquad 2.3$$

where **T** is the **kinetic energy** operator, $\mathbf{V_{ext}}$ is the **external potential**, which is the sum of all nucleus-electron interactions, $\mathbf{V_{int}}$ represents the electron-electron interactions, and $\mathbf{E_{II}}$ is the nuclei-nuclei interaction. This term can be considered constant and added in the final result, in reason of Born-Oppenheimer approximation.

Even considering the adiabatic approximation, the many-body problem remains difficult to solve due to the electron-electron interaction term, which does not allow us to propose a separation of variables to solve Equation 2.1. In this context, the *Density Functional Theory* (**DFT)** emerged, which proposes the study of a given quantum system based on the density of charge of its ground state (ρ_0).

Considering the density operator as:

$$\boldsymbol{\rho}(\vec{r}) = \sum\nolimits_{i=1,N} \delta(r - r_i) \qquad 2.6$$

the density of particles $\rho(\vec{r})$ can be written by the expectation value of $\boldsymbol{\rho}(\vec{r})$ [64]:

$$\rho(\vec{r}) = \frac{\langle\Psi|\boldsymbol{\rho}(\vec{r})|\Psi\rangle}{\langle\Psi|\Psi\rangle} = N\frac{\sum_{\text{all spins}}\int |\Psi(\vec{r},\vec{r}_2,\vec{r}_3 \dots \vec{r}_n)|^2 \, d\vec{r}_2 d\vec{r}_3 \dots d\vec{r}_N}{\int |\Psi(\vec{r}_1,\vec{r}_2,\vec{r}_3 \dots \vec{r}_N)|^2 \, d\vec{r}_1 d\vec{r}_2 d\vec{r}_3 \dots d\vec{r}_N} \qquad 2.6$$

So, the total energy is:

$$E = \langle\Psi|\mathbf{H}|\Psi\rangle = \langle\mathbf{T}\rangle + \int \rho(\vec{r})\mathbf{V_{ext}}\, dr^3 + \langle\mathbf{V_{int}}\rangle + E_{II} \qquad 2.7$$

where the external potential is given by the integral over the density functional and E_{II} is the nucleus-nucleus coulomb interaction.

2.2- **Density Functional Theory and Hohenberg–Kohn theorems**

The pioneering development of DFT is due to the work of Hilleth Thomas and Enrico Fermi who proposed in 1927 to analyze a homogeneous and no-interacting electron gas system, that satisfied Fermi's statistics. In this analysis, the kinetic energy of electrons is approximated as a function of $\rho(\vec{r})$**,** and the terms of *exchange* and *correlation* between electrons are omitted. The *exchange-correlation* term refers to others electronic interactions. Later, these terms were included by Paul Dirac in 1930, when he formulated the local approximation to the *exchange* term*,* and still in use today [63,65]. Modern DFT is essentially based on two theorems proposed by P. Hohenberg and W. Kohn at 1964 [66], that is:

Theorem I: *For a given quantum system of interacting particles in an external potential* $\boldsymbol{V_{ext}}(\vec{r}_i)$*, this potential is determined unambiguously by the ground state particle density* $\rho_0(\vec{r})$**.**

This theorem implies that all properties of a given quantum system can be obtained from $\rho_0(\vec{r})$. On the other hand, the proof of this theorem is based on the principle of reduction to absurdity [64]. Two external potentials $\mathbf{V_{ext,1}}(\vec{r}_i)$ and $\mathbf{V_{ext,2}}(\vec{r}_i)$ that differ from each other by a constant must designate two different Hamiltonian operators $\mathbf{H}_1$ and $\mathbf{H}_2$ and consequently two different wave functions Ψ_1 and Ψ_2. The premise is that both potentials lead to the same particle density in the ground state $\rho_0(\vec{r})$. Based on the variational principle, for a fundamental non-degenerate state, $\langle\Psi|\mathbf{H}|\Psi\rangle > E_0$, if Ψ is an eigenstate of $\mathbf{H}$. Therefore:

$$E_1 = \langle\Psi_1|\,\mathbf{H}_1|\,\Psi_1\rangle < \langle\,\Psi_2|\,\mathbf{H}_1|\,\Psi_2\rangle. \tag{2.8}$$

The last term can be written as:

$$\begin{aligned}\langle\,\Psi_2|\,\mathbf{H}_1|\,\Psi_2\rangle \;&=\; \langle\,\Psi_2|\,\mathbf{H}_2|\,\Psi_2\rangle \;+\; \langle\,\Psi_2|\,\mathbf{H}_1 - \;\mathbf{H}_2|\,\Psi_2\rangle \\ &= E_2 \;+ \int \rho_0(\vec{r})\big[\mathbf{V_{ext,1}} - \mathbf{V_{ext,2}}\big]\,dr^3\end{aligned} \tag{2.9}$$

Thus,

$$E_1 \;< E_2 \;+ \int \rho_0(\vec{r})\big[\mathbf{V_{ext,1}} - \mathbf{V_{ext,2}}\big]\,dr^3. \tag{2.10}$$

Similarly:

$$E_2 < E_1 + \int \rho_0(\vec{r})\left[\mathbf{V_{ext,2}} - \mathbf{V_{ext,1}}\right] dr^3. \quad 2.11$$

Comparing equations 2.10 and 2.11 we arrived at:

$$E_1 + E_2 < E_1 + E_2 \quad 2.12$$

which is a false inequality. Thus, the premise that the same density $\rho_0(\vec{r})$ can set two potentials $\mathbf{V_{ext,1}}(\vec{r}_i)$ and $\mathbf{V_{ext,2}}(\vec{r}_i)$ it's false, as we wanted to demonstrate. The validity of this theorem for the degenerate case can be found in the Parr and Yang [67] work.

Theorem II: A universal functional of the energy *E[ρ($\vec{r}$)] can be written, which is valid for any external potential* $\boldsymbol{V_{ext}}(\vec{r}_i)$. *The value of the global minimum for the functional E[ρ($\vec{r}$)] will be defined by the density of the ground state* $\rho_0(\vec{r})$.

The proof of this theorem is given from Equation 2.7, written in terms of density:

$$\begin{aligned} E[\rho(\vec{r})] &= \langle \mathbf{T}[\rho(\vec{r})] \rangle + \int \rho(\vec{r}) \mathbf{V_{ext}}\, dr^3 + \langle \mathbf{V_{int}}[\rho(\vec{r})] \rangle + \mathbf{E_{II}} \\ &= \mathbf{F_{HK}}[\rho(\vec{r})] + \int \rho(\vec{r}) \mathbf{V_{ext}}\, dr^3 + \mathbf{E_{II}} \end{aligned} \quad 2.13$$

where the functional $\mathbf{F_{HK}}[\rho(\vec{r})]$ is defined as electronic energies except those that depend on the external potential.

Considering $\rho_0(\vec{r})$ associated with a potential $\mathbf{V_{ext}}(\vec{r}_i)$**,** which leads to a Hamiltonian **H** and an eigenstate Ψ_0. And $\rho_1(\vec{r})$ as another density that takes a different eigenstate Ψ_1. Therefore, by the variational principle:

$$E_0 = \langle \Psi_0 | \mathbf{H} \mid \Psi_0 \rangle < \langle \Psi_1 | \mathbf{H} \mid \Psi_1 \rangle = E_1. \quad 2.14$$

Therefore, the energy of the fundamental state defined by:

$$E_0 = \langle \Psi_0 | \mathbf{H}_1 | \Psi_0 \rangle \quad 2.15$$

it is necessarily the energy that minimizes the functional $E[\rho(\vec{r})]$.

2.3- Density Functional Theory and self-consistent process

Although Hohenberg–Kohn's theorems present the possibility of describing a quantum system based on the density of the ground state, there is no indication of how to perform these calculations. So, how to solve the many-body problem based on DFT is a big task. Thus, in 1965, W. Kohn and L. J. Sham (KS) [68] proposed a method that allows many-body problem

to be solved more easily using an auxiliary system of equations. That is, the set of single-particle KS equations includes many-body effects.

The KS model assumes that the external potential, $\mathbf{V_{ext}}$ in Equation 2.4, will depend on the configuration of the system. However, the electron-electron repulsion $\mathbf{V_{ee}}$ and the kinetic energy of electrons **T** have the same mechanism of action on all systems. Therefore, the system is analyzed with a set of single-particles, but taking into account the many-body effects, then equation 2.7 can be rewritten as,

$$E[\rho(\vec{r})] = T_s[\rho(\vec{r})] + \int \rho(\vec{r})\mathbf{V_{ext}}\, dr^3 \; + \\ + E_{Hartree}[\rho(\vec{r})] + E_{xc}[\rho(\vec{r})] + E_{II} \qquad 2.16$$

where the term $T_s[\rho(\vec{r})]$ is the kinetic energy of electrons in the **non-interacting** system [64]; $\mathbf{V_{ext}}$ is the external potential taking into account the nuclei and other external fields; E_{II} is due nucleus-nucleus interaction; $E_{Hartree}$ corresponds to the classical coulomb electron-electron interaction, defined as:

$$E_{Hartree} = \int \frac{\rho(\vec{r})\rho(\vec{r}')dr^3 dr'^3}{|\vec{r} - \vec{r}'|} \qquad 2.17$$

and $E_{xc}[\rho(\vec{r})]$ take into account the many-body effects, including exchange effects due to antisymmetric principle and correlation effects due to the fact that electron movement is correlated.

To minimize the energy presented in Equation 2.16, the Euler-Lagrange multiplier method is used. Considering N electrons,

$$N = \int \rho(\vec{r})dr^3, \qquad \rho(\vec{r}) \geq 0 \qquad 2.18$$

and according to the stationary principle:

$$\delta\{E[\rho(\vec{r})] - N\epsilon\} = 0 \qquad 2.19$$

where ϵ is the energy of electrons described in the orbitals.

For a system of N electrons, the density can be given by a summation of N self-functions θ_i^{KS} of one-electron:

$$\rho(\vec{r}) = \sum_{i=1}^{N} \left|\theta_i^{KS}\right|^2. \qquad 2.20$$

Initially, this equation is defined only to the system of non-interacting electrons, since the eigenfunctions θ_i^{KS} are defined to a Hamiltonian to this type of system [64]. The eigenfunctions θ_i^{KS} are known as Kohn-Sham orbitals. As density depends on the eigenfunctions θ_i^{KS}, the electronic density can be minimized by minimizing θ_i^{KS}.

Writing $T_s[\rho(\vec{r})]$ in terms of Kohn-Sham orbitals:

$$T_s[\rho(\vec{r})] = \sum_{i=1}^{N} \int \nabla\theta_i^{KS} \nabla\left(\theta_i^{KS}\right)^* dr^3 \qquad 2.21$$

The variation of this term implies:

$$\frac{\delta T_s[\rho(\vec{r})]}{\delta\rho(\vec{r})} = -\nabla^2\, \theta_i^{KS}. \qquad 2.22$$

In this way, we can write:

$$\left\{-\nabla^2 + 2\int \frac{\rho(\vec{r}')dr'^3}{|\vec{r}-\vec{r}'|} + \int\int \frac{\rho(\vec{r})\rho(\vec{r}')dr^3dr'^3}{|\vec{r}-\vec{r}'|} + v_{xc}(\vec{r})\right\}\theta_i^{KS} = \epsilon_i\theta_i^{KS} \qquad 2.23$$

where exchange-correlation potential $v_{xc}(\vec{r})$ is given by,

$$v_{xc}(\vec{r}) = \frac{\delta E_{xc}[\rho(\vec{r})]}{\delta\rho(\vec{r})} \qquad 2.24$$

and the exchange-correlation energy is:

$$E_{xc}[\,\rho(\vec{r})\,] = \int \rho(\vec{r})\epsilon_{xc}\left(\rho(\vec{r})\right) dr^3 \qquad 2.25$$

considering $\epsilon_{xc}\left(\rho(\vec{r})\right)$ as the exchange-correlation density.

The Equation 2.23 can be rewritten as:

$$\{-\nabla^2 + v_s\}\theta_i^{KS} = \mathbf{H}_{KS}\theta_i^{KS} = \epsilon_i\theta_i^{KS} \qquad 2.26$$

in which v_S is known as an effective potential and $\mathbf{H}_{KS}$ as Kohn-Sham's Hamiltonian operator. Thus, θ_i^{KS} eigenfunctions are obtained from a system of N electrons that do not interact, but they are under the influence of an effective potential that describes the many-body system. Moreover, Kohn-Sham orbitals also consider the exchange-correlation electron-electron interaction, which is included in the effective potential through the $v_{xc}(\vec{r})$.

The solution of Kohn-Sham equations can be obtained from a self-consistent process, starting from an initial (assumption) electronic density (ρ_0). This self-consistent process is described in Figure 2.1. From ρ_0, the kinetic term ($-\nabla_1^2$) and KS potential (v_s) are determined and then the Kohn-Shan orbitals (θ_i^{KS}) obtained. From θ_i^{KS}, a new charge density ρ and

consequent energy E[ρ] is obtained in a cyclic process where the last charge density ρ is used as the input parameter for the next cycle. The system is considered converged when the energy difference between the last two cycles reaches a certain minimum value.

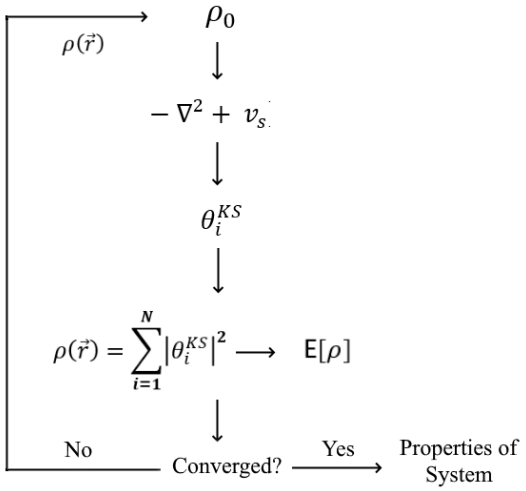

Figure 2.1: Kohn-Sham self-consistent scheme.

It is also worth mentioning that it is not possible to attribute physical meaning to Kohn-Sham orbitals θ_i^{KS} and their eigenvalues ϵ_i. Its use is restricted only to the determination of density $\rho(\vec{r})$ in the self-consistent process. To define the exchange-correlation term $v_{xc}(\vec{r})$, several important approximations were developed, in the next section some of them are presented.

2.4- E_{xc} approximations

Initially, the E_{xc} term can be approximated as:

$$E_{xc}[\rho(\vec{r})] = \int \rho(\vec{r})\, \epsilon_{xc}\, dr^3 \qquad 2.27$$

where ϵ_{xc} is the exchange-correlation energy for each electron $\rho(\vec{r})$-dependent in the vicinity of the point $\vec{r}$. In these terms, two important approximations are presented below, called Local Density Approximation (LDA) and Generalized-Gradient Approximation (GGA).

2.4.1- LDA approximation

The *Local Density Approximation* (LDA) considers a homogeneous electron gas. This gas (commonly known as "Jellium") is electrically neutral. Within this approach, the Equation 2.27 is written in terms of $\epsilon_{xc}^{hom}[\rho(\vec{r})]$:

$$E_{xc}^{LDA}[\rho(\vec{r})] = \int \rho(\vec{r})\, \epsilon_{xc}^{hom}[\rho(\vec{r})]\, dr^3. \quad 2.28$$

Thus, $\epsilon_{xc}^{hom}[\rho(\vec{r})]$ is separated in relation to their terms of exchange and correlation separately:

$$\epsilon_{xc}^{hom}[\rho(\vec{r})] = \epsilon_{c}^{hom}[\rho(\vec{r})] + \epsilon_{x}^{hom}[\rho(\vec{r})] \quad 2.29$$

where,

$$\epsilon_{x}^{hom}[\rho(\vec{r})] = -3\left(\frac{3\rho(\vec{r})}{8\pi}\right)^{\frac{1}{3}} \quad 2.30$$

and,

$$E_{x}^{LDA}[\rho(\vec{r})] = -\frac{3}{4}\left(\frac{3}{\pi}\right)^{\frac{1}{3}} \int [\rho(\vec{r})]^{\frac{4}{3}}\, dr^3. \quad 2.31$$

The term $\epsilon_{c}^{hom}[\rho(\vec{r})]$ can be obtained mainly through computational approaches or even complicated analytical equations.

An improvement in the LDA approach can be achieved considering spin polarization, called Local Spin Density Approximation (LSDA). In that case, $\epsilon_{xc}^{hom}\left[\rho(\vec{r})_{up}, \rho(\vec{r})_{down}\right]$ and $E_{xc}^{hom}\left[\rho(\vec{r})_{up}, \rho(\vec{r})_{down}\right]$ are written in terms of the individual of each spin. The total density will be $\rho(\vec{r}) = \rho(\vec{r})_{up} + \rho(\vec{r})_{down}$.

2.4.2- GGA approximation

The LSDA has been improved by several GGA approximations. In 1986, Perdew and Wang [69] considered that electron-correlation-exchange energy is also functional of the density gradient. $\epsilon_{xc}[\rho(\vec{r}), |\nabla\rho(\vec{r})|]$, where the equation 2.27 is rewritten as:

$$E_{xc}^{GGA}\left[\rho(\vec{r})_{up}, \rho(\vec{r})_{down}\right] = \int \rho(\vec{r})\epsilon_{xc}\left[\rho(\vec{r})_{down}, \rho(\vec{r})_{up}, |\nabla\rho(\vec{r})|_{down}, |\nabla\rho(\vec{r})|_{up}\right] dr^3 \quad 2.32$$

considering the spin polarization.

The $E_{xc}^{GGA}[\rho(\vec{r})_{up}, \rho(\vec{r})_{down}]$ is decomposed in its exchange and correlation components:

$$E_{xc}^{GGA} = E_{x}^{GGA} + E_{c}^{GGA}. \quad 2.33$$

Usually, the name of the functional is denoted by the initials of its authors along with the year in which they were proposed.

2.4.3- GGA-PBE approximation

Nowadays, the GGA established by authors Perdew, Burke and Ernzerhof in 1996 [70] is widely used in solids calculations, and called as GGA-PBE. The correlation term is given by:

$$E_{c}^{PBE}[\rho(\vec{r})_{up}, \rho(\vec{r})_{down}] = \int \rho(\vec{r})[\, \epsilon_{c}^{hom}(r_s, \xi) + H(r_s, \xi, t)]dr^3 \quad 2.34$$

where $\rho(\vec{r}) = \rho(\vec{r})_{up} + \rho(\vec{r})_{down}$, r_s is known as a local Seitz radius, defined as $r_s^3 = \frac{4\pi\,\rho(\vec{r})}{3}$, $\xi = \frac{\rho(\vec{r})_{up} - \rho(\vec{r})_{down}}{\rho(\vec{r})}$ considering spin polarization, and $t = \frac{|\nabla\rho(\vec{r})|}{2\phi k_s \rho(\vec{r})}$ is a gradient of density, where $\phi = \frac{(1+\xi)^{\frac{2}{3}} + (1-\xi)^{\frac{2}{3}}}{2}$ and $k_s = \sqrt{4k_F/\pi(\hbar^2/me^2)}$.

The gradient H was made using three conditions:

1 – At the limit $t \to 0$, H can be approximated in a second-order expansion:

$$H \to 0.066725\,\frac{e^2\phi^3 t^2}{a_0} \quad 2.35$$

considering high densities limits ($k_s \to 0$) and $a_0 = \frac{\hbar^2}{me^2}$.

2 - At the limit $t \to \infty$:

$$H \to -\,\epsilon_{c}^{hom}(r_s, \xi) \quad 2.36$$

where correlation terms vanish.

3 - Within a uniform density escalation for the high-density limit, the correlation energy must be a constant.

On the other hand, exchange term is built based on 4 basic conditions:

1- Within a uniform density and high-density limits:

$$E_{x}^{PBE}[\rho(\vec{r})_{up}, \rho(\vec{r})_{down}] = \int \rho(\vec{r})[\, \epsilon_{x}^{hom}(\rho(\vec{r})) \,.\, F_x(s)]dr^3 \quad 2.37$$

where $\epsilon_{x}^{hom}(\rho(\vec{r})) = \frac{-3e^2 k_F}{4\pi}$ and the so-called enhancement factor $F_x(0) = 1$.

2 – The exact exchange energy obeys the spin equation:

$$E_x^{PBE}\left[\rho(\vec{r})_{up}, \rho(\vec{r})_{down}\right] = \frac{E_x^{PBE}\left[2\rho(\vec{r})_{up}\right] + E_x^{PBE}[\rho(\vec{r})_{down}]}{2}. \quad 2.38$$

3 – For a non-uniform electron gas, the enhancement factor is given by

$F_x(s) \to 1 + \mu s^2$,

where for a liner response $s \to 0$

4 – It is considered the Lieb-Oxford relationship, given by

$$E_x^{PBE}\left[\rho(\vec{r})_{up}, \rho(\vec{r})_{down}\right] \geq E_{xc}^{PBE}\left[\rho(\vec{r})_{up}, \rho(\vec{r})_{down}\right] \geq -1{,}679e^2 \int \rho(\vec{r})^{\frac{3}{4}}\, dr^3 \quad 2.39$$

since spin polarization enhancement factor is:

$$F_x(\xi = 1, s) = 2^{\frac{1}{3}} F_x\left(\frac{s}{2^{\frac{1}{3}}}\right). \quad 2.40$$

So, to describe the non-locality of this GGA approximation, the new enhancement factor F_{xc} was defined over local exchange, given by:

$$E_{xc}^{PBE}\left[\rho(\vec{r})_{up}, \rho(\vec{r})_{down}\right] = \int \rho(\vec{r}) \epsilon_x^{hom} . F_{xc}(r_s, \xi, s) dr^3 \quad 2.41$$

where for a local spin density $F_{xc}(r_s, \xi, 0) \to F_{xc}(r_s, \xi, 0)$. Finally, the GGA-PBE approach not only maintains the characteristics of LSDA approximation, but also takes into account the gradient-corrected non-locality characteristics.

2.4.4 – Modified Becke Johnson (mBJ)

It is well known that LDA and GGA approximations underestimate the band gap energies. In this way, Tran and Blaha [71] presented an efficient method to calculate the band gap energies of solids based on the modification of the Becke Roussel exchange potential[72]. Modified Becke Johnson (mBJ) potential is given by:

$$v_{X,\sigma}^{mBJ} = cv_{X\sigma}^{BR}(\vec{r}) + (3c - 2)\frac{1}{\pi}\sqrt{\frac{5}{12}}\sqrt{\frac{2t_\sigma(\vec{r})}{\rho_\sigma(\vec{r})}} \quad 2.42$$

where the density of charge and kinetic-energy density are, respectively,

$$\rho_\sigma(\vec{r}) = \sum_{i=1}^{N_\sigma} \left|\psi_{i,\sigma}\right|^2 \quad 2.43$$

and

$$t_\sigma(\vec{r}) = \sum_{i=1}^{N_\sigma} \nabla\psi_{i,\sigma}{}^{*} \cdot \nabla\psi_{i,\sigma}.$$

The c parameter is obtained from the electronic density, and the so-called Becke-Russel potential $v_{X\sigma}^{BR}$ is given by,

$$v_{X\sigma}^{BR} = -\frac{1}{b_\sigma(\vec{r})}\left(1 - e^{-X_\sigma(\vec{r})} - \frac{1}{2}X_\sigma(\vec{r})e^{-X_\sigma(\vec{r})}\right) \qquad 2.44$$

which represents the Coulomb potential created by the exchange hole.

2.4.4 – Hybrid functional (HSE06)

Hybrid functionals belong to a class of functionals that allow obtaining more accurate results for the chemical-physical properties of quantum systems compared to traditional GGA functionals. Hybrid functionals allow calculating the exchange-correlation energy $E_{xc}[\rho(\vec{r})]$ from incorporation of the exact exchange Hartree–Fock model. Among them, HSE06 (Heyd, Scuseria, and Ernzerhof) functional [73,74] are a class of functionals with exchange-correlation in calculated as

$$E_{Xc}^{HSE} = aE_X^{HF,SR}(\omega) + (1+a)E_X^{PBE,SR}(\omega) + E_X^{PBE,LR}(\omega) + E_c^{PBE} \qquad 2.45$$

where $E_X^{HF,SR}$ is the short-range HF exchange, $E_X^{PBE,SR}$ and $E_X^{PBE,LR}$ are the short-range and long-range components of the PBE exchange functional obtained from exchange hole of PBE model, and E_c^{PBE} is the PBE correlation energy.

The parameter ω defines the separation of HSE functional partitions the Coulomb potential for exchanges in short-range (SR) and long-range (LR). In HSE06, this value is $\omega_{HF} = \omega_{PBE}$, which is the case where HSE is accurate in the uniform electron gas limit. Moreover, the parameter a is the HF mixing constant, that assumes a default value of a = ¼.

2.5- Pseudopotential

As the number of electrons in a quantum system increases, so does the complexity of the wave function that describes them. Due to this difficulty, molecular and crystalline systems can have their physical and chemical properties described with good precision considering only the

distribution of electrons farther from the nucleus and higher energy, known as valence electrons. Valence electrons are those that effectively form chemical bonds as their wave functions overlap with the wave function of neighboring atoms.

Electrons that are strongly located around the atom are known as core and semi-core electrons. The wave function of these electrons has little overlapping with the wave function of neighboring electrons, making them insensitive to chemical environment change. Thus, the pseudopotential method assumes that the description of the states of the electrons of the core is not determinant for the description of the chemical bond. For this reason, the valence wave function does not need to be well defined in the core region, but in the region where the connection actually occurs, as shown in Figure 2.2.

This approximation reduces the number of particles, simplifying the calculation, and minimizing computational time. The mathematical construction of the pseudopotentials used in this work was based on PAW (Projector Augmented-wave) method. This method was developed by P. E. Blöchl [75] and is widely used to describe quantum system. This method decomposes the all-electron wave functions into the term of soft wave pseudo functions, which maintains the characteristics of the all-electron calculation in addition to considering localized contributions in the core. The PAW method is very effective in describing strongly correlated or magnetic systems, unlike the ultrasoft pseudopotential which is less accurate in magnetic systems [76].

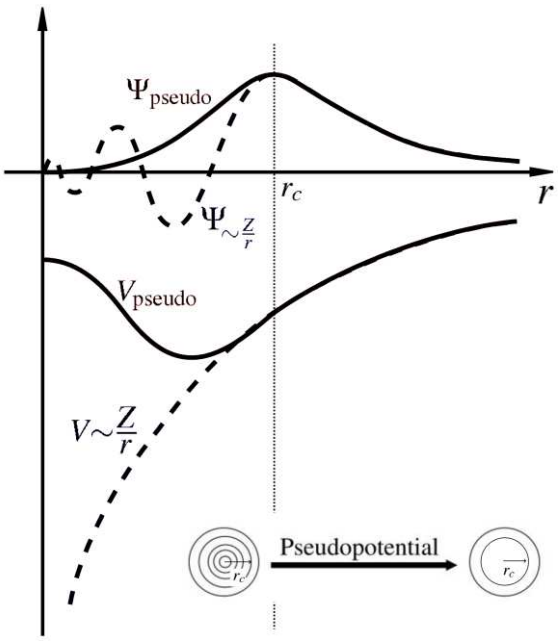

Figure 2.2: Comparison of a wavefunction in the Coulomb potential (real) of the nucleus to the one in the pseudopotential (approximation) [75].

2.6- Brillouin Zone

In solid state physics [77], the study of a periodic quantum system is performed from the use of the Bloch theorem[78]. This theorem states that the solutions to the Schrödinger equation in a periodic potential is given by plane wave functions modulated by a periodic equation, i.e.:

$$\Psi_{nk} = e^{i\vec{k}.\vec{r}} u_{nk}(\vec{r}) \qquad 2.46$$

which can be obtained at the limit of the so-called Brillouin Zone (BZ), which is the Wigner–Seitz unit cell built in reciprocal space. In this context, during the simulation of a given quantum system, the Monkhorst-Pack [79] method is widely used to generate a set of k points in BZ, to then calculate the eigenfunctions. Specifically, BZ to crystalline structures of the space group F-43m (#217) and Fm-3m (#225) are presented in Figure 2.3.

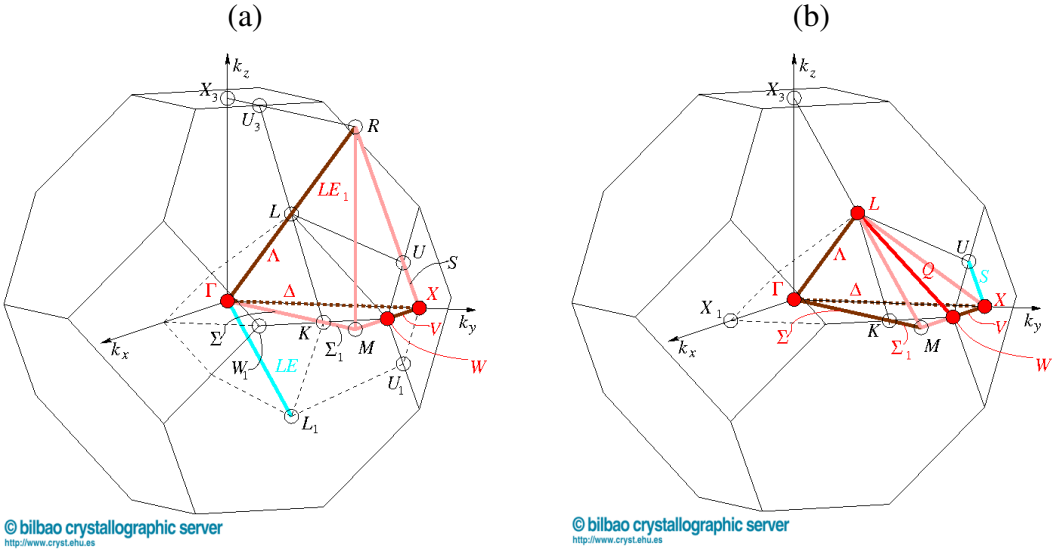

Figure 2.3: Brillouin zone and high symmetry points to crystalline structures of the space groups a) F-43m and b) Fm-3m [80].

2.7- VASP Package

The *Vienna ab-initio simulation package* (VASP) [76,81–84], is a computational package for ab initio calculations based on the DFT, through the solution of Kohn-Sham equations. It stands out for the main features implemented in VASP: i) plane wave base set; ii)

pseudopotential within PAW [75] and *ultrasoft* [83] approaches; iii) Monkhorst-Pack algorithm [79]; iv) Davidson, RMM-DIIS and Conjugate-gradient methods for electronic minimization; and v) LDA, GGA, meta-GGA, DFT+U, hybrid functional, and van der Waals functional available.

2.8- Wannier special functions

The Wannier's functions [85,86], introduced by Gregory Wannier in 1937, are a complete set of orthogonal functions that arise from the unitary transformation from the Bloch functions (Equation 2.46). As seen in Figure 2.4, the Bloch functions are modulated according to the value of k, so Wannier functions are built by superposing Bloch's functions of different k, creating a wave packet centered in each atom.

To construct the wave packet in real space, a very large superposition in k space is required. Thus, the localized Wannier function (WF) is defined as [79]:

$$w_0(\vec{r}) = \frac{V}{(2\pi)^3}\int_{BZ} \Psi_{nk}(\vec{r})\, dk \qquad 2.47$$

where V is the volume of real-space primitive cell and the integral is carried over the BZ.

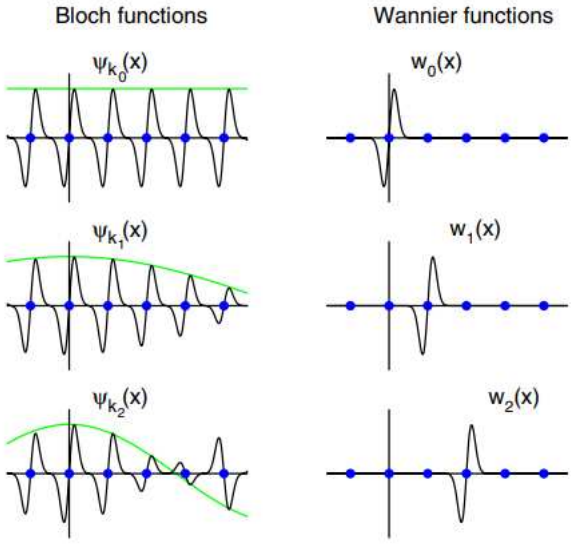

Figure 2.4: Relation between Bloch functions and Wannier functions (WFs). Source: [87].

The functions of Wannier have great application in the study of properties in solids when interpolating the band structures obtained from ab initio calculations. One of the main difficulties in using Wannier functions is the fact that they are not exclusive to a given band,

due to a phase indeterminacy in the Bloch orbitals $u_{nk}(\vec{r})$. Thus, the Wannier functions selected are known as maximally localized Wannier functions (MLWFs). Marzari and Vanderbilt [88], proposed represent the indeterminacy by a free unitary matrix $U_{mn}(k)$ among the occupied Bloch orbitals at every wave vector.

In this work a basis set formed by maximally-localized Wannier functions [88,89] was obtained from WANNIER90 code [90]. In this code, at a given k point, the states are within a predefined window. Thus, a set of $N^{(k)}$ states are obtained performing a unitary transformation in the Bloch state that are within the energy window at each point:

$$u_{nk}^{opt}(\vec{r}) = \sum_{m \in N^k} U_{mn}^{dis(k)} u_{mk}(\vec{r}) \qquad 2.48$$

where $U_{mn}^{dis(k)}$ is a matrix $N^{(k)} \times N$. The $U_{mn}^{dis(k)}$ can be obtained minimizing the gauge invariant in the outer energy window. Thus, with $u_{nk}^{opt}(\vec{r})$ the procedure developed by Marzari and Vanderbilt[88] can be used to define the Wannier functions.

2.9- Boltzwann computational package

Boltzwann [91] is a computational package to determine transport properties based on the semiclassical Boltzmann equations, within the relaxation-time and the rigid band approximations [77,92,93]. Furthermore, this package is integrated with the Wannier90 code where post-processing is performed using the previously obtained Wannier functions. So, the transport distribution function is a tensor defined as:

$$\sum_{ij}(\epsilon) = \frac{1}{V}\sum_{n,k} v_i(n,k) v_j(n,k)\, \tau\,(n,k)\delta\left(\epsilon - E_{n,k}\right) \qquad 2.49$$

which considers the sum over all bands throughout the Brillouin area. $E_{n,k}$ is the energy of the band n at k; $v_i = \frac{1}{\hbar}\frac{\partial E_{n,k}}{\partial k_i}$ is the ith element of the band velocity at (n, k) and $\tau\,(n,k)$ is the relaxation time. From eq. 2.49, Seebeck coefficient (S), electronic conductivity (σ) and thermal conductivity (κ_{el}) can be obtained as:

$$[\sigma]_{ij}(\mu, T) = e^2 \int_{-\infty}^{+\infty} d\epsilon \left(-\frac{\partial f(\epsilon, \mu, T)}{\partial \epsilon}\right) \sum_{ij}(\epsilon), \qquad 2.50$$

$$[\sigma S]_{ij}(\mu, T) = \frac{e}{T}\int_{-\infty}^{+\infty} d\epsilon \left(-\frac{\partial f(\epsilon, \mu, T)}{\partial \epsilon}\right)(\epsilon - \mu) \sum_{ij}(\epsilon) \qquad 2.51$$

and

$$[K]_{ij}(\mu, T) = \frac{1}{T}\int_{-\infty}^{+\infty} d\epsilon \left(-\frac{\partial f(\epsilon, \mu, \tau)}{\partial \epsilon}\right)(\epsilon - \mu)^2 \sum_{ij}(\epsilon). \qquad 2.25$$

For an open system (J = 0), the electronic term of the thermal conductivity is $\kappa_{el} = K - S^2\sigma T$. The lattice contribution to the thermal conductivity (κ_{lat}) is not considered in the calculations.

2.9- Analysis tools for Chemical Bonds

In this section three tools for the analysis of chemical bonds in solids are discussed. All of them are given from the results of the DFT calculations previously carried out, namely: Charge Density, Electron Location Function (ELF) and Bader Charge.

2.9.1 Density of Charges

As mentioned early, the ground state density of charge $\rho_0(\vec{r})$ is an important quantity obtained from a self-consistent ab initio calculation based on DFT. From VASP output files, it is possible extract the density of charges in terms of $\vec{r}$ in *e*/(volume cell). The density can be calculated separately for electrons with spin up and down. Charge density can be graphically analyzed by plotting in a suitable plane or in a region of space, considering a certain isosurface. From these maps, the spatial distribution of charges is obtained, being useful in the analysis of chemical bonds.

2.9.2 Electron Localization Function (ELF)

Electron Localization Function (ELF) is a tool that maps the probability of finding a spin- σ electron in the vicinity of another reference electron with the same spin-σ. Becke and Edgecombe [94] define ELF function considering the probability of find an electron named **2** of spin-σ in position $\vec{r}_2$ in the vicinity of reference electron named **1** in $\vec{r}_1$ with the same spin-σ:

$$\rho^{\sigma,\sigma}(\vec{r}_1, \vec{r}_2) = \frac{\rho_2^{\sigma,\sigma}(\vec{r}_1, \vec{r}_2)}{\rho_\sigma(\vec{r}_1)} \qquad 2.53$$

where $\rho_\sigma(\vec{r}_1)$ represents the density of probability of electron **1** and $\rho_2^{\sigma,\sigma}(\vec{r}_1, \vec{r}_2)$ Hartree-Fock probability of finding two particles with a same spin σ simultaneously at positions $\vec{r}_1$ and $\vec{r}_2$, that is,

$$\rho_2^{\sigma,\sigma}(\vec{r}_1,\vec{r}_2) = \rho_\sigma(\vec{r}_1)\rho_\sigma(\vec{r}_2) - |\rho_1^\sigma(\vec{r}_1,\vec{r}_2)|^2 \quad 2.54$$

considering $\rho_1(\vec{r}_1)$ as a σ-spin one-body density matrix of the Hartree-Fock determinant:

$$\rho_1^\sigma(\vec{r}_1,\vec{r}_2) = \sum_i^\sigma \psi_i^*(\vec{r}_1)\psi_i(\vec{r}_2) \quad 2.55$$

with summation restricted to orbitals of σ spin only.

Moreover, from Taylor expansion of the spherically averaged conditional, the pair probability is given by:

$$\rho^{\sigma,\sigma}(\vec{s},\vec{r}) = \frac{1}{3}\left[\tau_\sigma - \frac{1}{4}\frac{(\nabla\rho_\sigma)^2}{\rho_\sigma}\right]|\vec{s}|^2 + \cdots \quad 2.56$$

where τ_σ positive-definite kinetic energy density, and the measure of electron localization is given by,

$$D_\sigma = \tau_\sigma - \frac{1}{4}\frac{(\nabla\rho_\sigma)^2}{\rho_\sigma}. \quad 2.57$$

Written another way, for an eigenfunction given by a Hartree-Fock or Kohn Sham orbitals θ_i^{KS} [95]:

$$D_\sigma = \frac{1}{2}\sum_i |\nabla\theta_i^{KS}|^2 - \frac{1}{8}\frac{|\nabla\rho_\sigma|^2}{\rho_\sigma}. \quad 2.57$$

There is an inverse relationship between localizability and probability. The lower the probability of finding electron 2 in a region of space, which implies a lower value of D_σ, the more localized is the reference electron **1** is in that location.

Since the function D_σ can take on any value, the ELF function is then defined as being:

$$ELF = \frac{1}{1 + \left(\frac{D_\sigma}{D_\sigma^0}\right)^2}, \quad 2.59$$

$$0 \leq ELF \leq 1.$$

In which D_σ^0 corresponds to a uniform electron gas with spin density equal to the local value of $\rho_\sigma(\vec{r})$:

$$D_\sigma^0 = \frac{3}{10}(3\pi^2)^{\frac{5}{3}}\rho_\sigma^{\frac{5}{3}}. \quad 2.60$$

The upper limit ELF = 1 corresponding to perfect localization ($D_\sigma \to 0$). ELF = 1/2 corresponding to electron gas-like pair probability ($D_\sigma = D_\sigma^0$) and ELF = 0 corresponds to the

zero probability of finding the reference electron ($D_\sigma \rightarrow \infty$). Also, the function ELF can be analyzed by mapping it on a given plane or by plotting it in space to some isosurface value.

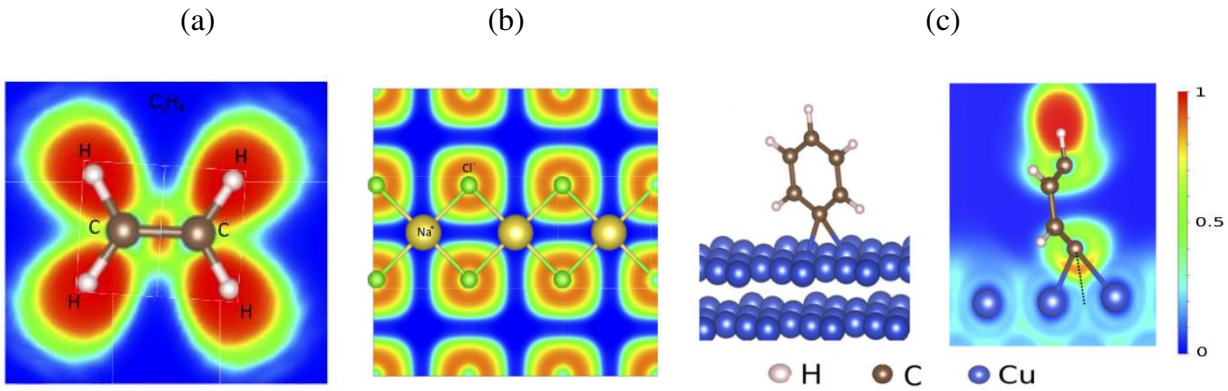

Figure 2.5: 2D plot ELF to a) molecule ethene b) NaCl salt c) along the plane containing the chemical bond between C and a Cu–Cu metallic bond. Source: [96].

Two concepts that usually appear in this analysis are the attractor and basin. The attractor is the region where the ELF function presents its maximum locations, while the points around the attractor that also have high function values form its basin. For instance, Figure 2.5 (a) shows a non-polar covalent bonds C-C, an attractor centered on the bond axis is usually observed. For a polar-covalent bond, the attractor tends to move toward the more electronegative atom. As shown in Figure 2.5(b), for ionic bonds of the NaCl type, spherical surfaces (basin) appear around atoms ion (Cl^-), while Na^+ not present ELF. Furthermore, Figure 2.5 (c) shows that for metallic bonds of the Cu-Cu type, ELF presents a small extension; while for Cu-C type bonds, with polar covalent character, the ELF function is greater in the vicinity of C.

2.9.3 Bader Charge

Bader charges are calculated from integrals on so-called Bader volumes, through the theory developed by R. Bader [97] for atoms and molecules. Bader's volumes come from

partitioning the space of a system of many atoms into volumes that have only a maximum charge density. These volumes are separated by surfaces on which the charge density is a minimum normal to the surface, satisfying the condition $\nabla\vec{\rho}.\vec{n} = 0$**.** Usually, each atom in the molecule has a maximum charge density so that each atom will possess its Bader volume [98]. The Bader charge is then defined as:

$$q = Z_{VEC} - \text{Bader population} \qquad 2.61$$

where Z_{VEC} is the number of valence electrons of an atom and the Bader population arises from the integral that provides the number of electrons of Bader volume of that atom. The Bader Charge was calculated using Henkelman's code [99] implemented in program VASP.

2.10 Effective Mass

The calculation of the effective masses was based on the free electron approximation (FEA) in rigid band condition. For a free electron, energy is a parabolic function of wave vector κ:

$$E = \frac{p^2}{2m} = \frac{\hbar^2 k^2}{2m} \qquad 2.62$$

where m is the electron mass, $\vec{p}$ the linear momentum and $\hbar = 6.58\times10^{-16}\, eV$. So, the variation of energy in reason of k can be written as:

$$\frac{1}{\hbar^2}\frac{d^2E}{dk^2} = \frac{1}{m}. \qquad 2.63$$

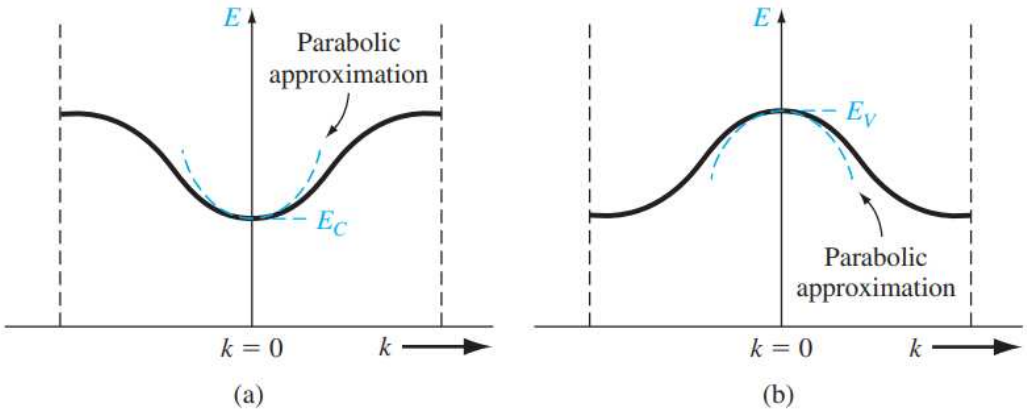

Figure 2.6: Representation of a) VBT parabolic approximation, b) VBB parabolic approximation. Source: [87,100].

In FEA the band structure has a parabolic characteristic in the vicinity of a certain k point, as seen in Figure 2.6 that shows the Valence Band Top (VBT) and Conduction Band Bottom (CBB) region. A free electron does not experience the influence of any potential, then the mass in Equation 2.63 will be equal to the rest mass of the electron m_0^*. On the other hand, an electron in certain crystalline system suffers the influence of effective potentials, then the mass in Equation 2.63 is different of m_0^*, i.e., the effective mass m^*.

Considering E_l the energy of the free electron and E the energy of the electron in a given crystalline system, the following expression can be written:

$$E - E_l = Ck^2 \qquad 2.64$$

where C is a constant, where the second derivative with respect to k is:

$$\frac{d^2E}{dk^2} = 2C\,. \qquad 2.65$$

After comparing equations 2.63 and 2.65:

$$m^* = \frac{1}{2C}. \qquad 2.66$$

This relationship allows us to directly calculate the effective mass from a parabolic adjustment performed in a given region in the band structure, where the parabolic curvature C is an important parameter. A more "closed" band will then have a higher value of C, which indicates a lower value of m*. This bands are known as Light Electron band in conduction band and Light Hole band in valence band (Figure 2.7). While more "opened" parabolas have a lower value of C and consequently a higher value of m* and are known as Heavy Electron/Hole Bands.

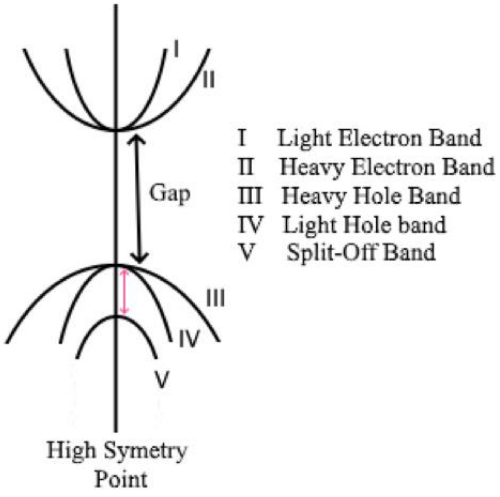

Figure 2.7: Classification of the bands according to the effective mass presented at points of high symmetry.

As already mentioned, the term hole refers to the Valence Band Top (VBT), since in this case the approximation is made by means of a convex parabola (negative constant C), implying a negative mass. The physical interpretation is that this mass refers to the electrons that could be transferred to the conduction band, leaving these levels unoccupied, then called holes.

High values of effective mass have a direct relation with increase the Seebeck coefficient, but decrease electronic mobility and consequently the electrical conductivity [101,102]. The analysis of effective mass for Seebeck coefficient is make with basis of density of states effective mass (m^*_{DOS}) that take in account different crystallographic directions and the degeneracy factor N_d given by relation [103]:

$$m^*_{DOS} = (m^*_1\, m^*_2 m^*_3)^{\frac{1}{3}}\, N_d^{\frac{2}{3}}. \qquad 2.67$$

That m^*_1, m^*_2 and m^*_3 are effective mass take of principal directions of the equal energy ellipsoids. The m^*_{DOS} also can be calculated directly with the equation of density of states within free electron approximation (FEA):

$$D(E) = \frac{1}{2\pi^2}\left(\frac{2m^*_{DOS}}{\hbar^2}\right)^{3/2} E^{1/2}. \qquad 3.14 \quad 2.68$$

This approximation is applied next to the fermi level.

2.11 Spin–orbit coupling (SOC)

Spin-orbit coupling (SOC) is a relativistic effect that is described by Dirac's relativistic analysis of the electron [64]. Usually, SOC has its importance increased as the atomic number increases and causes the loss of degeneracies in the band structures, and leading to a band split-off, as shown in Figure 2.7 [77,104]. The SOC effect is very important for magnetism and spintronics, in which it drives magnetic anisotropy, spin relaxation, magnetic damping, anisotropic magnetoresistance and Hall effect [105].

2.12 Cohesive Energy (E_c)

The cohesive energy of a solid refers to the energy needed to separate the atoms of crystal structure and put them isolated [77,106] . In an ideally ionic crystal, the cohesive energy can be calculated summing up the electrostatic of the arrange the atoms. When metallic and

covalent bonds are involved, the energy of cohesive E_c can be calculated from first principles calculation using the total energy (E_T) of crystal and the isolated atoms belonging to the system, i.e:

$$E_c = E_T(\text{crystal}) - \sum E_T(\text{atoms}). \qquad 3.14 \quad 2.69$$

The cohesive energy is a parameter for measure the stability of a crystal lattice and depend of type, localization, quantity and chemical bonds of atoms in the structure.

3 – METHODOLOGY

The work was developed through first principles calculations within the Density Functional Theory (DFT) [66,68]. For the calculations of the electronic structure, spin polarization was considered, using the Projector Augmented-Wave (PAW) method [75], within GGA-PBE [70], GGA-mBJ HSE06 [73,74] functional as implemented in the VASP. The electronic distribution for each pseudopotential is: Co ($3d^8 4s^1$), Sn ($5s^2 4d^{10} 5p^2$), V($3p^6 3d^4 4s^1$), Nb($4p^6 5s^2 4d^3$) and (Ta ($5p^6 6s^2 5d^3$). The calculations were performed with a 350 eV energy cutoff in the plane-waves expansions. Each structure was fully relaxed, until the residual forces in the ions were at least less than 1 meV/Å. Also, the effective mass was calculated according to equation 2.66, within parabolic approximation. A parabolic fitting was performed, considering the quadratic term (C) of polynomials of degree 2, 3 and 4. The parabolic approximation was considered successful when the coefficient C of the 3 analyzed curves had a fluctuation of less than 5%. For all systems, a 9×9×9 k-points Monkhorst–Pack mesh centered on the gamma point was used for integration in the BZ, as shown in the convergence test highlighted in Figure 3.1.

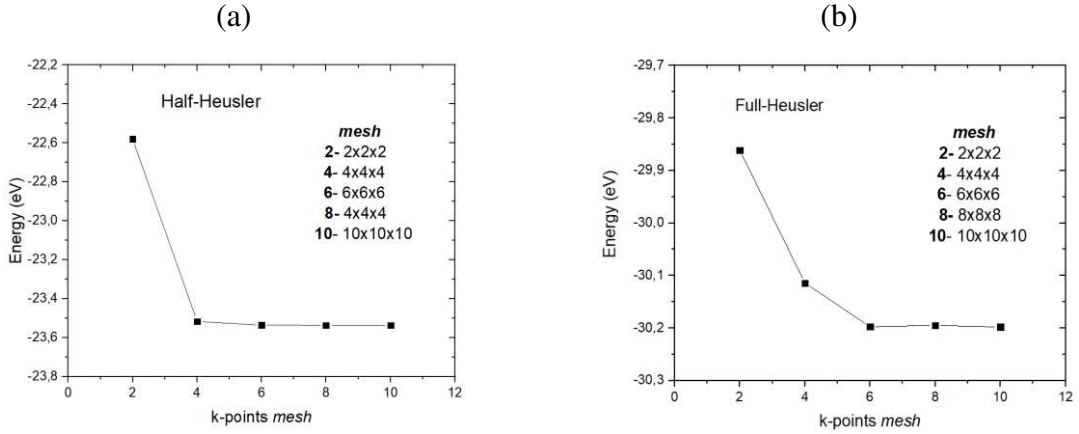

Figure 3.1: Equilibrium structures of (a) HH and (b) FH alloys from GGA-PBE calculations.

The thermoelectric quantities, S, σ and κ_{el} were calculated by solving the Boltzmann's transport equations in the relaxation time approximation (τ) as implemented in the Boltzwann code [91]). The MLWF's was obtained from WANNIER90 code [90] and used to interpolate the band structures obtained previously from ab initio calculation. A 40×40×40 grid of k-points was considered to calculated the thermoelectric quantities.

4 – RESULT AND DISCUSSION

This section presents the theoretical results of physicochemical properties of Co-VB-Sn (VB = V, Nb, Ta) Heusler alloys. The results were organized into subsections called: 4.1 Structures; 4.2 Electronic and Magnetic Properties; 4.3 Effective Mass and SOC; 4.4 Chemical Bonds; and 4.5 Thermoelectric Properties. The results were compared to the available experimental data.

4.1 Structures

Half-Heusler alloys (HH) have a general formula XYZ, spatial group F-43m (SG #216), Strukturbericht designation C_{1b} and Pearson symbol cF12. As shown in Figure 4.1 (a), HH structure has three sites defined through the Wyckoff positions 4a (0.0.0), 4b (0.5, 0.5, 0.5) and 4c (0.25, 0.25, 0.25). When the 8c position (0.75, 0.75, 0.75) is takes into account, the Full-Heusler alloy (FH) and general formula XY_2Z is formed, as depicted in Figure 3.1 (b). The FH has space group Fm-3m (#225), Strukturbericht designation L_{21} and Pearson symbol cF16 [107,108].

HH alloys are usually described as being formed by the interpenetration of a NaCl-type structure (Figure 4.1 (c)) with a SnZ-type structure (Figure 4.1 (d)). As shown in Figure 4.1 (e) - (f), the chemical bond between the positions 4c-4a and 4c-4b leads to a tetrahedron inversion, although the structures remain the same [109]. Figure 4.1 (g) shows a third possible bond of eightfold coordination, since there are two tetrahedrons around the 4c position. This explains the reason of the exchange of atoms of positions 4a and 4b leads to equivalent structures. Thus, the description of chemical bonds in HH can go beyond the simplification made when considering this alloy as being generated from combination of NaCl-type and ZnSn-type structures [110]. In addition, Figure 4.1 (h-j) depicts a FH structure, where a more complicated bonding arrangement is observed, although this structure may have the same type of bonds as the HH.

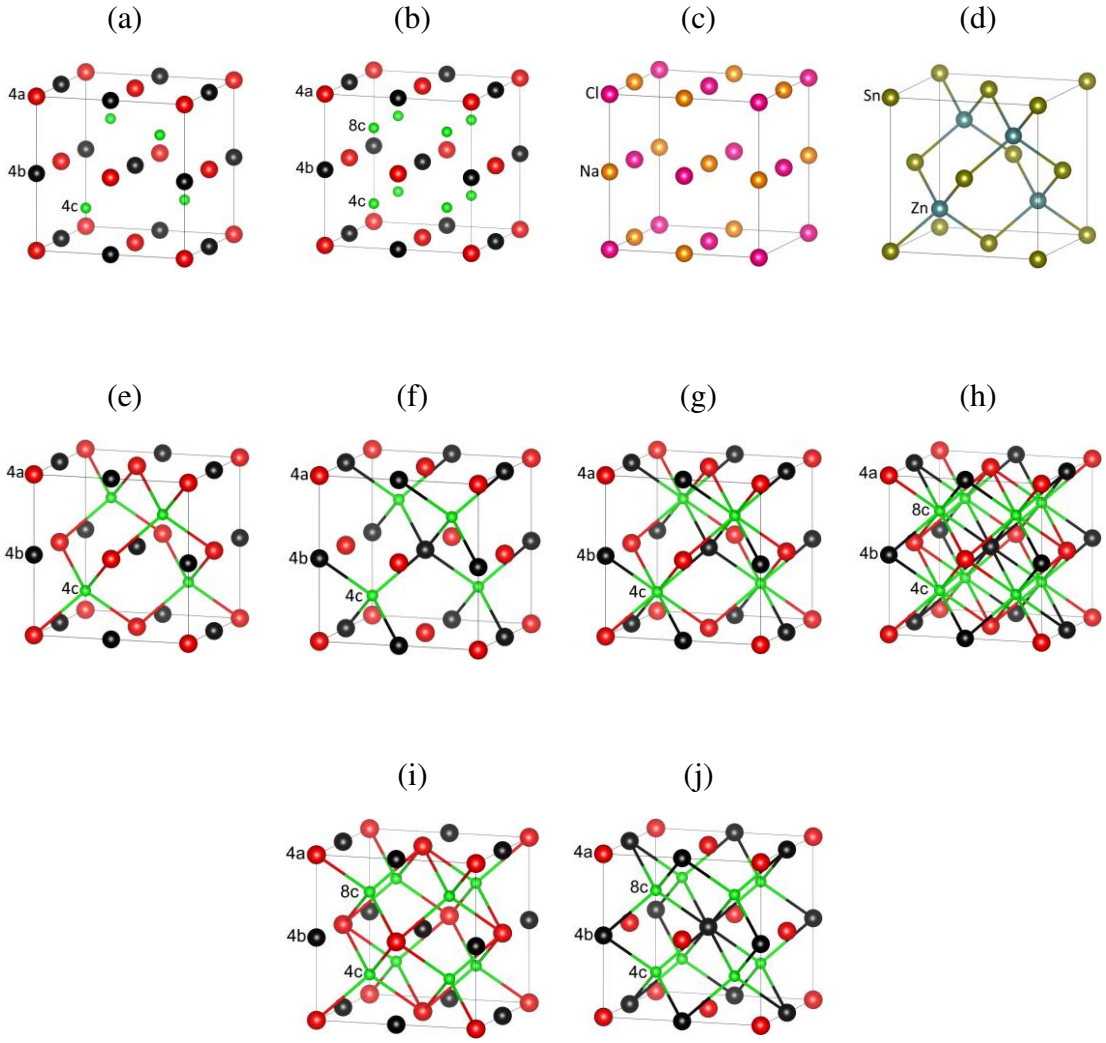

Figure 4.1: Crystal structures: (a) Half-Heusler, (b) Full-Heusler, (c) NaCl-type and (d) ZnSn-type. In figures (e-f) are represented three possible chemical bonds of atom in 4c. The structures Full-Heusler (h-j) may have the same type of bonds as the Half-Heusler.

Ternary Heusler alloys have well-defined sites for each element, resulting in 6 possible structures (permutation P(3,3)) as shown in Table 4.1. In agreement with the results showed in next, there is only three distinct structures from the six possible [111]. This distinction occurs only in reason of occupation of the 4c/8c site. So, the structures I and II, II and IV, V and VI are equivalent, and will be treated in this work as A, B and C, respectively.

Table 4.1. Wyckoff positions for the atoms Co, Sn and Ta for each HH and FH structure. The 8c position is occupied only in FH case.

Structures		Wyckoff Positions		
		Co	**Sn**	**Group VB[a]**
A	I	4c/8c	4a	4b
	II	4c/8c	4b	4a
B	III	4a	4c/8c	4b
	IV	4b	4c/8c	4a
C	V	4a	4b	4c/8c
	VI	4b	4a	4c/8c

[a]Group VB = V, Nb and Ta.

4.1.1 Vanadium alloys

Based on GGA-PBE calculations, the lattice parameters of vanadium structures A, B and C were optimized for HH and FH alloys. As previously mentioned, among the six possible structures, the energies curves showed that sets of structures I-II, III-IV and V-VI are degenerated. The Wyckoff positions for each structure are shown in Table 4.1. Position 8c is occupied only for FH cases. As shown in Figure 4.2 (a), the occupation of site 4c by Co leads to more stable structure in case of HH-A.

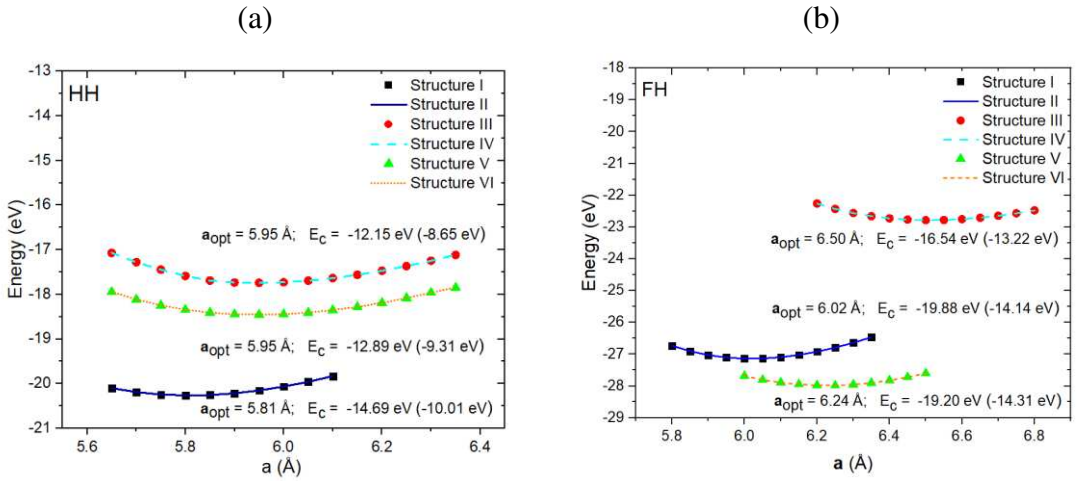

Figure 4.2: Total energy versus lattice parameter of several (a) HH and (b) FH vanadium structures for obtained from GGA-PBE calculations. The cohesive energy was calculated from Equation 2.69 within GGA-PBE (HSE06) approximation.

Table 4.2 presents the optimized lattice parameter equal to 5.81 Å to HH-A CoVSn alloy, in good agreement with previous theoretical works [112–115]. It was observed that the lattice parameter did not change when SOC effect is taken into account. Moreover, structures with the same atomic species in sites 4c/8c are energetically equivalent, for instance, I and II; III and IV; V and VI, named structures A, B and C, respectively. HH-B and HH-C have the same lattice parameter 5.95 Å, although the latter is slightly more stable. This lattice parameter is very close to that reported experimentally [116], although the authors did not determine what the crystal structure of the studied sample is. Finally, the cohesive energy (E_C) was calculated from the GGA-PBE and HSE06 functionals (showed in parentheses), as shown in Figure 4.2 (a), corroborating that HH-A is the most stable structure among others.

Table 4.2 - Lattice parameter of Group VB alloys.

	This Work	**Theoretical work**	**Experimental**
V alloys			
HH-A (Å)	5.81	5.79 [112], 5.81 [113], 5.83 [114,115], 5.70 [115], 5.71 [117], 5.73 [118]	5.98 [aa] [116]
FH-A (Å)	6.02	6.03 [119], 6.02 [120]	**-**
Nb alloys			
HH-A (Å)	5.97	5.90 [112], 5.91 [121],	5.95 [53,54,60,62,122]
FH-A (Å)	6.17	6.18 [123]	6.15 [124–126]
Ta alloys			
HH-A (Å)	5.96	5.97 [61], 5.89 [118], 5.96 [127], 5.95 [128]	5.94[61] , 5.95[62]
FH-A (Å)	6.15	6.16 [127]	-

[aa] Structure not specified.

The lattice parameter optimizations for Vanadium FH alloys are presented in Figure 4.2 (b). For FH-A, a = 6.02 Å in good agreement with literature [119,120]. Conversely, FH-B (6.24 Å) and FH-C (6.50 Å) have larger lattice parameters. As presented in Table 4.3, Sn has simultaneously high atomic radius and greater electronegativity compared to other atoms. In fact, the occupation of the 8c site by a Sn atom causes the FH-C structure to have a higher lattice parameter, while the FH-B structure has an intermediary value.

Table 4.3 – Atomic radius and Pauling electronegativity [129].

	Co	Sn	V	Nb	Ta
Atomic Radius (Å)	1.35	1.45	1.35	1.45	1.45
Pauling electronegativity	1.88	1.96	1.63	1.60	1.50

The cohesive energies (EC) were calculated for Vanadium FH structures. It was obtained from GGA-PBE approximation that Ec(A) < Ec(C) < Ec(B), while Ec(C) < Ec(A) < Ec(B) from hybrid HSE06 calculations. Considering that hybrid approximation provides a more accurate electronic description, it can be seen that FH-C is the most stable structure among others.

4.1.2 Niobium alloys

The optimized lattice parameter for HH and FH niobium alloys are presented in Figure 4.3. Similar to the alloys with vanadium, the structure HH-A, where Co is located in position 4c, is the most stable with optimized parameter 5.97 Å and E_c = -16.48 eV (-13.25 eV). As shown in Table 4.2, a good agreement with previous experimental works [53,54,60,62,122] is observed. On the other hand, HH-B and HH-C structures have greater lattice parameters and cohesive energies (less negative), that is, lower stability.

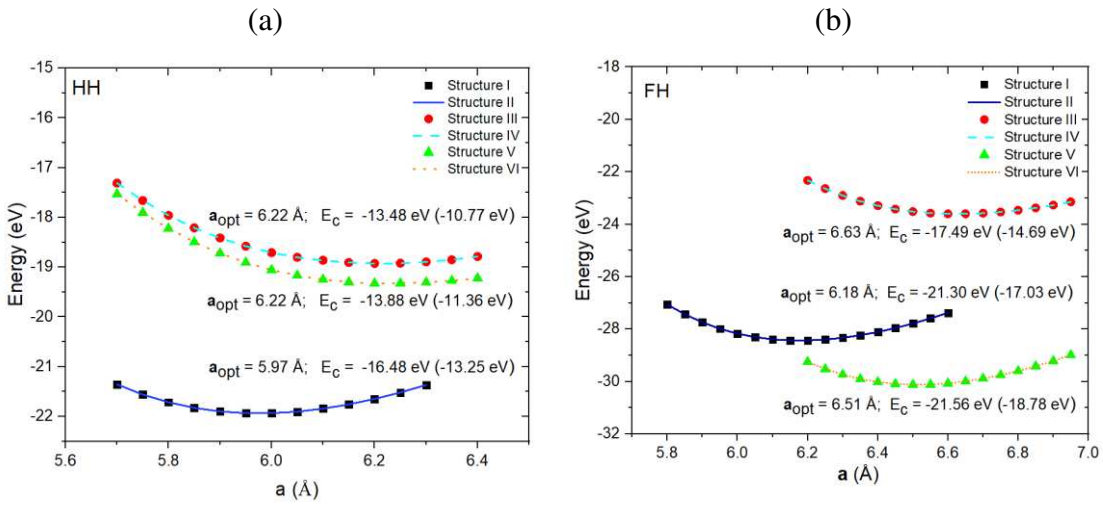

Figure 4.3: Total energy versus lattice parameter of several (a) HH and (b) FH niobium structures for obtained from GGA-PBE calculations. The cohesive energy was calculated from Equation 2.69 within GGA-PBE (HSE06) approximation.

The lattice parameter optimizations for Niobium FH alloys are presented in Figure 4.3 (b). For FH-A, a = 6.18 Å in good agreement with theorical and experimental results reported in literature [123-126]. Conversely, FH-B (6.63 Å) and FH-C (6.51 Å) have larger lattice parameters. The cohesive energies were calculated from GGA-PBE and HSE06 functionals, where FH-C < FH-A < FH-B. So, indicating that FH-C structure is the most stable among them.

4.1.3 Tantalum alloys

The optimized lattice parameter for Tantalum structures Ta alloys is presented in Figure 4.4. The most stable structure HH-A has an optimized parameter of 5.96 Å, in agreement with theorical [61,127,128] and experimental [61,62] results. The HH-B and HH-C structures presented greater lattice parameter. Finally, the cohesive energy (E_C) was calculated from the GGA-PBE and HSE06 functionals, as shown in Figure 3.4 (a), confirming that HH-A is the most stable structure among others.

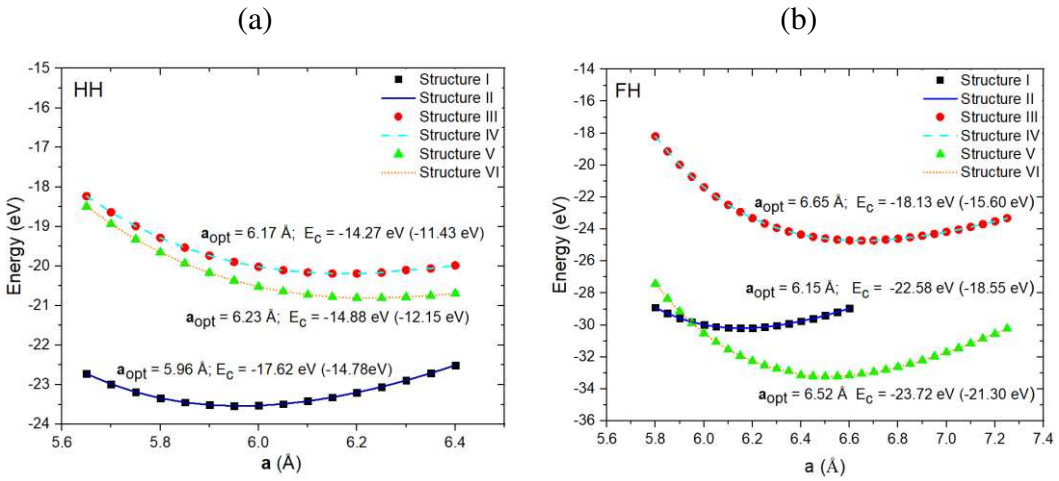

Figure 4.4: Total energy versus lattice parameter of several (a) HH and (b) FH tantalum structures for obtained from GGA-PBE calculations. The cohesive energy was calculated from Equation 2.69 within GGA-PBE (HSE06) approximation.

Figure 4.4 (b) shows that the optimized lattice parameter of for FH-A is 6.15 Å, which is very close to the 6.16 Å as previously reported by R. Dutt and et al. [127]. On the other hand, FH-B (6.65 Å) and FH-C (6.52 Å) have larger lattice parameters. The calculated cohesive energy shows that FH-C is the most stable of the structures.

4.2 Electronic and Magnetic properties

Several physicochemical properties of Heusler alloys have a strong dependence of valence electron count (VEC) [130]. As verified, the Slater-Pauling rule predict the total magnetic moment (M) from the equations:

$$\text{HH: } M = |Z_{VEC} - 18| \quad 4.1$$

$$\text{FH: } M = |Z_{VEC} - 24| \quad 4.2$$

where Z_{VEC} is the number of valence electrons of respectively atom. For the atoms used in this work: $Z_{VEC}(Co) = 9, Z_{VEC}(V, Nb, Ta) = 5$ and $Z_{VEC}(Sn) = 4$. Considering the unitary cell, HH alloys have 3 atoms (XYZ) and FH have 4 atoms (X_2YZ). According to Equation 4.1, HH alloys must have a total magnetization equal to zero, while equation 4.2 predicts a total magnetization of $3\mu_B$, $2\mu_B$ and $1\mu_B$ for the FH-A, FH-B, and FH-C structures, respectively.

4.2.1 Vanadium alloys

Table 4.4 shows the total magnetic moment and magnetic moment per atom for HH and FH structures. From HSE06 calculations a good agreement with Slater-Pauling rule was observed for HH-A, HH-C, FH-A and FH-B structures, where only HH-A has a diamagnetic characteristic. In the FH-C structure, an antiferromagnetic (ferromagnetic) interaction between vanadium atoms and a total magnetic moment of 2.0 μ_B/cell (4.4 μ_B/cell) were obtained from HSE06 (GGA-PBE) calculations. Moreover, a contribution of the interstitial region of the crystal (Δ_m) to the total magnetic moment is observed for some structures. The magnetic moment is calculated from spheres around the atoms, where Δ_m are the contributions to the total magnetic moment from the interstitial region between these spheres.

Considering that: i) the atoms involved in the composition of the HH and FH structures have strongly correlated electrons; ii) the GGA-PBE approximation fails in the electronic description of these systems, including the positioning of the Kohn-Shan levels; iii) the hybrid approximation provides a more precise electronic description of strongly correlated systems, so in this work the results obtained from the HSE06 functional were admitted.

Figure 4.5 shows the total (TDOS) and partial (PDOS) density of states for HH structures obtained from GGA-PBE and HSE06 calculations. A semiconductor character is observed for HH-A structure. As summarized in Table 4.5, a band gap of 0.64 eV was obtained from GGA-PBE calculation, which is in good agreement with other theoretical work

[112,113,118]. Conversely, a band gap of 1.33 eV was calculated from HSE06 functional, which is almost double (0.85 eV) of the previously obtained from mBJ calculation [114]. Figures 4.5 (a-d) shows that V(d) and Co(d) orbitals are prominent around the Fermi level (E_f), while Sn(p) orbitals have a smaller contribution in the valence band region. Furthermore, a splitting of the t_{2g} and e_g levels is observed for the d-levels of V and Co atoms according to Crystal Field Theory [131]. Co(e_g) and V(t_{2g}) levels are mainly present in VCB, while Co(t_{2g}) and V(t_{2g}) are present CBB.

Table 4.4 - Local (m) and total (M) magnetic moments of the structures HH and FH for (Co-V-Sn) alloys from HSE06 (GGA-PBE) calculation. Δ_m represents the contribution of interstitial region of the crystal. Values of M in bold are in accordance with the Slater-Pauling rule.

Alloy		**m** μ_B/atom			**Δ_m** μ_B/cell	**|M|** μ_B/cell
		Co	**Sn**	**V**		
HH	A	0 (0)	0 (0)	0 (0)	0 (0)	**0 (0)**
	B	1.8 (0.1)	0 (0)	-2.4 (0)	0 (0)	0.6 (0.1)
	C	2.2 (0.3)	0 (0)	-2.1 (-0.2)	-0.1(0)	0 (0.1)
FH	A	1.4/1.4 (1.0/1.0)	0 (0)	0.6 (1.0)	-0.4 (0)	**3.0 (3.0)**
	B	1.7 (-0.5)	0/0 (0/0)	-2.8 (2.0)	-0.8 (0.4)	1.9 (1.9)
	C	2.0 (1.0)	0 (0)	-2.4/2.4 (1.5/1.5)	0 (0.4)	2.0 (4.4)

As shown in Figures 4.5 (e-h), a conductor character is observed for the HH-B structure in both approximations, although there are divergent results in the partial densities of states. Figures 4.5 (h) shows that around E_F, Co(t_{2g}) and Ta(t_{2g}) projections are present principally for the spin down channel, which is not observed from GGA-PBE calculation in Figure 4.5 (f). The HH-C structure also showed a conductor character, as shown in Figures 4.5 (i-l). A similar trend for PDOS is observed, where compared with HH-B structure.

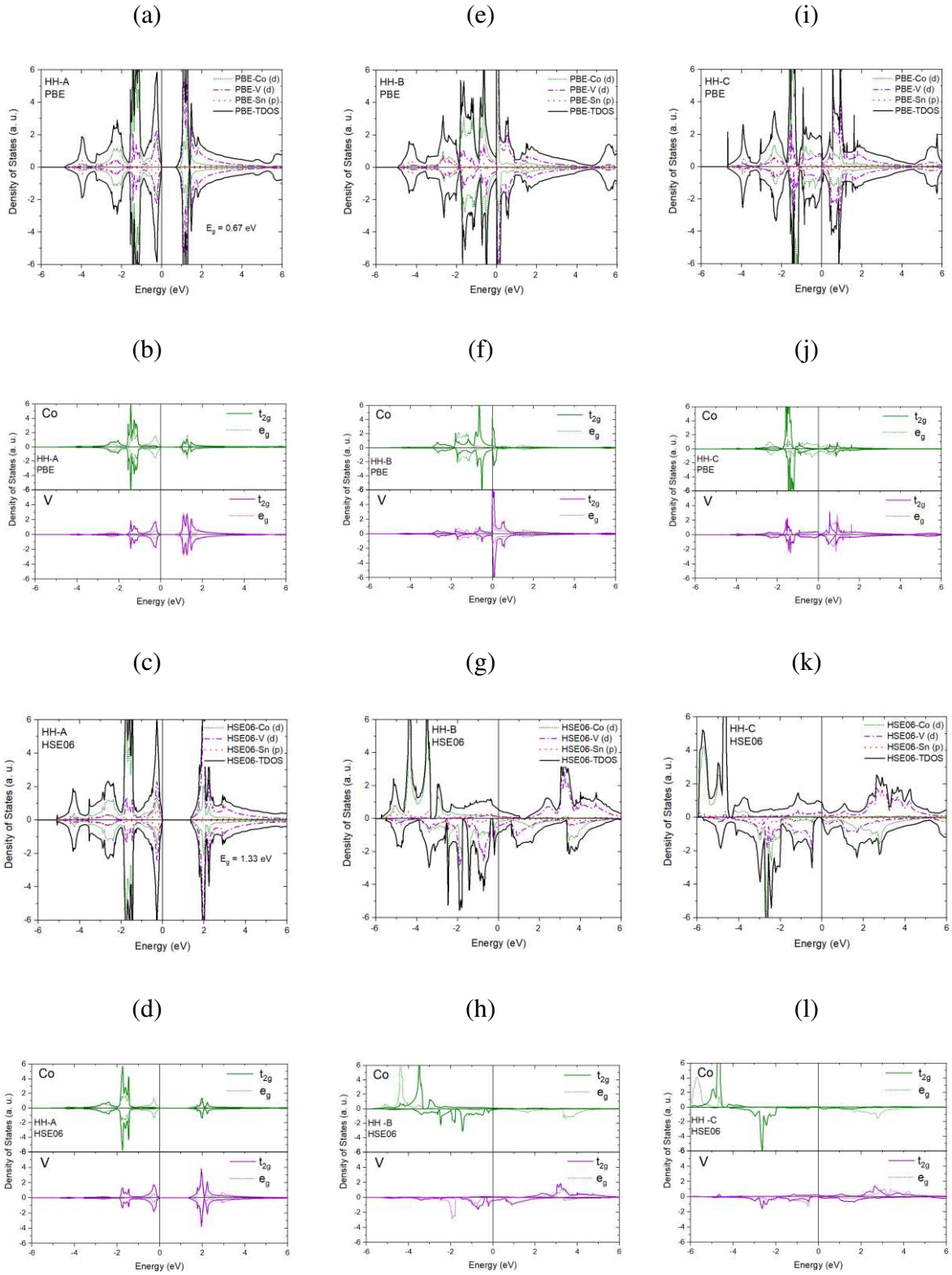

Figure 4.5: TDOS and PDOS for (a-b) HH-A, (c-d) HH-B and (e-f) HH-C vanadium structures, obtained from PBE calculations; (g-h) HH-A, (i-j) HH-B and (k-l) HH-C vanadium structures, obtained from HSE06 calculations.

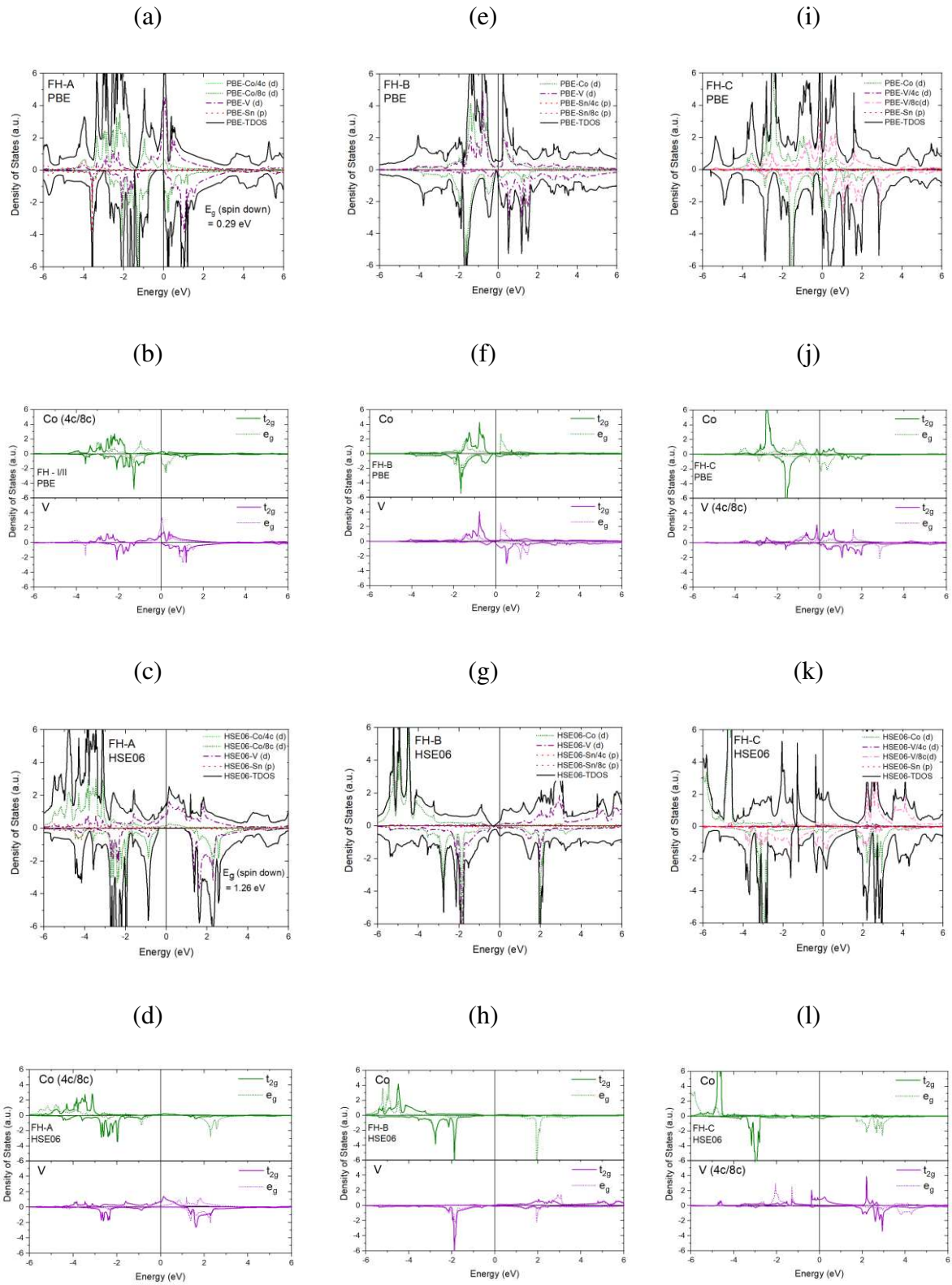

Figure 4.6: TDOS and PDOS for (a-b) FH-A, (c-d) FH-B and (e-f) FH-C vanadium structures, obtained from PBE calculations; (g-h) FH-A, (i-j) FH-B and (k-l) FH-C vanadium structures, obtained from HSE06 calculations.

TDOS and PDOS for FH alloys were obtained from GGA-PBE and HSE06 calculations, as depicted in Figure 4.6. From GGA-PBE calculation, FH-A structure presents a half-metal (HM) behavior with an underestimated band gap of 0.29 eV compared to other theoretical results [120,132]. In contrast, a band gap of 1.26 eV in spin down channel was found in HSE06 calculation. Unfortunately, no experimental results were found in the literature. It is important to mention that the HM character of the material allows it to have a complete spin polarization, thus a fully spin-polarized current for spintronic applications [133,134]. As observed in Figure 4.6 (c), Co atoms that occupy the positions 4c and 8c have the same density of states. According to Figures 4.6 (d) V(t_{2g}) have an important contribution to conductor character in the spin up channel.

Table 4.5 – Band gap of VB Group alloys.

	This Work	**Theoretical work**	**Experimental**
V alloys			
HH-A (Å)	0.64[a] 1.33[b]	0.65 [a] [112], 0.63 [a], 0.89 [c] [113], 0.85 [c] [114], 0.75 [d] [117], 0.66 [a] [118]	-
FH-A (Å)	0.29[a] 1.26[b]	0.56 [a] (HM) [120], 0.53 [a] (HM) [132]	-
Nb alloys			
HH-A (Å)	0.97 [a] 1.50 [b]	1.0 [a], 1.3 [b] [54], 1.0 [a] [55], 0.92 [a] [62], 1.0 [a] [122], 0.99 [a] [135]	0.87 [62], 1.00 [118]
FH-A (Å)	0.86 [b] (HM)	Metallic [a] [123,136]	-
Ta alloys			
HH-A (Å)	1.04[a] 1.18[b]	1.3 [b] [61], 1.04 [a] [62], 1.06 [a] [118], 1.04 [a] [127], 1.09 [a] [128], 1.11 [a], 1.13 [c] [137]	1.60-1.80 [61], 0.57 [62]
FH-A (Å)	1.36[b] (HM)	Metallic [c] [138]	-

[aa] Structure not specified, [a] GGA-PBE, [b] HSE06, [c] mBJ, [d] VWN-LDA, [e] LSDA.

As shown in Figures (e-l), FH-B and FH-C structures are conductors, although spin-gapless [139] character was obtained for the FH-B structure from GGA-PBE calculation, but

not to the HSE06. Even so, it is important highlight that this character can be an advantage in several areas, for instance, in applications of spintronic devices [140]. In addition, both FH and HH present discrepancy between the GGA-PBE and HSE06 results, both in relation to the description of the DOS and magnetization. As discussed above, this is related to the difficulty of analysis from the GGA-PBE functional, where it fails to accurately describe strongly correlated systems, generally involving d and f orbitals [141].

4.2.2 Niobium alloys

Table 4.6 shows the partial and total magnetization for Nb alloys. From HSE06 calculation, HH-A presented a diamagnetic behavior, while FH-A presented a M = 3 μ_B/cell in agreement with Slater-Pauling rule. The total magnetic moment of FH-A comes from the magnetization of 1.6 μ_B/Co, in agreement with previous theorical work [124]. Unlike, all of other structures are in disagreement with Slater-Pauling rule.

Table 4.6 - Local (m) and total (M) magnetic moments of the structures HH and FH for (Co-Nb-Sn) alloys from HSE06 (GGA-PBE) calculation. Magnetic moments calculated with GGA-PBE for comparation. Δ_m represents the contribution of interstitial region of the crystal. Values of M in bold are in accordance with the Slater-Pauling rule.

Alloy		**m** μ_B/atom			**Δ_m** μ_B/cell	**|M|** μ_B/cell
		Co	**Sn**	**Nb**		
HH	A	0 (0)	0 (0)	0 (0)	0 (0)	**0 (0)**
	B	2.3 (1.2)	0 (0)	1.8 (0)	0.1 (0)	4.2 (1.2)
	C	2.0 (0.5)	0 (0)	-0.6 (-0.2)	0 (0)	1.4 (0.3)
FH	A	1.6/1.6 (0.9/0.9)	0 (0)	-0.1 (0)	-0.1 (0)	**3.0** (1.8)
	B	1.6 (0.2)	-0.1/-0.1 (0/0)	-2.0 (0.4)	-0.5 (0)	1.1 (0.6)
	C	2.0 (0)	0 (0)	0/0 (0/0)	0 (0)	2.0 (0)

The TDOS and PDOS for HH-A are presented in Figures 4.7 (a-d), where a semiconductor character is observed from the GGA-PBE and HSE06 calculations. Also, in the region of E_f, Co(d) and Nb(d) orbitals is very present in VBT and CBB, where the d-splitting in t_{2g} and e_g symmetries is observed. As summarized in the Table 4.5, the band gap of 0.97 eV

was obtained from GGA-PBE calculation, in good agreement with previous work [54,55,122,135]. In contrast, a band gap of 1.5 eV was obtained with HSE06, which is slightly larger than 1.3 eV as reported in literature [54], although experimental measurements are 0.87 eV [62] and 1.00 eV [118], indicating that HSE06 approximation overestimates the band gap about 30%. However, as previously reported by Yan et al [59], the Co excess (or another element) in HH Nb alloys, can induce the formation the FH phases, what cause the reduction of band gap. This experimental issue was reported by Shan Li et al [62], who assigned exactly to occupation of 8c sites by Co atoms. As depicted in Figures 4.7 (e-l), the structures HH-B and HH-C presented conductor character. Figures 4.7 (h) and (l) show that Co(t_{2g}) and Nb(e_g) and Nb(t_{2g}) play an important hole to conductor character in two spin channels.

As presented in Figures 4.8 (a-d), a HM character is found for FH-A, although the literature [123,136] report a metallic behavior, where from HSE06 calculations, a band gap of 0.86 eV was obtained in spin down channel. Figures 4.8 (c) and (d), shows that Nb(d) has a strong presence at the Fermi level in the spin up channel, while HSE06 Co(d) in the VBT and CCB in the spin down channel. Structures FH-B and FH-C have conductor character, as demonstrated in Figures 4.8 (e-l).

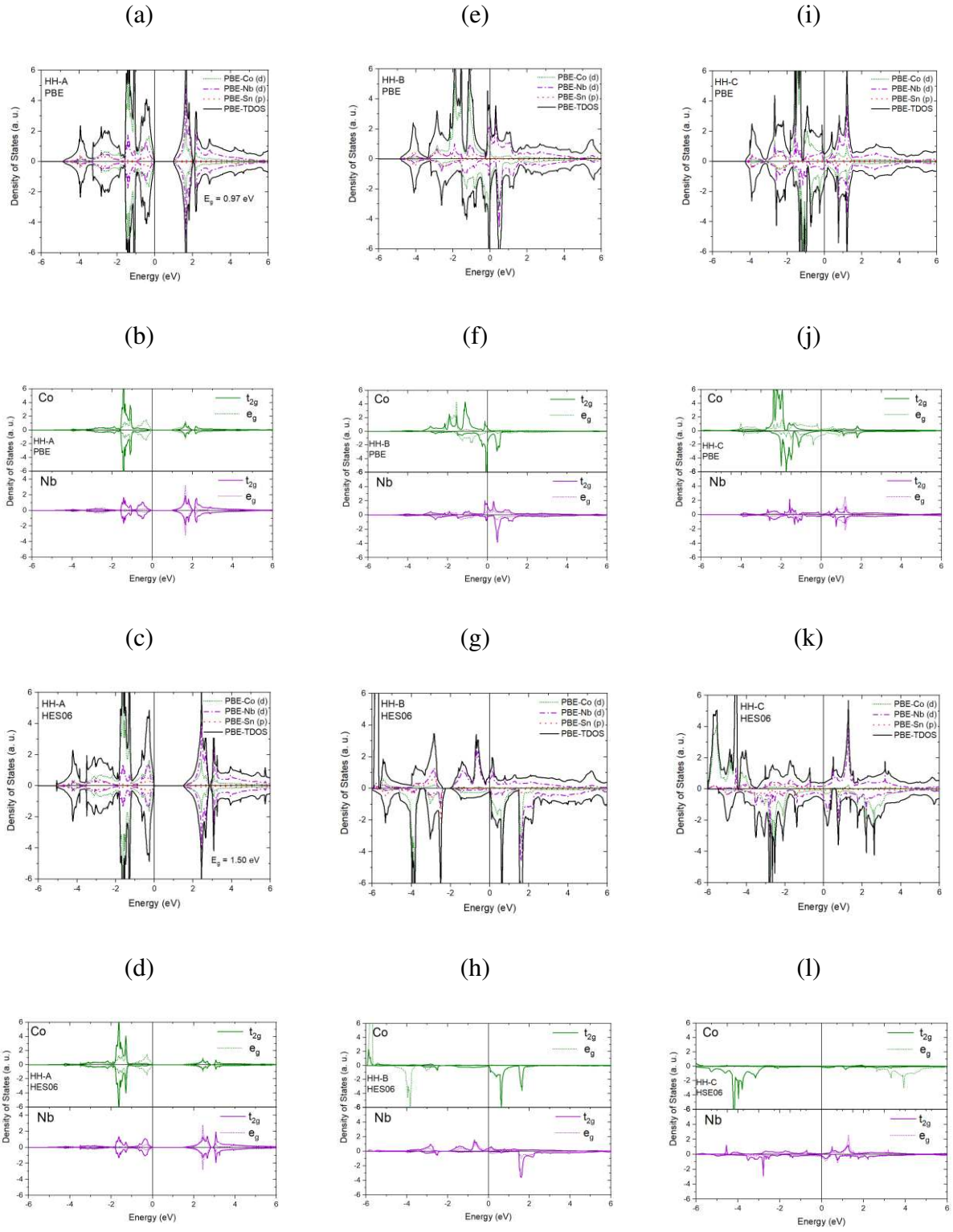

Figure 4.7: TDOS and PDOS for (a-b) HH-A, (c-d) HH-B and (e-f) HH-C niobium structures, obtained from PBE calculations; (g-h) HH-A, (i-j) HH-B and (k-l) HH-C niobium structures, obtained from HSE06 calculations.

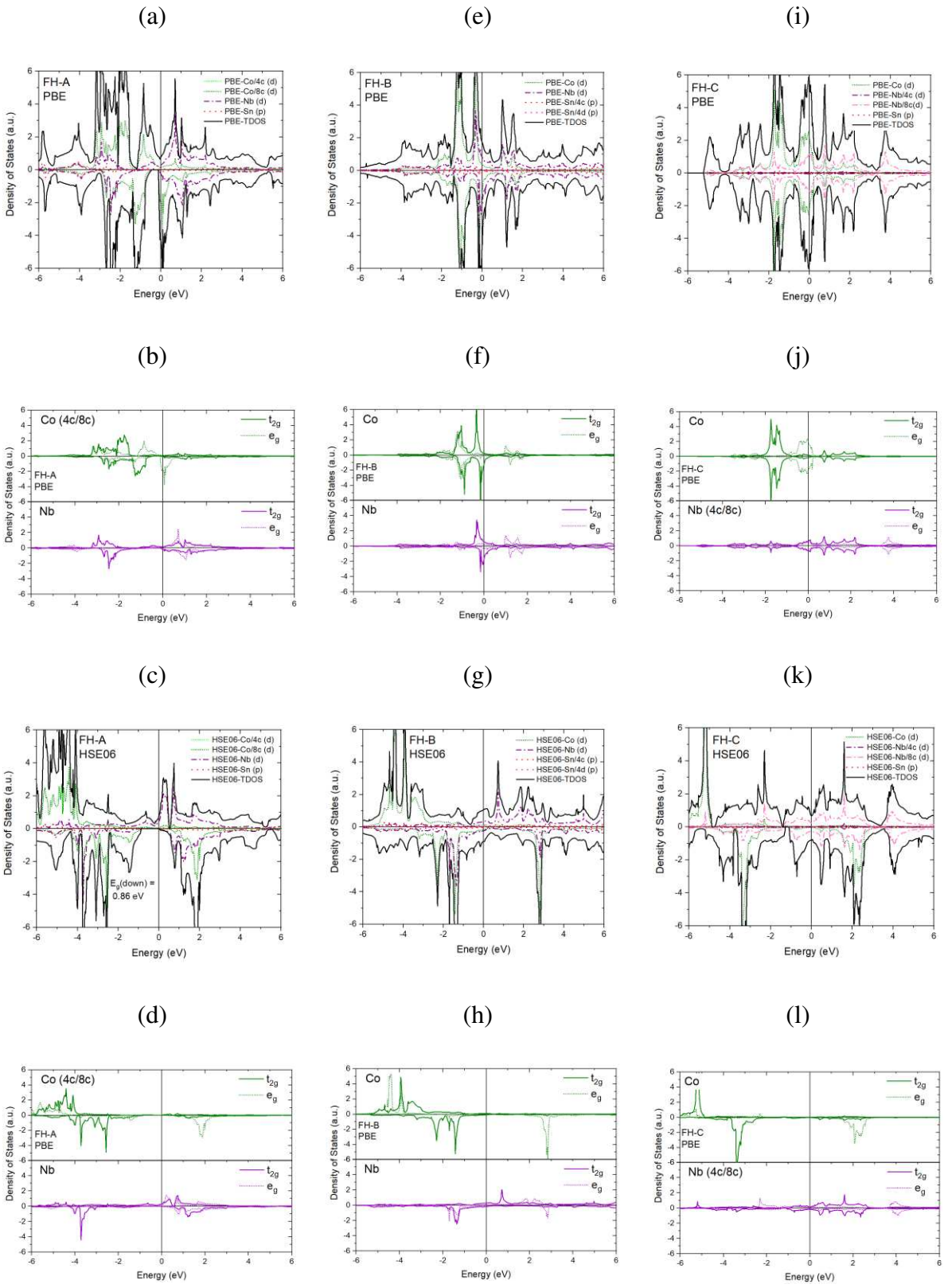

Figure 4.8: TDOS and PDOS for (a-b) FH-A, (c-d) FH-B and (e-f) FH-C niobium structures, obtained from PBE calculations; (g-h) FH-A, (i-j) FH-B and (k-l) FH-C niobium structures, obtained from HSE06 calculations.

4.2.3 Tantalum alloys

Table 4.7 presents the magnetic moment for the Ta alloys. From HSE06 calculations, HH-A and FH-A structures are in accordance with Slater-Pauling rule, respectively, in diamagnetic and ferromagnetic configurations. For FH-B structure, it is observed a larger contribution of the interstitial region of the crystal (Δ_m) to the total magnetic moment.

Table 4.7 - Local (m) and total (M) magnetic moments of the structures HH and FH for (Co-Ta-Sn) alloys from HSE06 (GGA-PBE) calculation. Magnetic moments calculated with GGA-PBE for comparation. Δ_m represents the contribution of interstitial region of the crystal. Values of M in bold are in accordance with the Slater-Pauling rule.

Alloys		**m** μ_B/atom			**Δ_m** μ_B/cell	**|M|** μ_B/cell
		Co	**Sn**	**Ta**		
HH	A	0 (0)	0 (0)	0 (0)	0 (0)	**0 (0)**
	B	2.2 (0.3)	0 (0)	0.8 (0)	0 (0)	3.0 (0.3)
	C	2.0 (0.2)	0 (0)	-0.4 (0)	0 (0)	1.6 (0.2)
FH	A	1.5/1.5 (0.7/0.7)	0 (0)	0 (0)	0 (0)	**3.0** (1.4)
	B	1.5 (0.2)	0/0 (0/0)	-1.5 (0.2)	1.0 (0)	1.0 (0.4)
	C	2.0 (1.3)	0 (0)	0/0 (0/0)	0 (0)	2.0 (1.3)

PDOS and TDOS for HH tantalum alloys are presented in Figure 4.9. According to Figures 4.9 (a-d) HH-A presents a semiconductor character and band gap of 1.04 eV (1.18 eV) form GGA-PBE (HSE06) calculations, which are in good accordance with previous theoretical results [62,118,127,128,137], as shown in Table 4.5. However, experimental measurements have a considerable interval of values 0.57-1.8 eV [61,62]. This fact could be associated with the presence of Co atoms in the 8c sites, leading to the formation of FH phases. As shown in Figures 4.9 (e-l) HH-B and HH-C have a conductor character, according to GGA-PBE and HSE06 calculations, although there are discrepancies between both approximations regarding the positioning of the d-orbitals. Figure 4.9 (h) show that Co(t_{2g}) plays an important role to conductor character in the spin down channel of FH-B, while Ta(e_g) and Ta(t_{2g}) guarantee this

behavior in spin up channel. In case of FH-C, Figure 4.9 (l) shows that Co(e_g), Co(t_{2g}), Ta(e_g) and Ta(t_{2g}) have a small presence near Fermi level.

Figure 4.10 shows TDOS and PDOS for FH tantalum alloys FH. As depicted in Figures 10 (a-d) a disagreement between GGA-PBE and HSE06 results is observed for FH-A structure, where a conductor and HM character are observed, respectively. The conductor character was predicted previously by Dutt and Chakrabarti [138] from the mBJ functional. In this work, a band gap of 1.36 eV in spin up channel was obtained from hybrid functional HSE06. To date, no experimental measurements have been found in the literature. As shown in Figures 4.10 (e-l) a conductor character is observed for FH-B and FH-C structures in GGA-PBE and HSE06 calculations, although there are discrepancies between both approximations regarding the positioning of the d-orbitals. As discussed previously, GGA-PBE is not accurate for describing strongly correlated systems. Therefore, more complex calculations are necessary, for instance, using hybrid functionals.

As discussed in this section: i) the Slater-Pauling rule was entirely confirmed, within HSE06 approximation, for those structures that have Co in the sites 8c/4c; ii) GGA-PBE approximation is insufficient to calculate and describe the electronic and magnetic properties of HH and FH structures; and iii) it was observed that Co-VB-Sn in the HH-A structures have semiconductor character, while FH-A structures half-metal nature. Finally, since that stability and semiconductor behavior are fundamental to development of thermoelectric, the study of HH-A and FH-A structures are presented in the next sections.

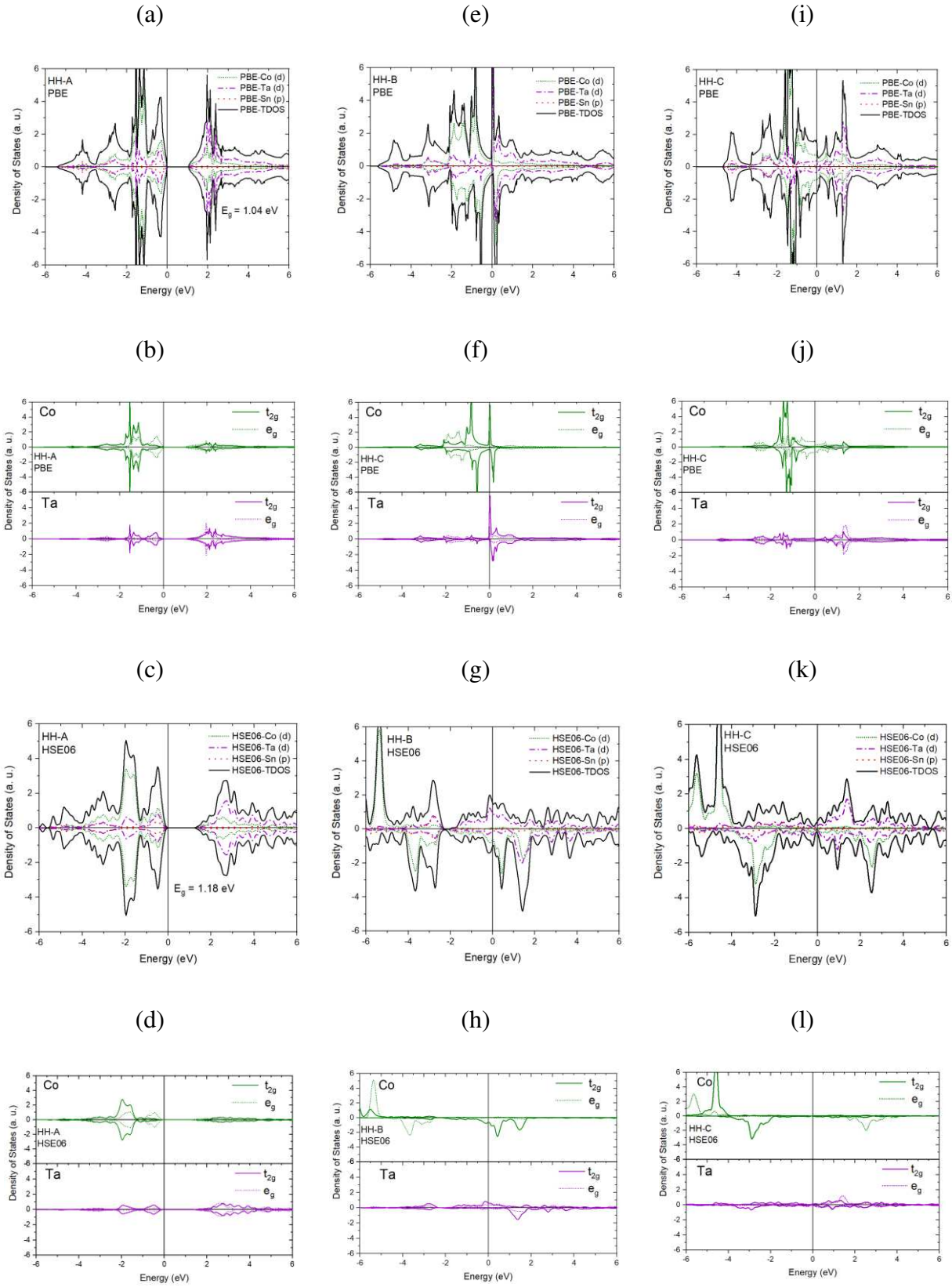

Figure 4.9: TDOS and PDOS for (a-b) HH-A, (c-d) HH-B and (e-f) HH-C tantalum structures, obtained from PBE calculations; (g-h) HH-A, (i-j) HH-B and (k-l) HH-C tantalum structures, obtained from HSE06 calculations.

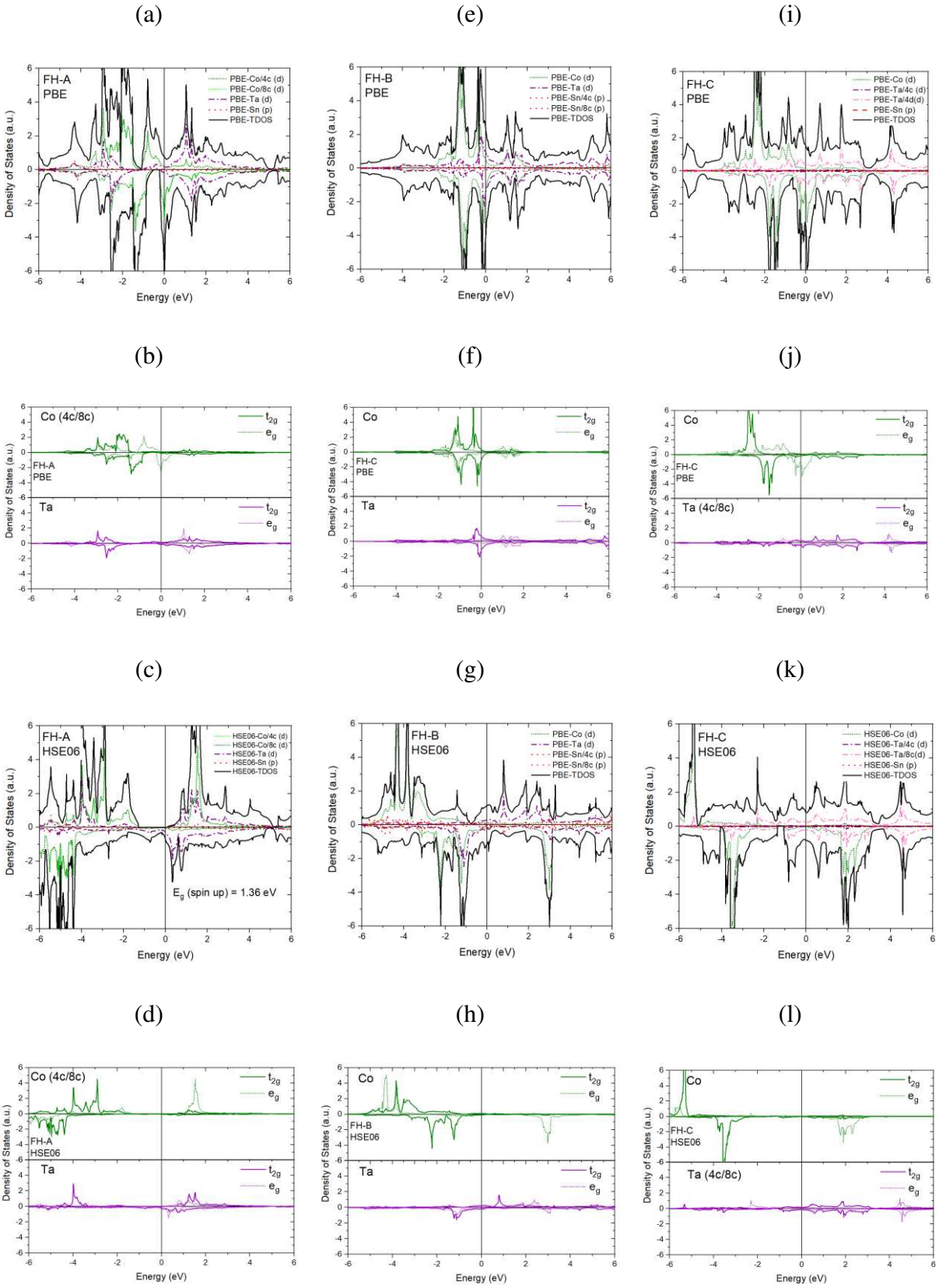

Figure 4.10: TDOS and PDOS for (a-b) FH-A, (c-d) FH-B and (e-f) FH-C structures tantalum, obtained from GGA-PBE calculations; (g-h) FH-A, (i-j) FH-B and (k-l) FH-C tantalum structures, obtained from HSE06 calculations.

4.3 Effective Mass and SOC

Based on the analysis of the bandstructure, the effects of the spin–orbit coupling (SOC) were studied in the Heusler alloys. Also, electrons (m_e^*) and hole (m_h^*) effective masses within parabolic approximation were obtained for the Heusler alloys structure along the high symmetry directions in the Brillouin Zone. Calculations were performed with and without SOC, and called GGA-PBE and GGA-PBE+SOC, respectively.

4.3.1 Vanadium alloys

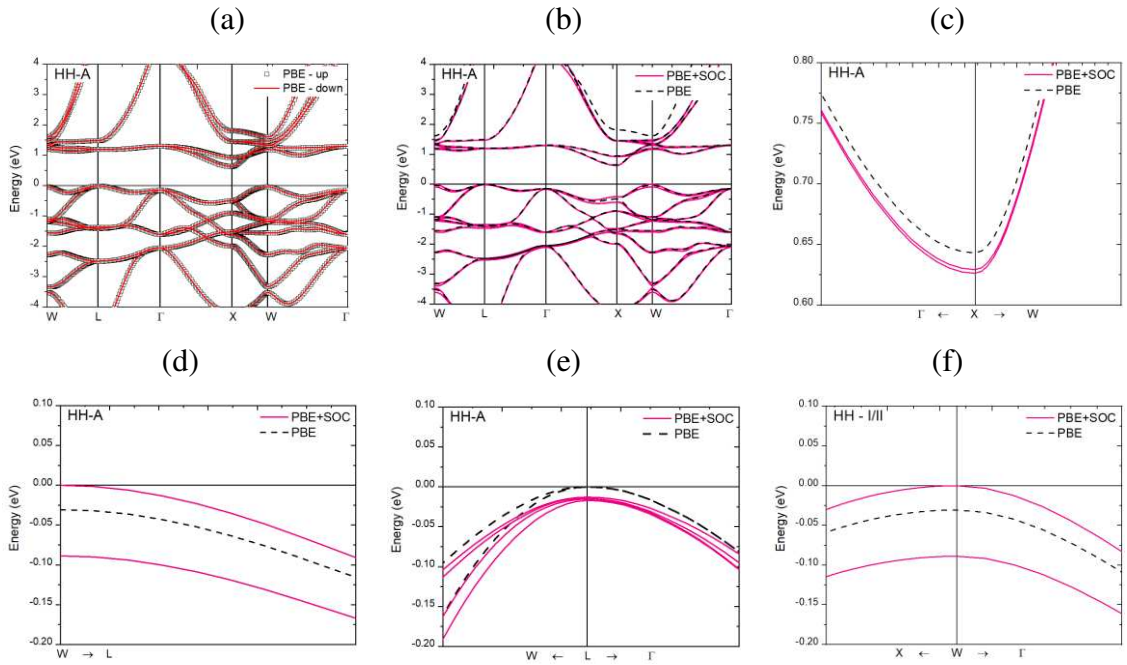

Figure 4.11: Bandstructure of vanadium HH-A alloy (a) GGA-PBE spin up and down (b) GGA-PBE+SOC (c) CBB Γ - X - W (d) VTB W – L (e) VTB W - L - Γ (f) VTB X - W – Γ.

The GGA-PBE calculation of bandstructure of the Vanadium HH-A is presented in the Figure 4.11 (a). In agreement with density of states results, it is observed a semiconductor behavior with symmetric spin up and down bands. Figure 4.11 (b) presents a comparation of bandstructures obtained from GGA-PBE and GGA-PBE+SOC calculations (black dotted line represents the equivalent GGA-PBE up and down bands). Figure 4.11 (c) show a zoomed CBB around the high symmetry point X, where a split is observed. This fact caused a slight decrease in the band gap from 0.64 eV to 0.61 eV. A spin band degeneracy at the point X is observed, where the degeneracy factor is $N_{d,CBB} = 2$ (see Section 2.10). Figures 4.11 (d-f) show the zoomed VBT around the high symmetry points L and W. From GGA-PBE, there is an indirect

band gap L → X of 0.64 eV, where L has a degeneracy factor $N_{d,VTB} = 4$. On the other hand, an indirect band gap W → X of 0.61 eV is observed, when SOC effect is taken into account, with degeneracy factor $N_{d,VTB} = 1$.

Table 4.8 - Effective masses of CoVSn HH-A.

Particle	Path	GGA-PBE	PBE+SOC
$\mathbf{m_e^*}$	X - Γ	**1.82**[a]	**1.82**
$\mathbf{m_e^*}$	X - W	**0.31**	**0.31**
$\mathbf{m_{e,dos}^*}$	-	1.62	1.62
$\mathbf{m_h^*}$	L - Γ	**4.53**	**2.69**
$\mathbf{m_{hh}^*}$	L – W	**0.86**	**1.24**
$\mathbf{m_{lh}^*}$	L - W	0.60	0.85
$\mathbf{m_h^*}$	W - L	0.34	0.31
$\mathbf{m_h^*}$	W - Γ	1.10	1.04
$\mathbf{m_h^*}$	W - X	**1.69**	**1.74**
$\mathbf{m_{h,dos}^*}$	-	4.72	1.80

[a]The effective masses used in the Equation 2.67 to calculate $m_{e,DOS}^*$ and $m_{h,DOS}^*$ are presented in bold.

As already mentioned in Section 2.10, the effective mass is an important parameter in the study of TE materials. In this work, electrons (m_e^*) and hole (m_h^*) effective masses were obtained for HH-A vanadium alloy along the high symmetry directions in the Brillouin Zone. Within parabolic approximation, the calculations GGA-PBE and GGA-PBE+SOC are listed in Table 4.8. Considering that X point is the Conduction Band Bottom (CBB), an important anisotropy was observed in the effective masses of electron considering the X-Γ and X-W directions, i.e., $1.82m_0^*$ and $0.31m_0^*$, respectively. In addition, SOC effect is not important here.

On the other hand, the electron density state effective masses ($m_{e,DOS}^*$) were determined by fitting the FEA 2.68 equation with the values calculated from the DFT theory, around the Fermi level. That is, in the energy regions near TVB and CBB. Considering $N_{d,CBB} = 2$ are equal, was obtained $m_{e,DOS}^* = 1.62\ m_0^*$ from to both calculation, GGA-PBE and GGA-PBE+SOC, as seen in the Figure 4.12 (a) and (b). This result is smaller than $m_{e,DOS}^* = 1.90m_0^*$ as reported previously by Guo et al [142].

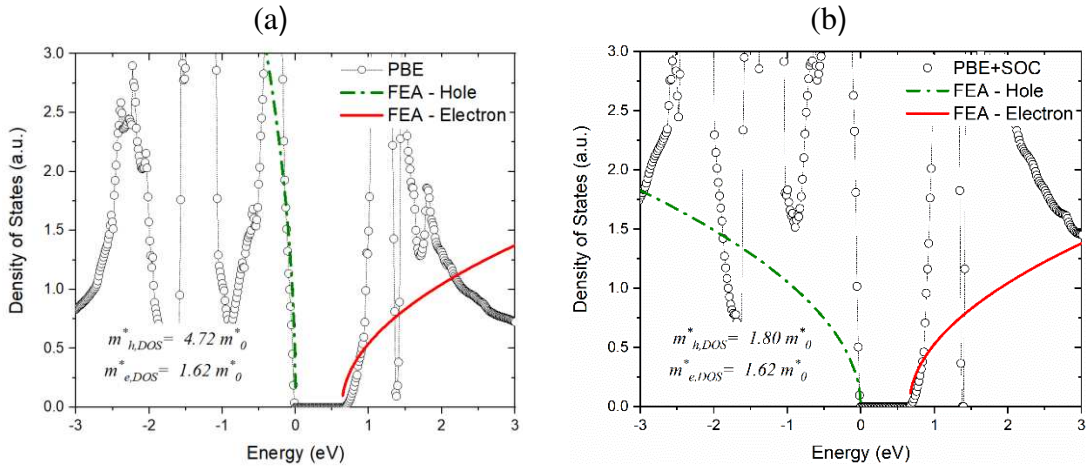

Figure 4.12: TDOS of HH-A vanadium structure obtained from (a) PBE (b) PBE-SOC. Curve adjusted by Equation 2.68, within free electron approximation (FEA), using the respective effective mass.

The hole effective masses were calculated around the k-points L (TVB) and W. In the L-Γ direction, a slight decrease from $4.53m_0^*$ to $2.69m_0^*$ (40.6% lower) from GGA-PBE and GGA-PBE+SOC, respectively. For GGA-PBE calculation, the L-W path present $0.86m_0^*$ and $0.60m_0^*$ for heavy (m_{hh}^*) and light (m_{lh}^*) holes effective mass. Considering GGA-PBE+SOC, an increase to $1.24m_0^*$ (30% higher) is seen for m_{hh}^* and an increase to $0.85m_0^*$ (30% higher) for m_{lh}^*. Around W point, the lowest m_h^* equal to $0.34m_0^*$ was observed along the W-L direction. In general, the SOC effect is not substantial in the directions around the point W. The hole density state effective masses ($m_{h,DOS}^*$) were calculated, where $m_{h,DOS}^* = 4.72\ m_0^*$ and $m_{h,DOS}^* = 1.80\ m_0^*$ from GGA-PBE ($N_{d,VTB} = 4$) and GGA-PBE+SOC ($N_{d,VTB} = 1$), respectively.

4.3.2 Niobium alloys

The GGA-PBE bandstructure of Niobium HH-A is shown in the Figure 4.13 (a), where a semiconductor character is observed in spin up and down channels, and an indirect band gap. Figure 4.13 (b) presents a comparation of bandstructures obtained with GGA-PBE and GGA-PBE+SOC (black dotted line represents the equivalent up and down bands). Figure 4. 13 (c) shows a zoomed CBB in the vicinity of the high symmetry point X. SOC effects cause a decrease of energy of CBB. Furthermore, a band split is observed in the X → W direction. For both GGA-PBE and GGA-PBE+SOC, the band degeneracy factor $N_{d,CBB} = 2$ is observed.

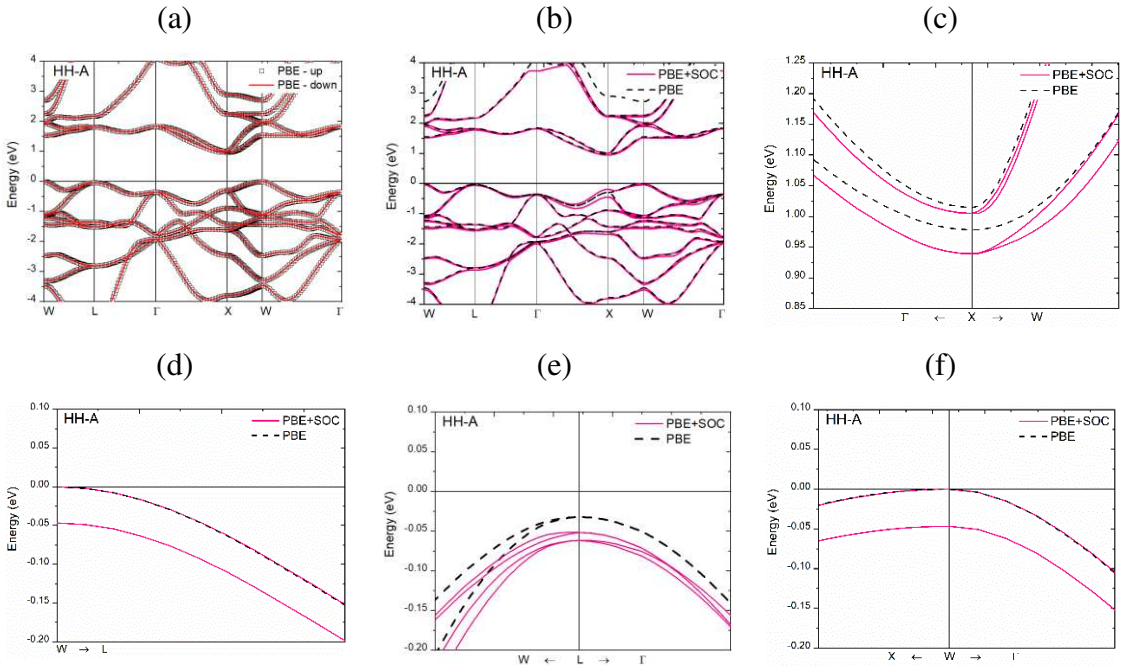

Figure 4.13: Bandstructure of niobium HH-A (a) GGA-PBE spin up and down (b) GGA-PBE+SOC (c) CBB Γ - X - W (d) VTB W – L (e) VTB W - L - Γ (f) VTB X - W – Γ.

Figures 4.13 (d-f) show the zoomed VBT around L and W points. Both GGA-PBE and GGA-PBE+SOC calculations presented an indirect bandgap W→ X of 0.97 eV and 0.93 eV, respectively. Due to SOC, a split-off energy of 47.0 meV occurs at the W point, and the energies in the L point are 32.0 (GGA-PBE) and 50.6 meV (GGA-PBE+SOC) from E_f.

The electron and hole effective masses were calculated within GGA-PBE and GGA-PBE+SOC approximations, as listed in Table 4.9. Considering the lowest conduction band around X point, the electron effective masses were obtained in X→ Γ and X→ W directions. From GGA-PBE (GGA-PBE+SOC) calculations, $m_e^* = 2.07m_0^*$ ($1.62m_0^*$) in the X → Γ direction, while $m_e^* = 1.23m_0^*$ ($0.59m_0^*$) in the path X → W. So, the SOC effect decreases m_e^*. For VBT, the hole effective masses were calculated in W→ L and W→ X and W→ Γ directions, where SOC effect is not very important, as shown in Table 4.9.

Table 4.9 - Effective masses of CoNbSn HH-A.

Particle	Path	GGA-PBE	PBE+SOC
$\mathbf{m_e^*}$	X - Γ	**2.07**[a]	**1.62**
$\mathbf{m_{he}^*}$	X - W	**1.23**	**0.59**
$\mathbf{m_{le}^*}$			0.41
$\mathbf{m_{e,dos}^*}$	-	1.97	1.84
$\mathbf{m_h^*}$	L - Γ	**3.33**	**3.11**
$\mathbf{m_{hh}^*}$	L – W	0.72	0.62
$\mathbf{m_{lh}^*}$	L - W	0.49	0.59
$\mathbf{m_h^*}$	W - L	0.23	0.23
$\mathbf{m_h^*}$	W - Γ	**0.72**	**0.79**
$\mathbf{m_h^*}$	W - X	**2.28**	**2.18**
$\mathbf{m_{h,dos}^*}$	-	2.80	1.61

[a]The effective masses used in the Equation 2.67 to calculate $m^*_{e,DOS}$ and $m^*_{h,DOS}$ are presented in bold.

By fitting the FEA 2.68 equation with the values calculated from the DFT theory, around the Fermi level, and considering, $N_{d,VTB} = 2$ (GGA-PBE) and $N_{d,VTB} = 1$ (GGA-PBE+SOC), the following electron and hole density of state effective mass were obtained from GGA-PBE (GGA-PBE+SOC) calculations, $m^*_{e,DOS} = 2.80m_0^*(1.84m_0^*)$ and $m^*_{h,DOS} = 1.97m_0^*(1.75m_0^*)$.

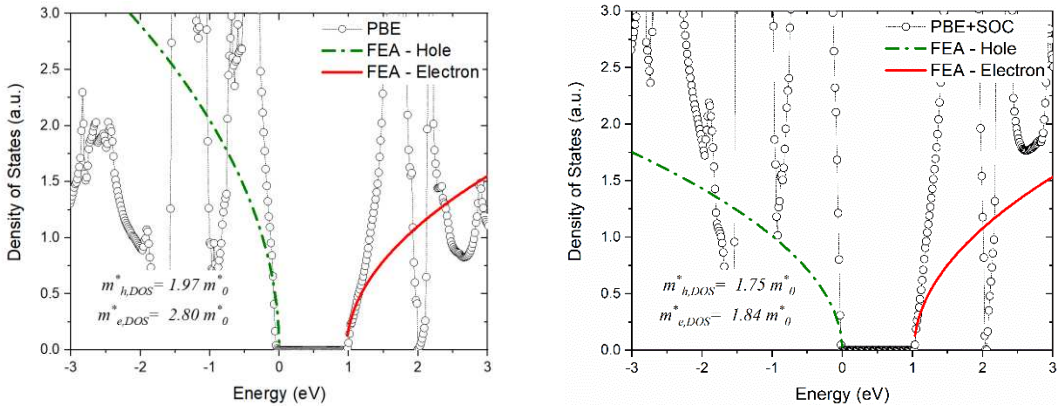

Figure 4.14: TDOS of HH-A niobium structure obtained from (a) PBE (b) PBE-SOC. Curve adjusted by Equation 2.68, within free electron approximation (FEA), using the respective effective mass.

4.3.3 Tantalum alloys

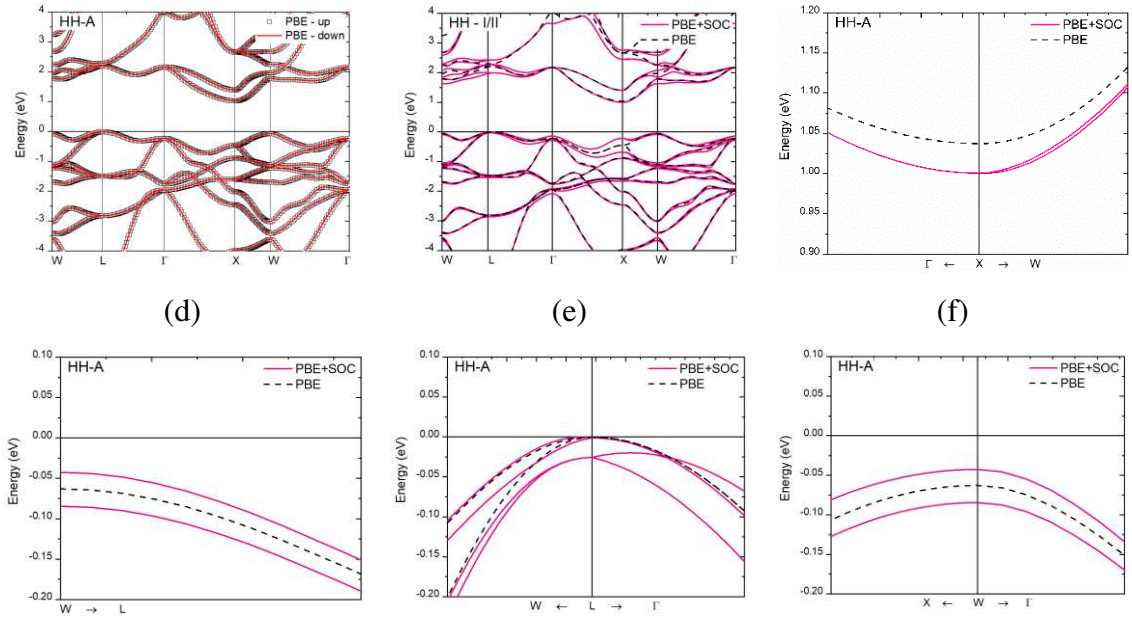

Figure 4.15: Bandstructure for tantalum HH-A (a) GGA-PBE spin up and down (b) GGA-PBE+SOC (c) CBB Γ - X - W (d) VTB W – L (e) VTB W - L - Γ (f) VTB X - W – Γ.

The bandstructure of Tantalum HH-A is shown in Figure 4.15 (a), where a semiconductor character is observed in symmetric spin up and down channels, and a indirect L → X bandgap. Figure 4.15 (b) presents the bandstructures obtained from GGA-PBE and GGA-PBE+SOC calculations. The SOC effects cause a decrease in the band gap from 1.04 eV to 1.00 eV. Figure 4.15 (c) shows a zoomed CBB in the vicinity of the high symmetry point X, where a band slightly split is observed in the X→ W direction. For both GGA-PBE and GGA-PBE+SOC calculations, it was defined a degeneracy factor $N_{d,CBB} = 2$. Figures 4.15 (d-f) show the zoomed VBT around L and W points. At the L point, GGA-PBE calculation predict $N_{d,VTB} = 4$, and $N_{d,VTB} = 2$ when SOC effect is taken into account. A split-off energy of 25.0 meV is observed.

The electron and hole effective masses were determined from GGA-PBE and GGA-PBE+SOC calculation, as presented in Table 4.10. Considering the CBB around X point, an important anisotropy was observed for the effective masses of electron in the X→ Γ and X→W directions, i.e., $2.29m_0^*$ ($1.96m_0^*$) and $1.07m_0^*(0.74m_0^*)$, respectively. This way, the SOC effect indicates a significant m_e^* reduction of 14% and 31% for X→ Γ and X→W, respectively. By fitting the FEA 2.68 equation with the values calculated from the DFT theory, around the Fermi level, and considering, $N_{d,VTB} = 4$ (GGA-PBE) and $N_{d,VTB} = 2$ (GGA-PBE+SOC), the following

electron and hole density of state effective mass were obtained from GGA-PBE (GGA-PBE+SOC) calculations, $m^*_{e,DOS} = 2.82m^*_0(2.24m^*_0)$ and $m^*_{h,DOS} = 4.58m^*_0(4.19m^*_0)$. These results are comparable with $m^*_{e,DOS} = 2.96m^*_0$, previously reported [142].

Table 4.10 - Effective masses of CoTaSn HH-A.

Particle	Path	GGA-PBE	PBE+SOC
$\mathbf{m^*_e}$	X - Γ	**2.29**	**1.96**
$\mathbf{m^*_e}$	X - W	**1.07**	**0.74**
$\mathbf{m^*_{e,dos}}$	-	2.82	2.24
$\mathbf{m^*_h}$	L - Γ	**4.20**	**3.88**
$\mathbf{m^*_{hh}}$	L – W	**0.760**	**0.550**
$\mathbf{m^*_{lh}}$	L - W	0.440	0.530
$\mathbf{m^*_h}$	W - L	0.310	0.310
$\mathbf{m^*_h}$	W - Γ	1.05	1.02
$\mathbf{m^*_h}$	W - X	**1.88**	**2.16**
$\mathbf{m^*_{h,dos}}$	-	4.58	4.19

[a]The effective masses used in the Equation 2.67 to calculate $m^*_{e,DOS}$ and $m^*_{h,DOS}$ are presented in bold.

(a) (b)

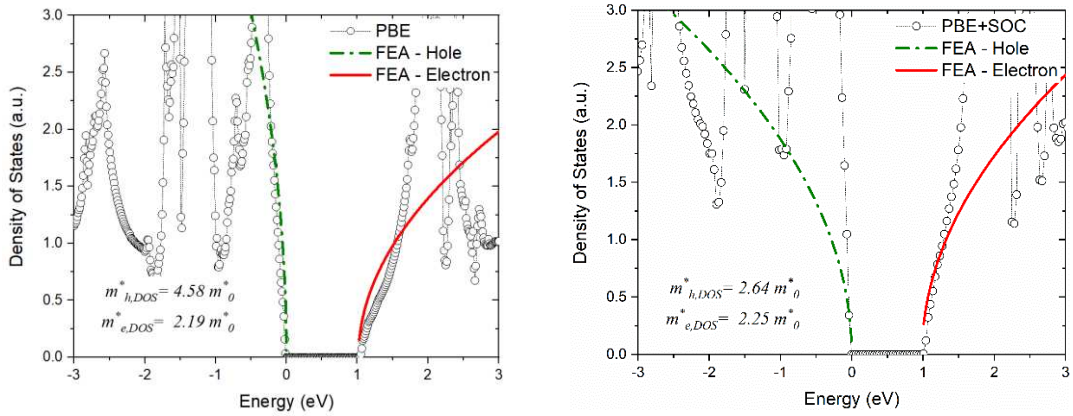

Figure 4.16. TDOS of CoNbSn HH-A structure obtained from (a) PBE (b) PBE-SOC calculation and adjusted by Equation 2.68, within free electron approximation (FEA).

In addition, the hole effective masses were obtained at the TVB. In the L→Γ direction, a slight decrease from $4.20m_0^*$ to $3.88m_0^*$ (8% lower) is obtained when SOC effect is considered. On the other side, in the L→W direction, the effective masses are $0.760m_0^*$ and $0.440m_0^*$ for heavy (m_{hh}^*) and light (m_{lh}^*) holes, respectively. From SOC calculations, a decrease to $0.550m_0^*$ (28% lower) is seen for m_{hh}^* and an increase to $0.530m_0^*$ (20% higher) for m_{lh}^*.

In general, the HH-A Vanadium, Niobium and Tantalum alloys presented high values of $m_{h,DOS}^*$ and $m_{e,DOS}^*$. This is mainly due to the localized 3d states, which cause the bands to present a flat dispersion [143] as well as a high degeneracy factor. Moreover, SOC effect generally decreases the $m_{h,DOS}^*$, mainly due to the decrease in $N_{d,VTB}$.

4.4 Chemical Bonds

This section presents the results to Bader charge, ELF and charge density for the Co-VB-Sn structures. The chemical bonds were analyzed in the crystallography plans $(1\bar{2}1)$ and (101), as represented in Figure 4.17. The calculations were carried out within the HSE06 approximation.

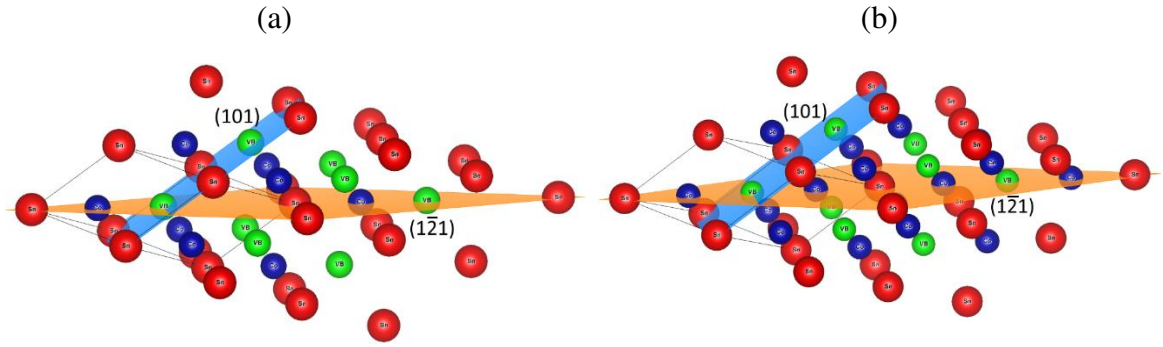

Figure 4.17. Representation of crystallography plans $(1\bar{2}1)$ and (101) in the a) HH-A and b) FH-A structures.

4.4.1 Vanadium alloys

Table 4.11 presents the Bader Charge for Vanadium HH and FH alloys. For all structures, Co has a negative or zero charge, V has a positive charge, while Sn has a more significant negative charge for structures B and C. Also, lower Sn and Co charges are observed in the HH-A and HH-C structures. So, despite the Sn atom having greater electronegativity and atomic radius, the polarization in the direction Co(4c)-V(4a/4b) is favored by the occupation of site 4c by Co in HH-A. In the other cases, HH-B and HH-C, the polarization in the Sn(4c)-

V(4a/4b) and V(4c)-Sn(4a/4b) directions are most favorable. Thus, it was observed that the type of atom located in the 4c/8c position plays an important hole for the polarization in the HH crystals.

Regarding the Bader charge sign, a similar result was found for FH structures. And as there are two atoms located in the respective 4c and 8c sites, the charge is reduced by approximately half the value found for HH structures. Additionally, it was verified that SOC effect does not change the Bader charges and, therefore, the nature of the chemical bonds.

Table 4.11 – Bader Charge q (|e|) obtained from HSE06 calculations for vanadium. Values in bold represent the atoms in the 4c/8c sites.

Crystal	**Atom**	**Structure**		
		A	**B**	**C**
HH	**Co**	**-1.14**	-0.13	0.00
	Sn	0.09	**-0.67**	-0.56
	V	1.05	0.80	**0.56**
FH	**Co**	**-0.44**[a]	0.00	-0.42
	Sn	0.07	**-0.18**[a]	-0.88
	V	0.81	0.36	**0.65**[a]

[a]Bader charge per atom in the 4c and 8c sites.

Figures 4.18 (a) and (b) show the charge density for HH-A and FH-A vanadium structures, respectively.[1] As the atomic radius of vanadium (R_V = 1.35 Å) is smaller than that of tin (R_{Sn} = 1.45 Å), the charge density has similar plot in the Co-Sn and Co-V directions, although greater polarization in observed Co-V direction, as shown by the Bader Charges results. Figure 4.18 (c) shows the ELF for HH-A vanadium structure, where an attractor (as indicated by the arrow) located between the Co and V atoms indicates a covalent-polar bond characteristic[2]. For FH-A structure, Figure 4.18 (d) indicates an absence of attractor in Co-V direction, while higher ELF values are present in Sn-V directions. This can be explained by

[1] The criteria for choosing the isosurface were based on main chemical bonds.

[2] The criteria for choosing the isosurface were based on the most appropriate analysis of the ELF functions.

greater electronegativity of Sn and the net charge of cobalt in the FH-A structure (-0.44 |e|) being much lower than of cobalt in the HH-A structure (-1.14 |e|), as shown in Table 4.11.

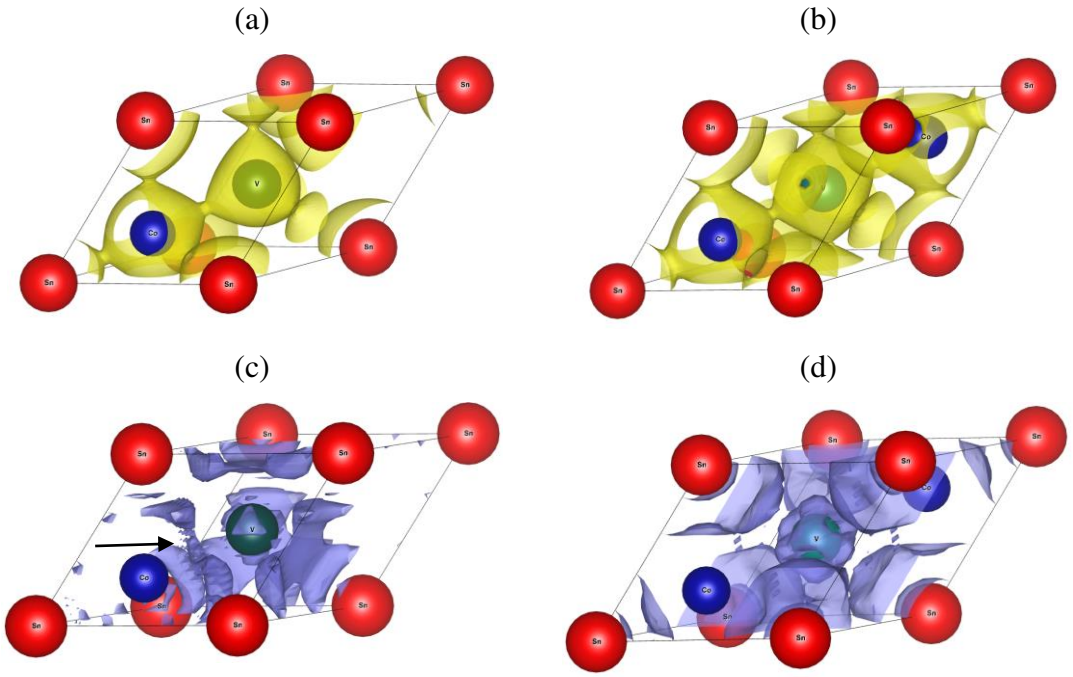

Figure 4.18. Charge density of a) HH-A vanadium with isosurface: 0.055 eÅ^{-3}, b) FH-A vanadium with isosurface: 0.044 eÅ^{-3}; and Electron localization function of c) HH-A vanadium with isosurface: 0.22, and d) FH-A vanadium with isosurface: 0.16.

Figure 4.19 (a) shows the ELF plots on the $(1\bar{2}1)$ and (101) planes of HH-A structure. For $(1\bar{2}1)$ plane, ELF presents larger values in-between the Sn-Co-V direction, approximately in the middle of the bond axis. On the other hand, from Bader analysis, it was obtained a charge equal to -1.14 |e| for Co, equal to +1.05 |e| for V and almost zero for Sn. Furthermore, the ELF is asymmetric around Co, i.e., displaced to one side of its nucleus. Thus, a covalent-polar bond is observed in the Sn-Co-V direction. As previously discussed, in Figure 4.5 (c), PDOS indicated that the bond occurs mainly by Sn(p)-Co(d)-V(d) orbitals hybridization. In the (101) plane, it is observed that in the vicinity of Sn the ELF assumes higher values, where bonds occur in the Sn-V direction.

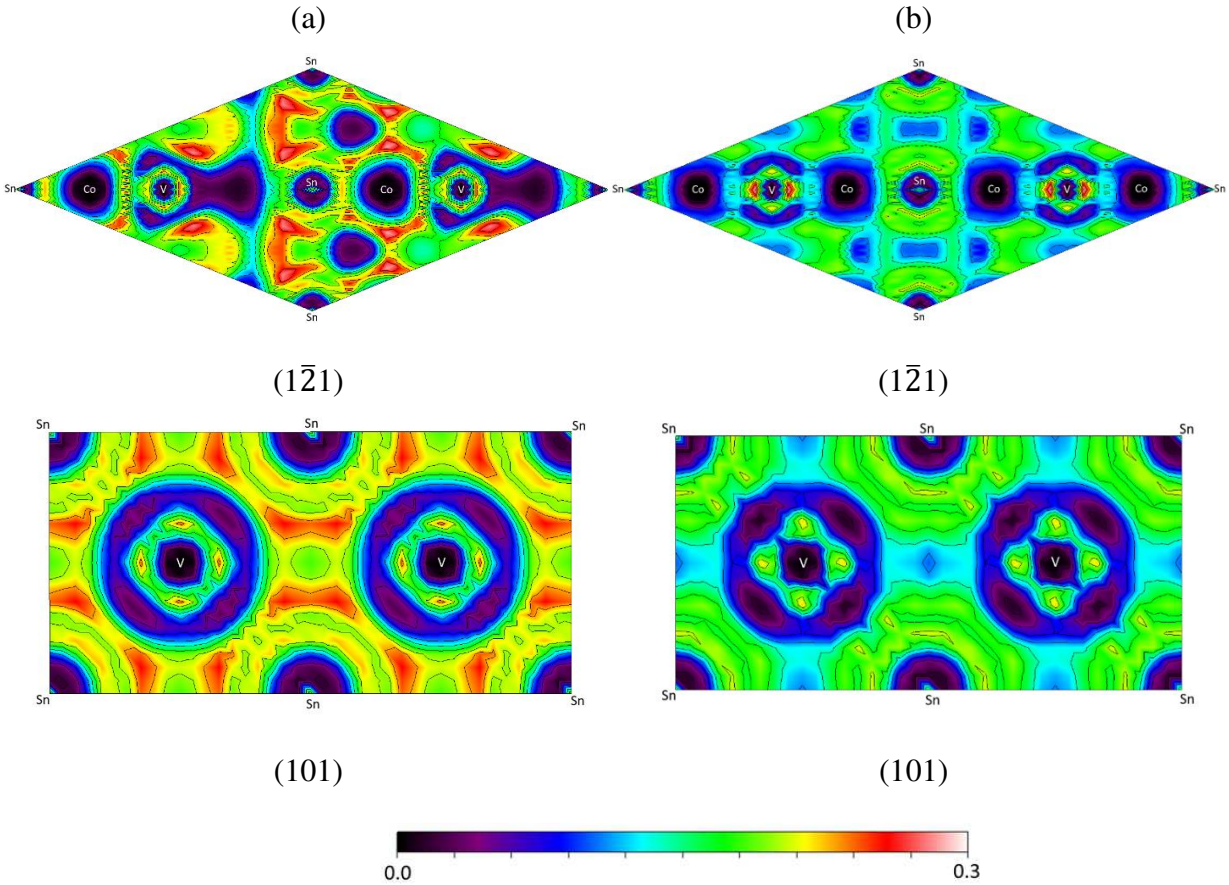

Figure 4.19. Electron localization function obtained from HSE06 calculations in the planes (1$\bar{2}$1) and (101) for a) HH-A and b) FH-A vanadium structures.

Figure 4.19 (b) presents the ELF plots on the (1$\bar{2}$1) and (101) planes of FH-A structure. In the plane (1$\bar{2}$1), the presence of Co in the 8c site in addition to the 4c site, induced a smaller electronic localization around them, when compared to the HH-A structure. This result is corroborated by the values presented for the Bader charge equal to -0.44 |e| per Co atom at sites 4c and 8c, while for V atom is equal to +0.81 |e|. Thus, it is observed that a covalent-polar bond remains in the Sn-Co-V direction, with a decrease in polarization. As shown in Figure 4.6 (c), PDOS indicated that the bond occurs mainly by Co(d)-V(d) orbitals hybridization, with a reduced contribution from Sn(p) orbitals. In the (101) plane, it is observed that in the vicinity of Sn the ELF assumes higher values, where bonds occur in the Sn-V direction.

4.4.2 Niobium alloys

The Bader charged for Niobium structures are presented in Table 4.12. Similar to Vanadium alloys, Nb assumes positive charge, while Co and Sn charges depend of Wyckoff position. Thus, a polarization is observed in the directions Co(4c)-Nb(4a/4b), Sn(4c)-

Nb(4a/4b), Nb(4c)-Sn(4a/4b), respectively, for the HH-A, HH-B and HH-C structures. In the structures HH-B and HH-C, Sn assumes a more negative charge, while Co in HH-A structure.

Concerning the Bader charge sign, a similar result was found for FH structures. And as there are two atoms located in the respective 4c and 8c sites, the charge per atom is reduced as compared with HH structures. Additionally, it was verified that SOC effect does not change the Bader charges and, therefore, the nature of the chemical bonds.

Table 4.12 – Bader Charge q (|e|) obtained from HSE06 calculations. Values in bold represent the atoms in the 4c/8c sites.

Crystal	**Atom**	**Structure**		
		A	**B**	**C**
HH	**Co**	**-1.11**	0.11	-0.09
	Sn	-0.01	**-0.84**	-0.46
	Nb	1.12	0.73	**0.55**
FH	**Co**	**-0.49**[a]	-0.03	-0.28
	Sn	0.09	**-0.17** [a]	-0.64
	Nb	1.07	0.35	**0.46**[a]

[a]Bader charge per atom in the 4c and 8c sites.

Figures 4.20 (a) and (b) show the charge density for HH-A and FH-A niobium structures, respectively. The charge density is present in the Co-Nb direction, unlike the Co-Sn direction. Figure 4.18 (c) shows the ELF for HH-A niobium structure, where an attractor (as indicated by the arrow) located between the Co and Nb atoms indicates a covalent-polar bond characteristic. For FH-A structure, Figure 4.18 (d) indicates an absence of attractor in Co-Nb direction, while higher ELF values are present in Sn-Nb directions. This can be explained by greater electronegativity of Sn and the net charge of cobalt in the FH-A structure (-0.49 |e|) being much lower than of cobalt in the HH-A structure (-1.11 |e|), as shown in Table 4.12.

Figure 4.21 (a) shows the ELF plots on the $(1\bar{2}1)$ and (101) planes of HH-A structure. For $(1\bar{2}1)$ plane, ELF presents larger values in-between the Sn-Co-Nb direction, approximately in the middle of the bond axis. On the other hand, from Bader analysis, it was obtained a charge equal to -1.11 |e| for Co, equal to +1.12 |e| for Nb and almost zero for Sn. Furthermore, the ELF is asymmetric around Co, i.e., displaced to one side of its nucleus. Thus, a covalent-polar bond is observed in the Sn-Co-Nb direction. As previously discussed, in Figure 4.7 (c), PDOS

indicated that the bond occurs mainly by Sn(p)-Co(d)-Nb(d) orbitals hybridization. In the (101) plane, it is observed that in the vicinity of Sn the ELF assumes higher values, where bonds occur in the Sn-Nb direction.

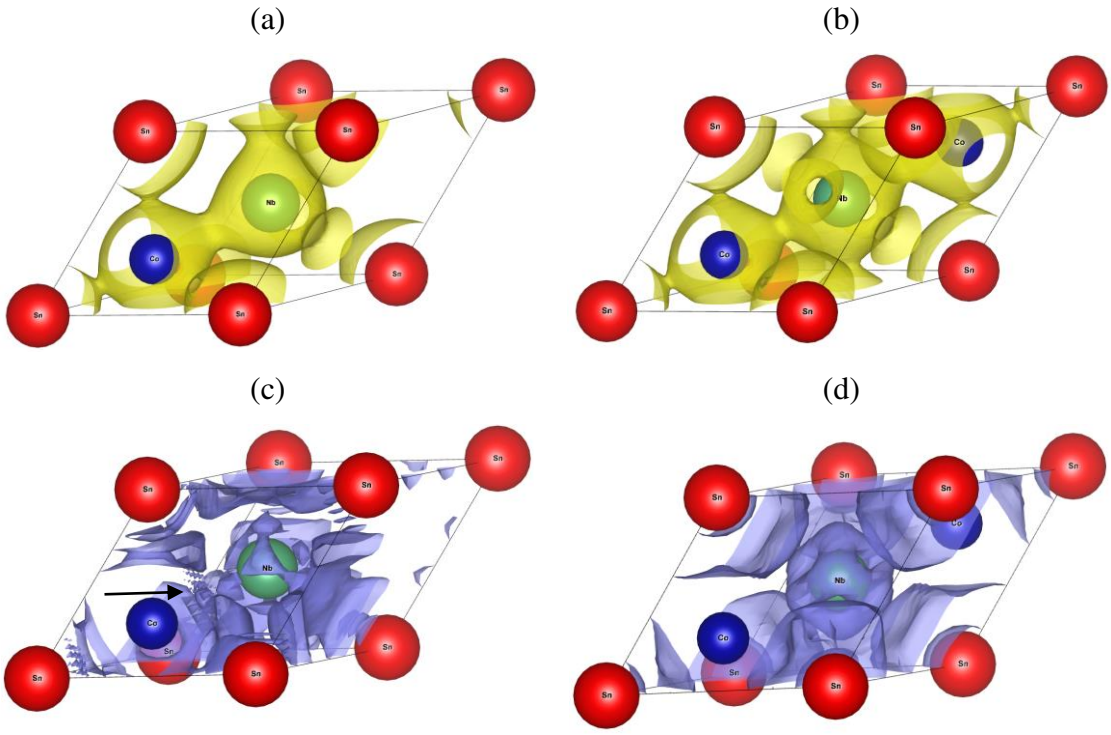

Figure 4.20. Charge density of a) HH-A niobium with isosurface: 0.057 eÅ^{-3}, b) FH-A niobium with isosurface: 0.044 eÅ^{-3}; and Electron localization function of c) HH-A niobium with isosurface: 0.22, and d) FH-A niobium with isosurface: 0.16.

Figure 4.21 (b) presents the ELF plots on the $(1\bar{2}1)$ and (101) planes of FH-A structure. In the plane $(1\bar{2}1)$, the presence of Co in the 8c site in addition to the 4c site, induced a smaller electronic localization around them, when compared to the HH-A structure. This result is corroborated by the values presented for the Bader charge equal to -0.49 |e| per Co atom at sites 4c and 8c, while for Nb atom is equal to +1.07 |e|. Thus, it is observed that a covalent-polar bond remains in the Sn-Co-Nb direction, with a decrease in polarization. As shown in Figure 4.6 (c), PDOS indicated that the bond occurs mainly by Co(d)-Nb(d) orbitals hybridization, with a reduced contribution from Sn(p) orbitals. In the (101) plane, it is observed that in the vicinity of Sn the ELF assumes higher values, where bonds occur in the Sn-Nb direction.

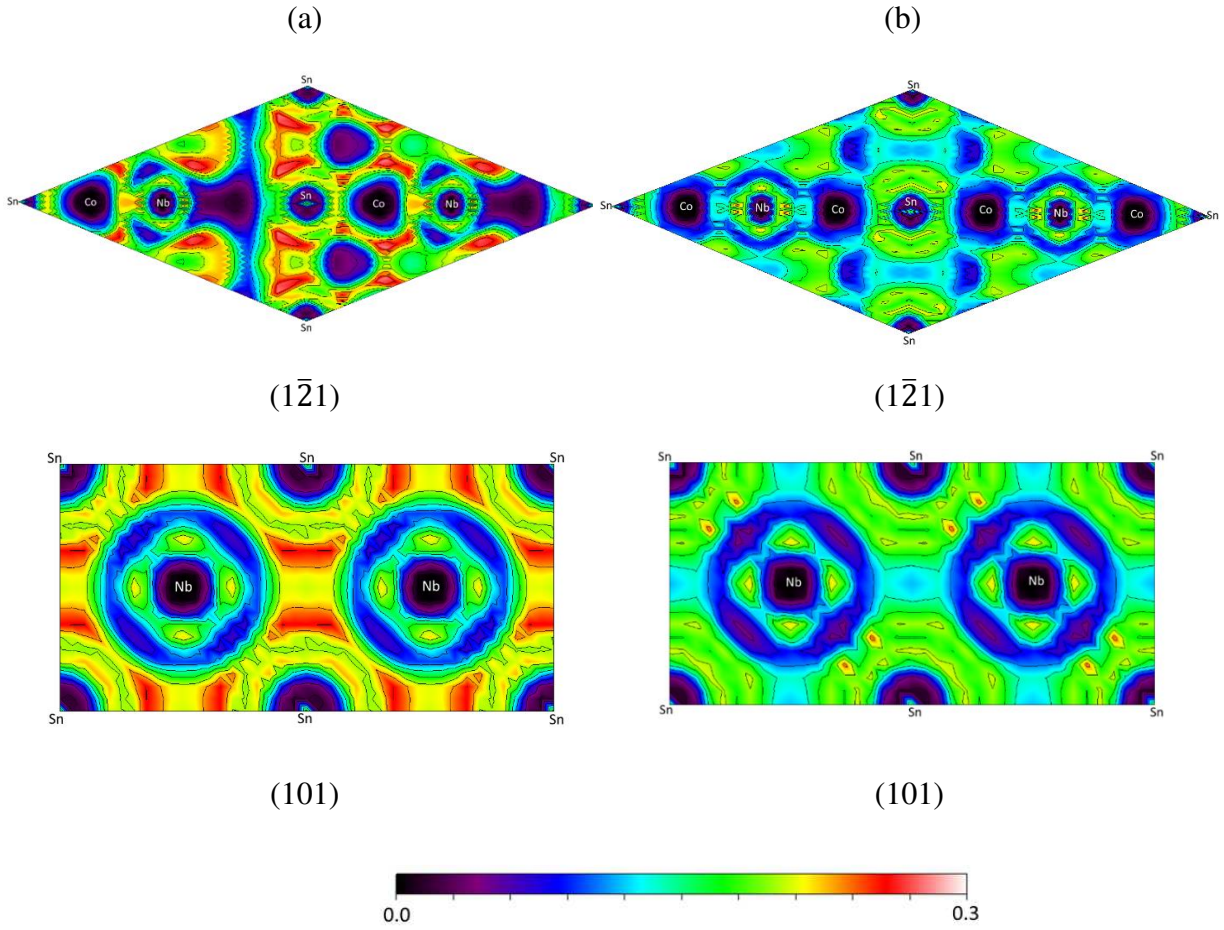

Figure 4.21. Electron localization function obtained from HSE06 calculations in the planes (1$\bar{2}$1) and (101) for a) HH-A and b) FH-A niobium structures.

4.4.3 Tantalum alloys

The Bader charges were calculated for Tantalum structures, as presented in Table 4.13. For HH structures, Co assumes a negative charge and Ta a positive charge, while Sn presents a more significant negative charge in HH-B. Analogous to vanadium and niobium alloys, polarization is observed in the directions Co(4c)-Ta(4a/4b), Sn(4c)-Ta(4a/4b), Ta(4c)-Sn(4a/4b), respectively, for HH-A, HH-B and HH-C structures. So, it was observed that the type of atom located in the 4c/8c position is crucial for the formation of the covalent-polar character of the chemical bonds in the HH crystals. Thus, it was verified that the HH-A structure has covalent-polar bonds in the Co(4c)–Ta(4a/4b) directions, as well as the HH-B and HH-C structures, respectively, in the Sn(4c)–Ta(4a/4b) and Ta(4c)–Sn (4a/4b) directions. As shown in Table 4.13, an analogous result was found for FH structures, although the two atoms located in the respective 4c and 8c sites have the charge reduced as compared with HH structures.

Additionally, it was verified that SOC effect does not change the Bader charges and, therefore, the nature of the chemical bonds.

Table 4.13 – Bader Charge q (|e|) obtained from HSE06 calculations. Values in bold represent the atoms in the 4c/8c sites.

Crystal	Atom	Structure		
		A	**B**	**C**
HH	**Co**	**-1.19**	-0.05	-0.11
	Sn	0.02	**-0.76**	-0.51
	Ta	1.17	0.81	**0.62**
FH	**Co**	**-0.57**[a]	0.03	-0.30
	Sn	0.06	**-0.17** [a]	-0.42
	Ta	1.08	0.31	**0.36**[a]

[a]Bader charge per atom in the 4c and 8c sites.

Figures 4.22 (a) and (b) show the charge density for HH-A and FH-A structures, respectively, where the results are very similar to the niobium case. There is greater charge density in the Co-Ta direction than in the Co-Sn direction for both HH-A and FH-A tantalum alloys. On the other hand, Figure 4.22 (c) shows an ELF attractor located between the Co and Ta atoms (indicated by arrow), confirm the covalent-polar bond Co-Ta in the HH-A structure. For FH-A structure, Figure 4.22 (d) indicates an absence of attractor in Co-V direction, while higher ELF values are present in Sn-Nb directions. This can be explained by greater electronegativity of Sn and the net charge of cobalt in the FH-A structure (-0.57 |e|) being much lower than of cobalt in the HH-A structure (-1.19 |e|), as shown in Table 4.13.

Figure 4.23 (a) shows the ELF plots on the $(1\bar{2}1)$ and (101) planes of HH-A structure. For $(1\bar{2}1)$ plane, ELF presents larger values in-between the Sn-Co-Ta direction, approximately in the middle of the bond axis. On the other hand, from Bader analysis, it was obtained a charge equal to -1.19 |e| for Co, equal to +1.17 |e| for Ta and almost zero for Sn. Furthermore, the ELF is asymmetric around Co, i. e., displaced to one side of its nucleus. Thus, a covalent-polar bond is observed in the Sn-Co-Ta direction. As previously discussed, in Figure 4.9 (c), PDOS indicated that the bond occurs mainly by Sn(p)-Co(d)-Ta(d) orbitals hybridization. In the (101) plane, it is observed that in the vicinity of Sn the ELF assumes higher values, where bonds occur in the Sn-Ta direction.

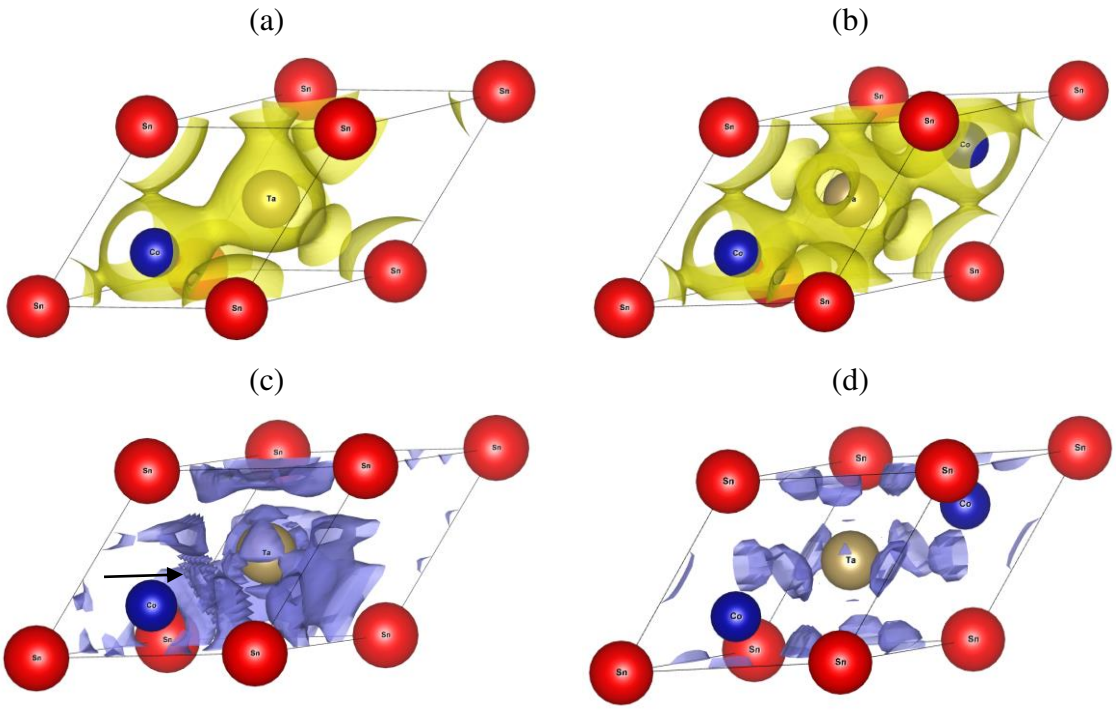

Figure 4.22. Charge density of a) HH-A tantalum with isosurface: 0.052 eÅ^{-3}, b) FH-A tantalum with isosurface: 0.045 eÅ^{-3}; and Electron localization function of c) HH-A tantalum with isosurface: 0.23, and d) FH-A tantalum with isosurface: 0.28.

Figure 4.23 (b) presents the ELF plots on the $(1\bar{2}1)$ and (101) planes of FH-A structure. In the plane $(1\bar{2}1)$, the presence of Co in the 8c site in addition to the 4c site, induced a smaller electronic localization around them, when compared to the HH-A structure. This result is corroborated by the values presented for the Bader charge equal to -0.57 |e| per Co atom at sites 4c and 8c, while for Ta atom is equal to +1.08 |e|. Thus, it is observed that a covalent-polar bond remains in the Sn-Co-Ta direction, with a decrease in polarization. As shown in Figure 4.6 (c), PDOS indicated that the bond occurs mainly by Co(d)-Ta(d) orbitals hybridization, with a reduced contribution from Sn(p) orbitals. In the (101) plane, it is observed that in the vicinity of Sn the ELF assumes higher values, where bonds occur in the Sn-Ta direction.

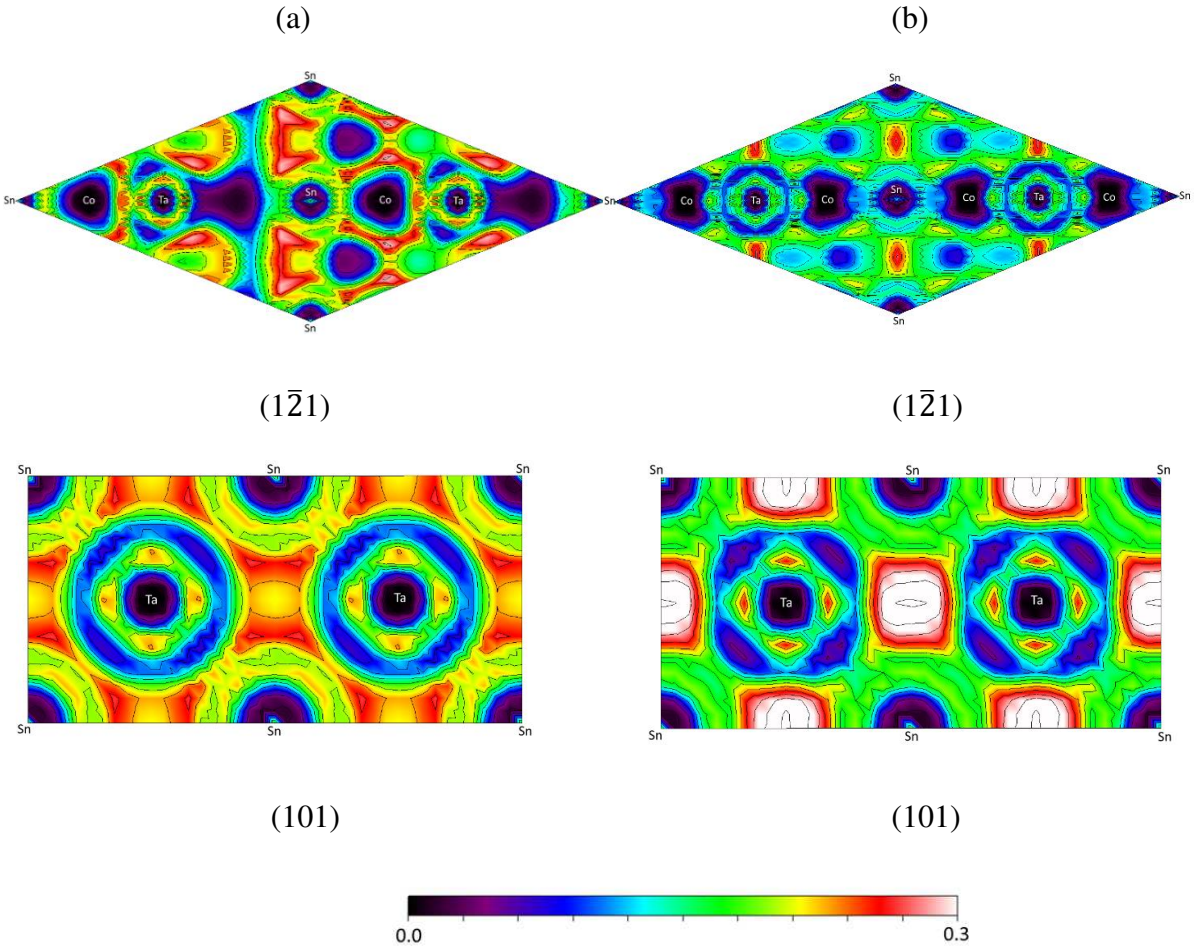

Figure 4.23. Electron localization function obtained from HSE06 calculations in the planes (1$\bar{2}$1) and (101) for a) HH-A and b) FH-A tantalum structures.

4.5 Thermoelectric Properties

In this section is presented the analyses of thermoelectric properties of tantalum HH-A alloy. The theorical results were compared with the experimental work of Li, S. & et al [62]. The MLWF functions were used to interpolate the band structure obtained previously from GGA-PBE approximation, as shown in Figure 4.24. Then, a post-processing calculation was carried out to obtain the thermoelectric quantities. The Seebeck coefficient S, electrical conductivity σ, and electronic component of thermal conductivity κ_e were obtained within rigid band approximation, where the chemical potential (μ) and the relaxation time (τ) were used to fit the extracted experimental data.

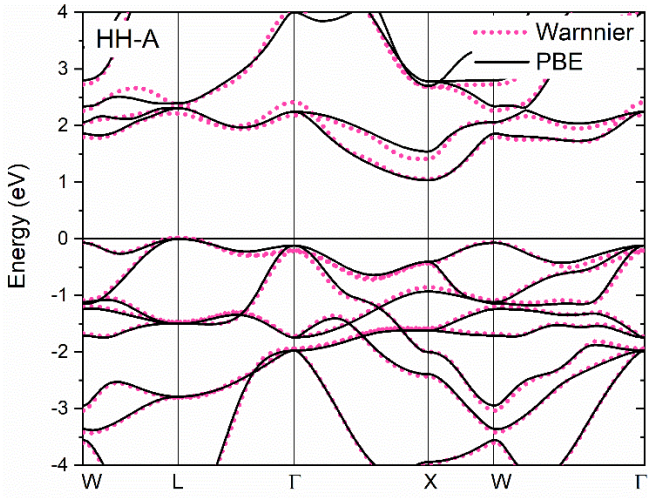

Figure 4.24. Calculated bandstructures obtained from Wannier functions (dashed lines) and GGA-PBE calculations (solid lines) Tantalum HH-A structure.

Figure 4.25 presents extracted experimental data [62] and theorical curves, considering $\tau = 0.16$ fs and $E_f - \mu = 1.2634$ eV, where E_f is the Fermi level. As shown in Figure 4.25 (a), the theoretical coefficient curve does not completely fit the experimental data, although a similar trend is observed. Figure 4.25 (b) presents the electrical conductivity, where for the range $450 < T < 800$ a reasonable agreement is observed. Figure 4.25 (c) shows that the contribution of electronic component to the thermal conductivity is significant at low temperatures ($T < 500$ K). On the other hand, κ_e has been overestimated for $T > 500$ K. It is expected that for $T > 500$ K phonons has an important contribution to the thermal conductivity. In addition, three curve fits were performed for ZT, as shown in Figure 4.25 (d). When only κ_e is considered, it is observed that ZT increases with temperature, although the values are overestimated in comparison with the experimental data. This result supports that contribution to the lattice is important for a broad description of the thermal conductivity in these materials. For $T < 700$ K, a suitable fit occurs when only the lattice component of the thermal conductivity κ_{lat} is taken into account, but underestimated for $T > 700$ K. The lattice component was obtained by Shan Li et al. [62], considering $\kappa_{lat} = \kappa - \kappa_e$, where κ_e was calculated via Wiedemann–Franz law within single parabolic band model. Thus, it is highlighted that the thermal conductivity plays an important role in Tantalum HH-A alloy and that the handling of the scattering process is very important to improve their thermoelectric properties. Therefore, the investigation of phonon scattering mechanisms as well as the electron–phonon coupling [143] can contribute to improve the calculation of the thermoelectric properties of the HH materials.

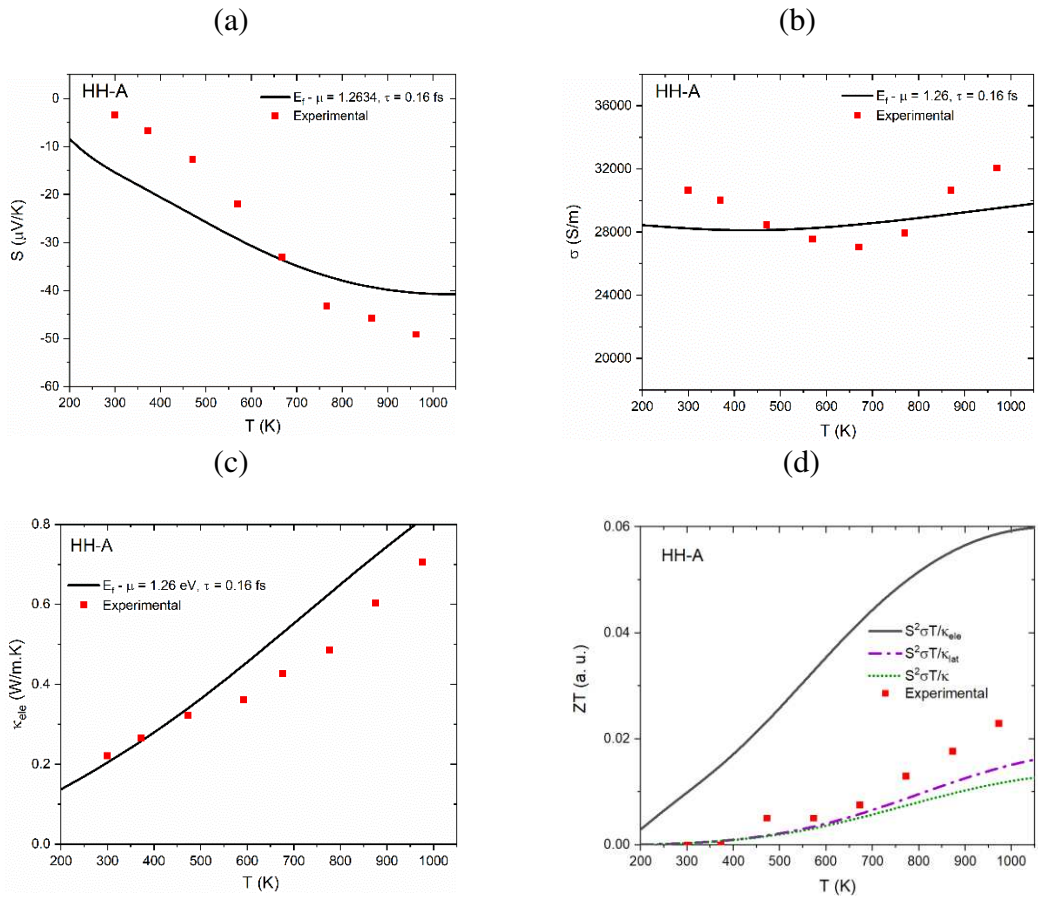

Figure 4.25. Theoretical and experimental results for (a) Seebeck coefficient, (b) electrical conductivity (c) electronic component of thermal conductivity and (d) ZT versus temperature in the range of temperature 200 –1050K for HH-A tantalum structure. Experimental data extracted from Ref. Shan Li, et al [62].

Figure 4.26 presents the theoretical results for Seebeck coefficient, electrical conductivity and power factor versus chemical potential for a temperature range 300–900 K. The TE quantities had been obtained for different carrier concentrations by varying the chemical potential. The values of μ were defined from the bandstructure calculations around the Fermi Level. As seen in Figure 4.26 (a), close to E_F, the Seebeck coefficient shows a downward trend as the temperature increases. Maximum values of S occur at -0.06 eV (n-type) and 0.05 eV (p-type), in agreement with result obtained previously [144]. As observed in Fig. 4.26 (b), electrical conductivity increases when a substantial carrier concentration is considered, i.e., for E_F- μ < -0.5 (n-type) and Ef - μ > 0.5 (p-type), although the Seebeck coefficient decreases under these conditions. For E_F - μ > - 1.0 eV and E_F - μ < 0.7 eV, electrical

conductivity increases as temperature increases, whereas for highest carrier concentrations (E_F - μ = 0.90 eV and -1.25 eV) the electrical conductivity decreases as temperature increases.

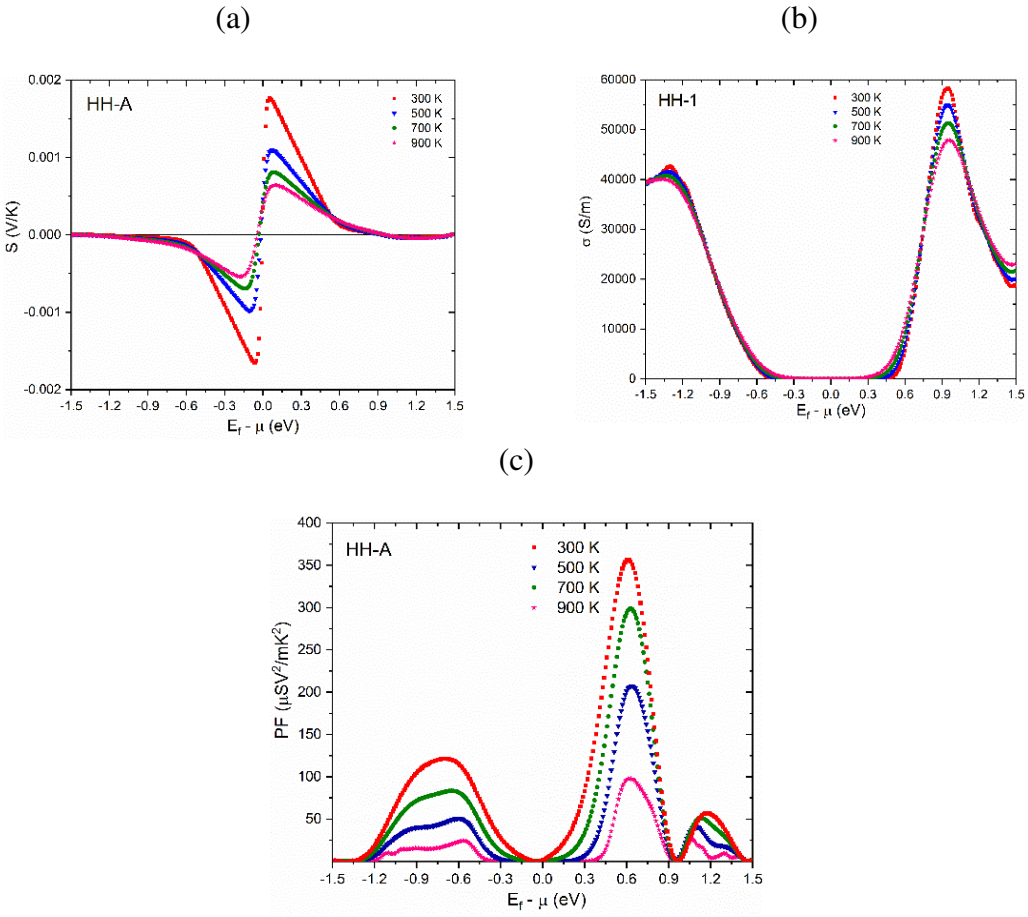

Figure 4.26. Calculated (a) Seebeck coefficient, (b) electrical conductivity and (c) power factor for in HH-A structure, as a function of the chemical potentials for different temperatures.

It was observed that power factor reaches higher values for lower temperatures and higher carrier concentrations. As shown in Fig. 4.26 (c), uppermost value (≈ 360 $\mu SV^2/mK^2$) occurs at E_F - μ ≈ +0.63 eV (p-type) at room temperature, although a smaller peak is observed in E_F - μ ≈ +1.2 eV. On the other side, a relevant peak at Ef - μ ≈ - 0.75 eV (n-type) is observed, where PF ≈ 125 $\mu SV^2/mK^2$ at T = 300 K. With these results, the doping process is a good way to improve of the TE properties of HH-A tantalum alloys. This process can increase carrier concentration, which increase the PF and can be a way of decrease the thermal conductivity. As shown by S. Li et al [62], ZT = 0.75 (T = 973K) in Sb-doping Co(Ta/Nb)Sn alloy ($Ta_{0.6}Nb_{0.4}CoSn_{0.94}Sb_{0.06}$). Also, as previously reported [142], thermoelectric properties were improved by the combination of Ta and V in this $CoTa_{0.5}V_{0.5}Sn$ structure.

5 – CONCLUSION

Within the perspective of development of new technologies environment friendly to generation of energy, this work analyzed Heusler structure Co-VB-Sn with focus in application as thermoelectric. The calculations showed that the HH alloys have a more stable structure when the Co atom occupies the 4c position (structure HH-A). For the FH alloy this occurs when the Ta atom occupies this position and its equivalent 8d (structure FH-C), although in the literature there are only experimental records of FH alloys with the Co atom occupying the 4c/8c position (structure FH-A). In both GGA-PBE and HSE06 approximations, HH-A structures present semiconductor behavior, that is fundamental to thermoelectric applications. On the other hand, FH-A present half-metallic behavior, which is interesting for application in other areas as spintronic. In addition, when HSE06 is considered, the structures HH-A and FH-A presented magnetization in accordance with Slater-Pauling rule. In general, GGA-PBE approximation describe satisfactorily the structural properties of Heusler alloys. From chemical bond analyses, the 4c/8c sites play an important role to definition of covalent-polar bonds in the HH-A and FH-A structures. In addition, structure HH-A Co-VB-Sn presented relative high DOS effective mass, which is fundamental for the thermoelectric properties. In terms of effective masses, SOC effect plays an important role. For HH-A tantalum alloy, it was observed that the contribution of electronic component to the thermal conductivity is significant for low temperatures ($T < 500$ K). On the other hand, for high temperatures the contribution of phonons must be taken into account, emphasizing the need for further studies. Finally, with these results stay evident the potential of Co-VB-Sn as thermoelectric. Finally, this work presented an important perspective of analyses how to improve thermoelectric properties from the controlled formation these structures. Finally, the process of doping is other possibility to improve this material as thermoelectric, and will be focus of study in future works, as well the study of FH-A to others applications.

6 – REFERENCES

[1] H. Ritchie, P. Rosado, Energy: Key Charts - Our World in Data, (2021). https://ourworldindata.org/energy-key-charts (accessed September 17, 2023).

[2] J. Evans, L.C. Hunt, eds., International Handbook on the Economics of Energy, 1st ed., Edward Elgar Publishing, Northampton, 2009. https://doi.org/10.4337/9781849801997.

[3] E. Panos, M. Densing, K. Volkart, Access to electricity in the World Energy Council's global energy scenarios: An outlook for developing regions until 2030, Energy Strategy Reviews. 9 (2016) 28–49. https://doi.org/10.1016/J.ESR.2015.11.003.

[4] M. Kanagawa, T. Nakata, Assessment of access to electricity and the socio-economic impacts in rural areas of developing countries, Energy Policy. 36 (2008) 2016–2029. https://doi.org/10.1016/J.ENPOL.2008.01.041.

[5] UNFCCC, Paris Agreement, Paris, 2015.

[6] C. Forman, I.K. Muritala, R. Pardemann, B. Meyer, Estimating the global waste heat potential, Renewable and Sustainable Energy Reviews. 57 (2016) 1568–1579. https://doi.org/10.1016/j.rser.2015.12.192.

[7] B. Sanchez, U.S. Energy Information Administration - EIA - Independent Statistics and Analysis, (2020). https://www.eia.gov/todayinenergy/detail.php?id=44436 (accessed May 1, 2023).

[8] J. Krane, Climate change and fossil fuel: An examination of risks for the energy industry and producer states, MRS Energy and Sustainability. 4 (2017) 1–12. https://doi.org/10.1557/MRE.2017.3/METRICS.

[9] R.R. Judkins, W. Fulkerson, M.K. Sanghvi, The Dilemma of Fossil Fuel Use and Global Climate Change, Energy and Fuels. 7 (1993) 14–22. https://doi.org/10.1021/EF00037A004/ASSET/EF00037A004.FP.PNG_V03.

[10] S. Bilgen, Structure and environmental impact of global energy consumption, Renewable and Sustainable Energy Reviews. 38 (2014) 890–902. https://doi.org/10.1016/J.RSER.2014.07.004.

[11] K. Bos, J. Gupta, Climate change: the risks of stranded fossil fuel assets and resources to the developing world, Third World Q. 39 (2018) 436–453. https://doi.org/10.1080/01436597.2017.1387477.

[12] A.M. Omer, Green energies and the environment, Renewable and Sustainable Energy Reviews. 12 (2008) 1789–1821. https://doi.org/10.1016/J.RSER.2006.05.009.

[13] M.M. Mohideen, S. Ramakrishna, S. Prabu, Y. Liu, Advancing green energy solution with the impetus of COVID-19 pandemic, Journal of Energy Chemistry. 59 (2021) 688–705. https://doi.org/10.1016/J.JECHEM.2020.12.005.

[14] A. Markandya, I. Arto, M. González-Eguino, M. V. Román, Towards a green energy economy? Tracking the employment effects of low-carbon technologies in the European Union, Appl Energy. 179 (2016) 1342–1350. https://doi.org/10.1016/J.APENERGY.2016.02.122.

[15] L. Mundaca, J. Luth Richter, Assessing 'green energy economy' stimulus packages: Evidence from the U.S. programs targeting renewable energy, Renewable and Sustainable Energy Reviews. 42 (2015) 1174–1186. https://doi.org/10.1016/J.RSER.2014.10.060.

[16] T.J. Seebeck, Ueber die magnetische Polarisation der Metalle und Erze durch Temperatur-Differenz, Ann Phys. 82 (1826) 133–160. https://doi.org/10.1002/ANDP.18260820202.

[17] T.J. Seebeck, Über den Magnetismus der galvanischen Kette, Abhadlungen Der Physikalischen Klasse Der Königlisch-Preußsischen. Akademie Der Wissenschaftten Aus Den Jahren 1820-1821: 289–346. (1822).

[18] J.C.A. Peltier, Nouvelles Experiences sur la Caloricite des Courans Electriques, Annales de Chimie et de Physique. LVl 371 (1834) 371–386.

[19] W. Thomson, On a mechanical theory of thermoelectric currents, Proceedings of the Royal Society of Edinburgh. 91 (1851).

[20] D. Rowe, Thermoelectrics handbook: macro to nano, 1st ed., CRC Press, New York, 1995.

[21] X.L. Shi, J. Zou, Z.G. Chen, Advanced thermoelectric design: From materials and structures to devices, Chem Rev. 120 (2020) 7399–7515. https://doi.org/10.1021/ACS.CHEMREV.0C00026.

[22] S. Bhattacharya, M.J. Skove, M. Russell, T.M. Tritt, Y. Xia, V. Ponnambalam, S.J. Poon, N. Thadhani, Effect of boundary scattering on the thermal conductivity of TiNiSn-based half-Heusler alloys, Phys Rev B Condens Matter Mater Phys. 77 (2008) 184203. https://doi.org/10.1103/PHYSREVB.77.184203.

[23] X. Zhang, L.D. Zhao, Thermoelectric materials: Energy conversion between heat and electricity, Journal of Materiomics. 1 (2015) 92–105. https://doi.org/10.1016/J.JMAT.2015.01.001.

[24] J. Fairbanks, THERMOELECTRIC APPLICATIONS IN VEHICLES STATUS 2008, Washington, 2008.

[25] H. Mamur, M.R.A. Bhuiyan, F. Korkmaz, M. Nil, A review on bismuth telluride (Bi2Te3) nanostructure for thermoelectric applications, Renewable and Sustainable Energy Reviews. 82 (2018) 4159–4169. https://doi.org/10.1016/j.rser.2017.10.112.

[26] C. Candolfi, S. El Oualid, D. Ibrahim, S. Misra, O. El Hamouli, A. Léon, A. Dauscher, P. Masschelein, P. Gall, P. Gougeon, C. Semprimoschnig, B. Lenoir, Thermoelectric

materials for space applications, CEAS Space Journal 13 (2021) 325–340. https://doi.org/10.1007/S12567-021-00351-X.

[27] L.E. Bell, Cooling, Heating, Generating Power, and Recovering Waste Heat with Thermoelectric Systems, Science. 321 (2008) 1457–1461. https://doi.org/10.1126/SCIENCE.1158899.

[28] M. Beekman, D.T. Morelli, G.S. Nolas, Better thermoelectrics through glass-like crystals, Nature Materials 201. 14 (2015) 1182–1185. https://doi.org/10.1038/nmat4461.

[29] K. Zhao, P. Qiu, X. Shi, L. Chen, Recent Advances in Liquid-Like Thermoelectric Materials, Adv Funct Mater. 30 (2020) 1903867. https://doi.org/10.1002/ADFM.201903867.

[30] Y. Zhou, L.D. Zhao, Promising Thermoelectric Bulk Materials with 2D Structures, Advanced Materials. 29 (2017) 1702676. https://doi.org/10.1002/ADMA.201702676.

[31] X. Liang, D.R. Clarke, Single layer In-O atomic sheets as phonon and electron barriers in ZnO-In2O3 natural superlattices: Implications for thermoelectricity, Citation: Journal of Applied Physics. 124 (2018) 25101. https://doi.org/10.1063/1.5027625.

[32] A. Bulusu, D.G. Walker, Review of electronic transport models for thermoelectric materials, Superlattices Microstruct. 44 (2008) 1–36. https://doi.org/10.1016/J.SPMI.2008.02.008.

[33] N. Toshima, Recent progress of organic and hybrid thermoelectric materials, Synth Met. 225 (2017) 3–21. https://doi.org/10.1016/j.synthmet.2016.12.017.

[34] B. Russ, A. Glaudell, J.J. Urban, M.L. Chabinyc, R.A. Segalman, Organic thermoelectric materials for energy harvesting and temperature control, Nature Reviews Materials. 1 (2016) 1–14. https://doi.org/10.1038/natrevmats.2016.50.

[35] K. Kurosaki, S. Yamanaka, Low-thermal-conductivity group 13 chalcogenides as high-efficiency thermoelectric materials, Physica Status Solidi (a). 210 (2013) 82–88. https://doi.org/10.1002/PSSA.201228680.

[36] G. Rogl, A. Grytsiv, M. Gürth, A. Tavassoli, C. Ebner, A. Wünschek, S. Puchegger, V. Soprunyuk, W. Schranz, E. Bauer, H. Müller, M. Zehetbauer, P. Rogl, Mechanical properties of half-Heusler alloys, Acta Mater. 107 (2016) 178–195. https://doi.org/10.1016/j.actamat.2016.01.031.

[37] K. Tolborg, B.B. Iversen, Chemical bonding origin of the thermoelectric power factor in Half-Heusler semiconductors, Chemistry of Materials. 33 (2021) 5308–5316. https://doi.org/10.1021/acs.chemmater.1c01409.

[38] J.K. Kawasaki, S. Chatterjee, P.C. Canfield, Full and half-Heusler compounds, MRS Bull. 47 (2022) 555–558. https://doi.org/10.1557/S43577-022-00355-W/FIGURES/1.

[39] K. Elphick, W. Frost, M. Samiepour, T. Kubota, K. Takanashi, H. Sukegawa, S. Mitani, A. Hirohata, Heusler alloys for spintronic devices: review on recent development and future perspectives, Sci Technol Adv Mater. 22 (2021) 271. https://doi.org/10.1080/14686996.2020.1812364.

[40] M. Sofronie, F. Tolea, A.D. Crisan, B. Popescu, M. Valeanu, Magnetoelastic properties in polycrystalline ferromagnetic shape memory Heusler alloys, Procedia Structural Integrity. 2 (2016) 1530–1537. https://doi.org/10.1016/J.PROSTR.2016.06.194.

[41] B. Yan, A. de Visser, Half-Heusler topological insulators, MRS Bull. 39 (2014) 859–866. https://doi.org/10.1557/mrs.2014.198.

[42] G.H. Yu, Y.L. Xu, Z.H. Liu, H.M. Qiu, Z.Y. Zhu, X.P. Huang, L.Q. Pan, Recent progress in Heusler-type magnetic shape memory alloys, Rare Metals. 34 (2015) 527–539. https://doi.org/10.1007/S12598-015-0534-1.

[43] Y. Xing, R. Liu, J. Liao, Q. Zhang, X. Xia, C. Wang, H. Huang, J. Chu, M. Gu, T. Zhu, C. Zhu, F. Xu, D. Yao, Y. Zeng, S. Bai, C. Uher, L. Chen, High-efficiency half-Heusler thermoelectric modules enabled by self-propagating synthesis and topologic structure optimization, Energy Environ Sci. 12 (2019) 3390–3399. https://doi.org/10.1039/c9ee02228g.

[44] S. Sakurada, N. Shutoh, Effect of Ti substitution on the thermoelectric properties of (Zr,Hf)NiSn half-Heusler compounds, Appl Phys Lett. 86 (2005) 1–3. https://doi.org/10.1063/1.1868063/328806.

[45] M. Schwall, B. Balke, Phase separation as a key to a thermoelectric high efficiency, Physical Chemistry Chemical Physics. 15 (2013) 1868–1872. https://doi.org/10.1039/C2CP43946H.

[46] C. Fu, T. Zhu, Y. Liu, H. Xie, X. Zhao, Band engineering of high-performance p-type FeNbSb based half-Heusler thermoelectric materials for figure of merit zT > 1, Energy Environ Sci. 8 (2014) 216–220. https://doi.org/10.1039/C4EE03042G.

[47] T. Zhu, C. Fu, H. Xie, Y. Liu, X. Zhao, High Efficiency Half-Heusler Thermoelectric Materials for Energy Harvesting, Adv Energy Mater. 5 (2015) 1500588. https://doi.org/10.1002/AENM.201500588.

[48] J.W.G. Bos, R.A. Downie, Half-Heusler thermoelectrics: a complex class of materials, Journal of Physics: Condensed Matter. 26 (2014) 433201. https://doi.org/10.1088/0953-8984/26/43/433201.

[49] R.J. Quinn, J.W.G. Bos, Advances in half-Heusler alloys for thermoelectric power generation, Mater Adv. 2 (2021) 6246–6266. https://doi.org/10.1039/D1MA00707F.

[50] S.H. Zaferani, A. Darebaghi, S.J. Hong, D. Vashaee, R. Ghomashchi, Experimental Realization of Heavily p-doped Half-Heusler CoVSn Compound, Energies 2020. 13 (2020) 1459. https://doi.org/10.3390/EN13061459.

[51] Y. Ono, S. Inayama, H. Adachi, T. Kajitani, Thermoelectric properties of NbCoSn-based half-Heusler alloys, International Conference on Thermoelectrics, ICT, Proceedings. (2006) 124–127. https://doi.org/10.1109/ICT.2006.331296.

[52] Y. Kimura, Y. Tamura, T. Kita, Thermoelectric properties of directionally solidified half-Heusler compound NbCoSn alloys, Appl Phys Lett. 92 (2008). https://doi.org/10.1063/1.2828713.

[53] D.A. Ferluccio, R.I. Smith, J. Buckman, J.W.G. Bos, Impact of Nb vacancies and p-type doping of the NbCoSn-NbCoSb half-Heusler thermoelectrics, Physical Chemistry Chemical Physics. 20 (2018) 3979–3987. https://doi.org/10.1039/c7cp07521a.

[54] M.L.C. Buffon, G. Laurita, N. Verma, L. Lamontagne, L. Ghadbeigi, D.L. Lloyd, T.D. Sparks, T.M. Pollock, R. Seshadri, Enhancement of thermoelectric properties in the Nb-Co-Sn half-Heusler/Heusler system through spontaneous inclusion of a coherent second phase, J Appl Phys. 120 (2016). https://doi.org/10.1063/1.4961215.

[55] R. He, L. Huang, Y. Wang, G. Samsonidze, B. Kozinsky, Q. Zhang, Z. Ren, Enhanced thermoelectric properties of n-type NbCoSn half-Heusler by improving phase purity, APL Mater. 4 (2016). https://doi.org/10.1063/1.4952994.

[56] Y. Kawaharada, K. Kurosaki, H. Muta, M. Uno, S. Yamanaka, High temperature thermoelectric properties of CoNb1-xHf xSn1-ySby half-Heusler compounds, J Alloys Compd. 377 (2004) 312–315. https://doi.org/10.1016/j.jallcom.2004.02.017.

[57] Y. Kawaharada, K. Kurosaki, H. Muta, M. Uno, S. Yamanaka, High temperature thermoelectric properties of CoNb1-xMxSn half-Heusler compounds, J Alloys Compd. 384 (2004) 303–307. https://doi.org/10.1016/j.jallcom.2004.04.095.

[58] R. Yan, W. Xie, B. Balke, G. Chen, A. Weidenkaff, Realizing p-type NbCoSn half-Heusler compounds with enhanced thermoelectric performance via Sc substitution, Sci Technol Adv Mater. 21 (2020) 122–130. https://doi.org/10.1080/14686996.2020.1726715.

[59] R. Yan, R. Xie, W. Xie, C. Shen, W. Li, B. Balke, S. Yoon, H. Zhang, A. Weidenkaff, Effects of Doping Ni on the Microstructures and Thermoelectric Properties of Co-

Excessive NbCoSn Half-Heusler Compounds, ACS Appl Mater Interfaces. 13 (2021) 34533–34542. https://doi.org/10.1021/acsami.1c08127.

[60] F. Serrano-Sánchez, T. Luo, J. Yu, W. Xie, C. Le, G. Auffermann, A. Weidenkaff, T. Zhu, X. Zhao, J.A. Alonso, B. Gault, C. Felser, C. Fu, Thermoelectric properties of n-type half-Heusler NbCoSn with heavy-element Pt substitution, J Mater Chem A Mater. 8 (2020) 14822–14828. https://doi.org/10.1039/d0ta04644b.

[61] A. Zakutayev, X. Zhang, A. Nagaraja, L. Yu, S. Lany, T.O. Mason, D.S. Ginley, A. Zunger, Theoretical prediction and experimental realization of new stable inorganic materials using Inverse Design approach, 2013. http://pubs.acs.org.

[62] S. Li, H. Zhu, J. Mao, Z. Feng, X. Li, C. Chen, F. Cao, X. Liu, D.J. Singh, Z. Ren, Q. Zhang, N-Type TaCoSn-Based Half-Heuslers as Promising Thermoelectric Materials, ACS Appl Mater Interfaces. 11 (2019) 41321–41329. https://doi.org/10.1021/acsami.9b13603.

[63] R.M. Martin, Electronic Structure: Basic Theory and Practical Methods, (2004). https://doi.org/10.1017/CBO9780511805769.

[64] I.N. Levine, Quantum chemistry, 7th ed., Pearson, Nova Jersey, 2013.

[65] R.O. Jones, Density functional theory: Its origins, rise to prominence, and future, Rev Mod Phys. 87 (2015) 897. https://doi.org/10.1103/REVMODPHYS.87.897/.

[66] P. Hohenberg, W. Kohn, Inhomogeneous electron gas, Physical Review. 136 (1964) B864. https://doi.org/10.1103/PHYSREV.136.B864/.

[67] R.G. Parr, W. Yang, Density-Functional Theory of Atoms and Molecules, Oxford University Press, Nova York, 1995. https://doi.org/10.1093/OSO/9780195092769.001.0001.

[68] W. Kohn, L.J. Sham, Self-consistent equations including exchange and correlation effects, Physical Review. 140 (1965) A1133. https://doi.org/10.1103/PHYSREV.140.A1133/.

[69] J.P. Perdew, W. Yue, Accurate and simple density functional for the electronic exchange energy: Generalized gradient approximation, Phys Rev B. 33 (1986) 8800. https://doi.org/10.1103/PhysRevB.33.8800.

[70] J.P. Perdew, K. Burke, M. Ernzerhof, Generalized Gradient Approximation Made Simple, Phys Rev Lett. 78 (1996) 1396. https://doi.org/10.1103/PhysRevLett.78.1396.

[71] F. Tran, P. Blaha, Accurate band gaps of semiconductors and insulators with a semilocal exchange-correlation potential, Phys Rev Lett. 102 (2009) 226401. https://doi.org/10.1103/PHYSREVLETT.102.226401/.

[72] A.D. Becke, M.R. Roussel, Exchange holes in inhomogeneous systems: A coordinate-space model, Phys Rev A. 39 (1989) 3761. https://doi.org/10.1103/PhysRevA.39.3761.

[73] J. Heyd, G.E. Scuseria, M. Ernzerhof, Hybrid functionals based on a screened Coulomb potential, J Chem Phys. 118 (2003) 8207–8215. https://doi.org/10.1063/1.1564060.

[74] A. V. Krukau, O.A. Vydrov, A.F. Izmaylov, G.E. Scuseria, Influence of the exchange screening parameter on the performance of screened hybrid functionals, Journal of Chemical Physics. 125 (2006) 224106. https://doi.org/10.1063/1.2404663/953719.

[75] P.E. Blöchl, Projector augmented-wave method, Phys Rev B. 50 (1994) 17953. https://doi.org/10.1103/PhysRevB.50.17953.

[76] G. Kresse, D. Joubert, From ultrasoft pseudopotentials to the projector augmented-wave method, Phys Rev B. 59 (1999) 1758. https://doi.org/10.1103/PhysRevB.59.1758.

[77] N.W. Ashcroft, N.David. Mermin, Solid state physics, Saunders College Publishing, New York, 1976.

[78] F. Bloch, Über die Quantenmechanik der Elektronen in Kristallgittern, Zeitschrift Für Physik. 52 (1929) 555–600. https://doi.org/10.1007/BF01339455.

[79] H.J. Monkhorst, J.D. Pack, Special points for Brillouin-zone integrations, Phys Rev B. 13 (1976) 5188. https://doi.org/10.1103/PhysRevB.13.5188.

[80] M.I. Aroyo, D. Orobengoa, G. De La Flor, E.S. Tasci, J.M. Perez-Mato, H. Wondratschek, Brillouin-zone database on the Bilbao Crystallographic Server, Acta Crystallographica Section A. 70 (2014) 126–137. https://doi.org/10.1107/S205327331303091X.

[81] G. Kresse, J. Furthmüller, Efficiency of ab-initio total energy calculations for metals and semiconductors using a plane-wave basis set, Comput Mater Sci. 6 (1996) 15–50. https://doi.org/10.1016/0927-0256(96)00008-0.

[82] G. Kresse, J. Furthmüller, Efficient iterative schemes for *ab initio* total-energy calculations using a plane-wave basis set, Phys Rev B. 54 (1996) 11169. https://doi.org/10.1103/PhysRevB.54.11169.

[83] G. Kresse, D. Joubert, From ultrasoft pseudopotentials to the projector augmented-wave method, Phys Rev B. 59 (1999) 1758. https://doi.org/10.1103/PhysRevB.59.1758.

[84] G. Kresse, J. Furthmuller, VASP the GUIDE, Institut fur Materialphysik, Universitat Wien, Sensengasse 8, A-1130 Wien, Austria, 2007.

[85] G.H. Wannier, Dynamics of Band Electrons in Electric and Magnetic Fields, Rev Mod Phys. 34 (1962) 645–655. https://doi.org/10.1103/REVMODPHYS.34.645.

[86] G.H. Wannier, The Structure of Electronic Excitation Levels in Insulating Crystals, Physical Review. 52 (1937) 191. https://doi.org/10.1103/PhysRev.52.191.

[87] N. Marzari, A.A. Mostofi, J.R. Yates, I. Souza, D. Vanderbilt, Maximally localized Wannier functions: Theory and applications, Rev Mod Phys. 84 (2012) 1419–1475. https://doi.org/10.1103/REVMODPHYS.84.1419/.

[88] N. Marzari, D. Vanderbilt, Maximally localized generalized Wannier functions for composite energy bands, Phys Rev B. 56 (1997) 12847. https://doi.org/10.1103/PhysRevB.56.12847.

[89] I. Souza, N. Marzari, D. Vanderbilt, Maximally localized Wannier functions for entangled energy bands, Phys Rev B. 65 (2001) 035109. https://doi.org/10.1103/PhysRevB.65.035109.

[90] A.A. Mostofi, J.R. Yates, Y.S. Lee, I. Souza, D. Vanderbilt, N. Marzari, wannier90: A tool for obtaining maximally-localised Wannier functions, Comput Phys Commun. 178 (2008) 685–699. https://doi.org/10.1016/J.CPC.2007.11.016.

[91] G. Pizzi, D. Volja, B. Kozinsky, M. Fornari, N. Marzari, BoltzWann: A code for the evaluation of thermoelectric and electronic transport properties with a maximally-localized Wannier functions basis, Comput Phys Commun. 185 (2014) 422–429. https://doi.org/10.1016/J.CPC.2013.09.015.

[92] P.T. Gressman, R.M. Strain, Global classical solutions of the Boltzmann equation with long-range interactions, PNAS. 107 (2010) 5744–5749. https://doi.org/10.1073/pnas.1001185107.

[93] Y. Takagiwa, Y. Pei, G. Pomrehn, G. Jeffrey Snyder, Validity of rigid band approximation of PbTe thermoelectric materials, APL Mater. 1 (2013) 11101. https://doi.org/10.1063/1.4809545/119671.

[94] A.D. Becke, K.E. Edgecombe, A simple measure of electron localization in atomic and molecular systems, J Chem Phys. 92 (1990) 5397–5403. https://doi.org/10.1063/1.458517.

[95] B. Silvi, A. Savin, Classification of chemical bonds based on topological analysis of electron localization functions, Nature. 371 (1994) 683–686. https://doi.org/10.1038/371683a0.

[96] R.J. Clements, J.C. Womack, C.-K. Skylaris, K. Koumpouras, J.A. Larsson, Distinguishing between chemical bonding and physical binding using electron localization function (ELF), Journal of Physics: Condensed Matter. 32 (2020) 315502. https://doi.org/10.1088/1361-648X/AB7FD8.

[97] R.F.W. Bader, Atoms in Molecules: A Quantum Theory, Oxford University Press, Oxford, 1990.

[98] W. Tang, E. Sanville, G. Henkelman, A grid-based Bader analysis algorithm without lattice bias, Journal of Physics: Condensed Matter. 21 (2009) 084204. https://doi.org/10.1088/0953-8984/21/8/084204.

[99] G. Henkelman, A. Arnaldsson, H. Jónsson, A fast and robust algorithm for Bader decomposition of charge density, Comput Mater Sci. 36 (2006) 354–360. https://doi.org/10.1016/J.COMMATSCI.2005.04.010.

[100] D.A. Neamen, Semiconductor Physics and Devices: Basic Principles, 4th ed., McGraw-Hill, New York, 2011.

[101] A. Suwardi, D. Bash, H.K. Ng, J.R. Gomez, D.V.M. Repaka, P. Kumar, K. Hippalgaonkar, Inertial effective mass as an effective descriptor for thermoelectrics via data-driven evaluation, J Mater Chem A Mater. 7 (2019) 23762–23769. https://doi.org/10.1039/C9TA05967A.

[102] G.J. Snyder, E.S. Toberer, Complex thermoelectric materials, Nature Materials. 7 (2008) 105–114. https://doi.org/10.1038/nmat2090.

[103] D.M. Rowe, CRC Handbook of Thermoelectrics, 1st ed., CRC Press, Boca Raton, 1995.

[104] S.D. Guo, Importance of spin–orbit coupling in power factor calculations for half-Heusler ANiB (A = Ti, Hf, Sc, Y; BSn, Sb, Bi), J Alloys Compd. 663 (2016) 128–133. https://doi.org/10.1016/J.JALLCOM.2015.12.139.

[105] A. Manchon, A. Belabbes, Spin-Orbitronics at Transition Metal Interfaces, Solid State Physics - Advances in Research and Applications. 68 (2017) 1–89. https://doi.org/10.1016/BS.SSP.2017.07.001.

[106] U. Mizutani, M. Inukai, H. Sato, E.S. Zijlstra, Electron Theory of Complex Metallic Alloys, Physical Metallurgy: Fifth Edition. 1 (2014) 103–202. https://doi.org/10.1016/B978-0-444-53770-6.00002-2.

[107] F. Casper, T. Graf, S. Chadov, B. Balke, C. Felser, Half-Heusler compounds: novel materials for energy and spintronic applications, Semicond Sci Technol. 27 (2012) 063001. https://doi.org/10.1088/0268-1242/27/6/063001.

[108] M.J. Mehl, D. Hicks, C. Toher, O. Levy, R.M. Hanson, G. Hart, S. Curtarolo, The AFLOW Library of Crystallographic Prototypes: Part 1, Comput Mater Sci. 136 (2017) S1–S828. https://doi.org/10.1016/J.COMMATSCI.2017.01.017.

[109] J. Yu, K. Xia, X. Zhao, T. Zhu, High performance p-type half-Heusler thermoelectric materials, J Phys D Appl Phys. 51 (2018) 113001. https://doi.org/10.1088/1361-6463/aaaa58.

[110] A.S. Gzyl, A.O. Oliynyk, L.A. Adutwum, A. Mar, Solving the Coloring Problem in Half-Heusler Structures: Machine-Learning Predictions and Experimental Validation, Inorg Chem. 58 (2019) 9280–9289. https://doi.org/10.1021/acs.inorgchem.9b00987.

[111] T. Graf, C. Felser, S.S.P. Parkin, Simple rules for the understanding of Heusler compounds, Progress in Solid State Chemistry. 39 (2011) 1–50. https://doi.org/10.1016/J.PROGSOLIDSTCHEM.2011.02.001.

[112] J. Ma, V.I. Hegde, K. Munira, Y. Xie, S. Keshavarz, D.T. Mildebrath, C. Wolverton, A.W. Ghosh, W.H. Butler, Computational investigation of half-Heusler compounds for spintronics applications, Phys Rev B. 95 (2017) 024411. https://doi.org/10.1103/PHYSREVB.95.024411.

[113] A.A. Mubarak, F. Hamioud, S. Tariq, Influence of Pressure on Optical Transparency and High Electrical Conductivity in CoVSn Alloys: DFT Study, J Electron Mater. 48 (2019) 2317–2328. https://doi.org/10.1007/S11664-019-06976-3.

[114] H. Shi, W. Ming, D.S. Parker, M.H. Du, D.J. Singh, Prospective high thermoelectric performance of the heavily p-doped half-Heusler compound CoVSn, Phys Rev B. 95 (2017). https://doi.org/10.1103/PHYSREVB.95.195207.

[115] M. Ameri, A. Touia, R. Khenata, Y. Al-Douri, H. Baltache, Structural and optoelectronic properties of NiTiX and CoVX (X = Sb and Sn) half-Heusler compounds: An ab initio study, Optik (Stuttg). 124 (2013) 570–574. https://doi.org/10.1016/J.IJLEO.2011.12.052.

[116] C.S. Lue, Y. Öner, D.G. Naugle, J.H. Ross, Magnetism of new semi-Heusler compounds FeVSn and CoVSn, IEEE Trans Magn. 37 (2001) 2138–2140. https://doi.org/10.1109/20.951101.

[117] M. Hichour, D. Rached, R. Khenata, M. Rabah, M. Merabet, A.H. Reshak, S. Bin Omran, R. Ahmed, Theoretical investigations of NiTiSn and CoVSn compounds, Journal of Physics and Chemistry of Solids. 73 (2012) 975–981. https://doi.org/10.1016/J.JPCS.2012.03.014.

[118] M. Zeeshan, H.K. Singh, J. van den Brink, H.C. Kandpal, Ab-initio design of new Heusler materials for thermoelectric applications, Phys Rev Mater. 1 (2017). https://doi.org/10.1103/PhysRevMaterials.1.075407.

[119] H. Abbassa, A. Labdelli, S. Meskine, Y.B. Cherif, A. Boukortt, Half-metallic properties in Co2XSn (X = Ti, V and Cr) full-Heusler compound, Modern Physics Letters B. 34 (2019) 2050028. https://doi.org/10.1142/S0217984920500281.

[120] N.T. Mahmoud, J.M. Khalifeh, B.A. Hamad, A.A. Mousa, The effect of defects on the electronic and magnetic properties of the Co2VSn full Heusler alloy: Ab-initio calculations, Intermetallics. 33 (2013) 33–37. https://doi.org/10.1016/J.INTERMET.2012.09.012.

[121] O.E. Osafile, O.N. Nenuwe, Lattice Dynamics and thermodynamic Responses of XNbSn Half-Heusler Semiconductors: A First-Principles Approach, Journal of the Nigerian Society of Physical Sciences. 3 (2021) 121–130. https://doi.org/10.46481/JNSPS.2021.174.

[122] Y. Ono, S. Inayama, H. Adachi, S. Yotsuhashi, Y. Miyazaki, T. Kajitani, Effects of Sb-doping on electrical transport properties of Co-based half-Heusler compound, Materials Research Society Symposium - Proceedings. 793 (2003) 195–200. https://doi.org/10.1557/PROC-793-S8.5/.

[123] A.R. Chandra, V. Jain, N. Lakshmi, R. Jain, V.K. Jain, Study of the electronic structure properties in Co2NbIn/Sn Heusler alloys, AIP Conf Proc. 1942 (2018). https://doi.org/10.1063/1.5028952/613275.

[124] A.U.B. Wolter, A. Bosse, D. Baabe, I. Maksimov, D. Mienert, H.H. Klauß, F.J. Litterst, D. Niemeier, R. Michalak, C. Geibel, R. Feyerherm, R. Hendrikx, J.A. Mydosh, S. Süllow, Structure and magnetic order of the Heusler compound Co2NbSn, Phys Rev B. 66 (2002) 174428. https://doi.org/10.1103/PhysRevB.66.174428.

[125] K.R.A. Ziebeck, P.J. Webster, Neutron diffraction and magnetization study of Heusler alloys containing Co and Zr, Hf, V, or Nb, J. Phys. Chem. Solids, 35 (1974) 1–7. https://doi.org/10.1016/0022-3697(74)90002-X.

[126] S. Süllow, C. Geibel, The magnetic and structural phase diagram of the Heusler-series (Co1-xNix)2NbSn, J Magn Magn Mater. 267 (2003) 115–119. https://doi.org/10.1016/S0304-8853(03)00344-5.

[127] R. Dutt, D. Pandey, A. Chakrabarti, Probing the martensite transition and thermoelectric properties of CoxTaZ (Z = Si, Ge, Sn and x = 1, 2): a study based on density functional theory, Journal of Physics: Condensed Matter. 33 (2020) 045402. https://doi.org/10.1088/1361-648X/ABBB40.

[128] J. Wei, G. Wang, Thermoelectric and optical properties of half-Heusler compound TaCoSn: A first-principle study, J Alloys Compd. 757 (2018) 118–123. https://doi.org/10.1016/J.JALLCOM.2018.05.037.

[129] The periodic table of the elements by WebElements, (n.d.). https://www.webelements.com/ (accessed August 1, 2023).

[130] B. Govind, A. Bhardwaj, A. Rajput, A. Kumar, S. Bano, D.K. Misra, Effect of ball milling on magnetic properties of a Heusler derivative Co9Ni7Sn8materials, AIP Conf Proc. 2220 (2020) 110024. https://doi.org/10.1063/5.0005577/600396.

[131] M. Weller, T. Overton, J. Rourke, F. Armstrong, Inorganic Chemistry, 7th ed., Oxford University Press, Oxford, 2018.

[132] H. Abbassa, A. Labdelli, S. Meskine, Y.B. Cherif, A. Boukortt, Half-metallic properties in Co2XSn (X = Ti, V and Cr) full-Heusler compound, Modern Phy Letters B. 34 (2019). https://doi.org/10.1142/S0217984920500281.

[133] I. Galanakis, P. Mavropoulos, P.H. Dederichs, Electronic structure and Slater–Pauling behaviour in half-metallic Heusler alloys calculated from first principles, J Phys D Appl Phys. 39 (2006) 765. https://doi.org/10.1088/0022-3727/39/5/S01.

[134] S.A. Wolf, D.D. Awschalom, R.A. Buhrman, J.M. Daughton, S. Von Molnár, M.L. Roukes, A.Y. Chtchelkanova, D.M. Treger, Spintronics: A spin-based electronics vision for the future, Science. 294 (2001) 1488–1495. https://www.science.org/doi/10.1126/science.1065389.

[135] L. Xi, J. Yang, L. Wu, J. Yang, W. Zhang, Band engineering and rational design of high-performance thermoelectric materials by first-principles, Journal of Materiomics. 2 (2016) 114–130. https://doi.org/10.1016/J.JMAT.2016.05.004.

[136] V.N. Antonov, B.N. Harmon, L. V. Bekenov, A.P. Shpak, A.N. Yaresko, Electronic structure and x-ray magnetic circular dichroism in the Heusler alloy Co2 NbSn, Phys Rev B Condens Matter Mater Phys. 71 (2005) 174428. https://doi.org/10.1103/PHYSREVB.71.174428/.

[137] E. Haque, M.A. Hossain, First-principles study of elastic, electronic, thermodynamic, and thermoelectric transport properties of TaCoSn, Results Phys. 10 (2018) 458–465. https://doi.org/10.1016/J.RINP.2018.06.053.

[138] R. Dutt, A. Chakrabarti, First-principles study to probe the effect of substitution at X and Z sites on the electronic, magnetic and transport properties of Co2X(V, Nb, Ta)Z(Al, Ga, In, Si, Ge, Sn) Heusler alloys, Solid State Commun. 359 (2023) 115022. https://doi.org/10.1016/J.SSC.2022.115022.

[139] Z. Yue, Z. Li, L. Sang, X. Wang, Spin-Gapless Semiconductors, Small. 16 (2020) 1905155. https://doi.org/10.1002/SMLL.201905155.

[140] X. Wang, Z. Cheng, J. Wang, X.L. Wang, G. Liu, Recent advances in the Heusler based spin-gapless semiconductors, J Mater Chem C Mater. 4 (2016) 7176–7192. https://doi.org/10.1039/C6TC01343K.

[141] L. Gagliardi, D.G. Truhlar, G.L. Manni, R.K. Carlson, C.E. Hoyer, J.L. Bao, Multiconfiguration pair-density functional theory: A new way to treat strongly correlated systems, Acc Chem Res. 50 (2017) 66–73. https://doi.org/10.1021/acs.accounts.6b00471.

[142] S. Guo, S. Anand, M.K. Brod, Y. Zhang, G.J. Snyder, Conduction band engineering of half-Heusler thermoelectrics using orbital chemistry, J Mater Chem A Mater. 10 (2022) 3051–3057. https://doi.org/10.1039/D1TA09377K.

[143] Y. Quan, S. Yue, B. Liao, Impact of Electron-Phonon Interaction on Thermal Transport: A Review, Nanoscale and Microscale Thermophysical Engineering. 25 (2021) 73–90. https://doi.org/10.1080/15567265.2021.1902441.

[144] Z.A.A.R. Almaghbash, O. Arbouche, A. Dahani, A. Cherifi, M. Belabbas, A. Zenati, H. Mebarki, A. Hussain, Thermoelectric and Piezoelectric Properties in Half-Heusler Compounds TaXSn (X = Co, Rh and Ir) Based on Ab Initio Calculations, Int J Thermophys. 42 (2021) 1–19. https://doi.org/10.1007/S10765-020-02755-Z.

SCIENTIFIC ACTIVITIES

a) Published Article

A.A.G. Santos, P. D. Borges, Ab initio investigation of Co–Ta–Sn Heusler alloys for thermoelectric applications, Comput. Theor. Chem. 1229 (2023) 114301. https://doi.org/10.1016/j.comptc.2023.114301.

b) Presentation of work in scientific meetings

A.A.G. Santos, P. D. Borges, Estudo de primeiros princípios das ligas half-heusler CoTaSn e CoNbSn para aplicação como materiais termoelétricos de alta eficiência. XXXIV Encontro Regional da SBQ-MG, Minas Gerais, 2022. *Work presented by Alan A. G. Santos.*